Universidade do Minho
Escola de Engenharia

Sacha Trevelyan Mould

Nanocomposites: the contribution of multiscale modelling to improve the dispersion levels

Outubro de 2013

Nanocomposites: the contribution of multiscale modelling to improve the dispersion levels
Sacha Trevelyan Mould
UMinho | 2013

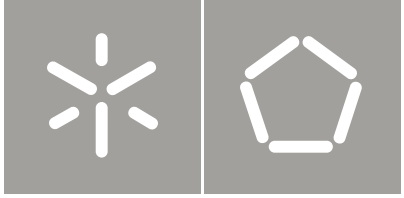

Universidade do Minho
Escola de Engenharia

Sacha Trevelyan Mould

Nanocomposites: the contribution of multiscale modelling to improve the dispersion levels

Tese de Doutoramento
Ciência e Engenharia de Polímeros e Compósitos

Trabalho efectuado sob a orientação do
Professor Doutor João Miguel Amorim N. C. Nóbrega
Professor Doutor José António C. G. Covas

Outubro de 2013

Rejoice with your family in the beautiful land of life.

— Albert Einstein

Dedicated to my parents:

Roy A. Mould and Ute B. Mould.

ABSTRACT

Polymer/layered silicate nanocomposites are a new class of materials that have raised much enthusiasm in scientific and technological domains due to their remarkable properties. However, tailoring their morphology and properties still remains a challenge. The present thesis combines experimental and theoretical approaches to further improve the knowledge available on the behavior of such materials.

A new on-line rotational rheometer to monitor the compounding process at the lab and industrial scales was designed and assessed, with a view to practical process monitoring and control. On-line measurements were performed during nanocomposite production in order to establish relationships between material formulation and processing conditions. Namely, the aim is to determine whether changes in clay type, clay content and process parameters (e. g., feed rate and screw speed) cause detectable alterations in the rheological response and thus in the level of dispersion. The analysis of the data was supported by XRD and electron (scanning and transmission) microscopy observations.

Secondly, multiscale simulations are undertaken based on coarse-graining methods, in order to capture the most relevant properties of bulk polymers and polymer nanocomposites. In the literature the amount of work dealing with coarse-graining simulations of polymers is inumerous, but little attention is given on how the magnitude of coarse-graining affects the accuracy of the local and global behavior of polymer chains. At a mesoscopic scale, particles enclose an arbitrary number of monomers with dimensions beyond the Kuhn length. Consequently, the resolution of local subtleties (e. g., fastest mode relaxations) is deteriorated and the scaling laws predicted by theory are scarcely applicable. A comprehensive analysis about how the magnitude of coarse-graining affects the equilibrium and non-equilibrium properties of linear polymer chains, at different molecular weights, is given. The results were quantitatively compared with molecular dynamics simulations, theoretical models and available experimental data. The parameters for mesoscopic simulations were empirically obtained from all-atom molecular dynamics simulations, and a time-mapping protocol is used to accurately accommodate the systems dynamics to the correct time-scale. Additionally, non-equilibrium simulations are used with the aim of studying the adjustability of the mesoscopic friction coefficient regarding the time-scale when steady and transient shear flows are imposed.

Finally, the procedure followed for the polymer/layered-silicate nanocomposite system allowed access to the large-scale morphology, providing a good starting point to further studies. Here, the effective potentials governing the mesoscopic interactions are estimated invoking the Iterative Boltzmann Inversion protocol. While atomistic simulations provide a detailed understanding of the clay interlayer structure and accurate predictions of the basal distance,

mesoscopic simulations provide the information necessary of the dispersion state of particles in the matrix.

RESUMO

Nanocompósitos à base de matrizes poliméricas e nanoargilas são novos materiais que, devido às suas excelentes propriedades, têm despertado bastante interesse tanto a nível científico como tecnológico. Todavia, controlar a sua morfologia de forma a obter propriedades específicas constitui ainda um desafio. Esta tese pretende analisar, propor e testar metodologias experimentais e teóricas inovadoras que forneçam uma melhor compreensão sobre o seu comportamento.

Um novo reómetro rotacional em linha para monitorizar o processo de mistura numa escala laboratorial e industrial foi projetado, implementado e validado, com o intuito prático de monitorizar e controlar o processo. Durante o processamento de nanocompósitos foram efetuadas medições em linha com a finalidade de se estabelecerem relações entre as formulações, as condições operatórias e a morfologia dos materiais obtidos. A influência do tipo e quantidade de nanoargila incorporada na matriz polimérica, assim como os principais parâmetros utilizados no processamento de nanocompósitos (débito e velocidade do parafuso da extrusora) no comportamento reológico e foi avaliada o grau de dispersão. A análise foi complementada com ensaios de difração de raios-X e microscopia electrónica de varrimento e transmissão.

Numa segunda vertente, simulações multi-escala com base em métodos de *coarse-graining* foram realizadas de forma a determinar as propriedades mais relevantes de polímeros e nanocompósitos à base de matrizes poliméricas. Embora o volume de publicações presentes na literatura abordando o tema seja vasto, a exploração do conhecimento sobre o modo de como o nível de *coarse-graining* afeta a precisão do comportamento local e global das cadeias do polímero é ainda limitada. Na meso-escala, cada partícula representa um número arbitrário de monómeros que se extende a comprimentos superiores ao de Kuhn. Consequentemente, a resolução das sutilezas locais (como por exemplo, as relaxações dos modos de Rouse mais rápidos) é afetada e as leis previstas pela teoria são apenas parcialmente aplicáveis. Uma análise detalhada sobre o modo como a magnitude do *coarse-graining* afeta as propriedades de equilíbrio e não-equilíbrio considerando diferentes pesos moleculares foi realizada. Os resultados foram comparados quantitativamente com simulações de dinâmica molecular, modelos teóricos e dados experimentais disponíveis. Os parâmetros utilizados nas simulações mesoscópicas foram obtidos empiricamente através de simulações atomísticas, e o mapeamento do tempo através de um protocolo para acomodar a dinâmica do sistema à escala de tempo correta. Adicionalmente, simulações em não-equilíbrio foram realizadas com o objetivo de estudar a ajustabilidade do coeficiente de fricção mesoscópico relativamente à escala de tempo em situações de fluxos estacionários e transientes.

Finalmente, foi desenvolvido um procedimento multi-escala que permite avaliar o estado da morfologia de sistemas contendo nanocompósitos à base

de matriz polimérica e nanoargila, tornando-se um ponto de partida para estudos mais detalhados. Os potenciais efetivos de interação foram obtidos através do algoritmo iterativo de inversão de Boltzmann. Enquanto que as simulações atomísticas proporcionaram um estudo detalhado da morfologia inter-lamelar e da distância basal, as simulações mesoscópicas forneceram informações essenciais sobre o estado de dispersão das nanopartículas na matriz polimérica.

We ourselves feel that what we are doing
is just a drop in the ocean.
But the ocean would be less because of
that missing drop.

— Mother Teresa

ACKNOWLEDGEMENTS

No words can describe how grateful I am for the support from those who directly or indirectly helped me to overcome so many hurdles to the successful completion of this work.

First and foremost, I would like to thank my supervisor, Prof. João Miguel Nóbrega, and co-supervisor, Prof. José António Covas, for their unquestionable guidance, support, and continuous belief in my ability to develop my research. They deposited their trust, giving me the opportunity to explore fields of knowledge that were beyond my academic experience, undoubtedly tracing my future research interests and professional growth.

I would like to express my sincere gratitude to Prof. Maurizio Fermeglia, Prof. Sabrina Pricl, Radovan Toth and Paola Posocco, from the Molecular Simulation Engineering Laboratory - MOSE (University of Trieste), for giving me the opportunity to spend nine months at their facility to learn and assimilate my first steps in molecular modelling. Their recommendations, guidance and openness to discuss some of the issues regarding the work were crucial.

Thanks to the Portuguese Foundation for Science and Technology (FCT) for the financial support through the PhD grant SFRH/BD/48512/2008, and the MultiHybrids IP 026685-2IP project under the 6^{th} Framework EC Program POCI 2010, for funding the parts and equipment associated to the on-line rheometer.

Many thanks to my colleagues, past and present, for all their patience and support: Prof. Ana Vera Machado Nóbrega, for believing in me at the early stage of my scientific career and for the guidance on selecting material formulations and discussion of the results; Joana Barbas, for the countless hours working together at the extruder and being able to share her experience; Simão Pereira, who assisted on the design of the on-line rheometer and, most importantly, from whom I owe the motivation, inspiration and friendship he constantly kept during my PhD journey; Oliver Pozo, in sharing his time with discussions related to simulations and programming; Raquel Santos, for reviewing the portuguese version of the abstract and the encouragement given during the writing of this thesis; Acácio Crespo, Flávio Rocha and Rafael RC, for their valuable assistance on the implementation of the graphical user interface that controls the on-line rheometer; João Paulo Peixoto, for his care giving technical support while working at the extruder machine; the "*Redondel*" crew (they know who they are), who always provided a pleasant working environment and moments of joy.

Thanks goes to Enrico Masarati from LyondellBasell, who through the scope of the MultiHybrids project provided all the conditions necessary to test the on-line rheometer in an industrial scenario at Basell Poliolefine Italia S.r.l. (Ferrara, Italy).

Most of all, I would not have ever made it this far without the love, dedication and support of my parents, Roy A. Mould and Ute B. Mould. This dissertation is dedicated to them.

CONTENTS

ACRONYMS *(by order of appearance)*

PLS Polymer/Layered Silicate

XRD X-Ray Diffraction

TEM Transmission Electron Microscopy

NMR Nuclear Magnetic Ressonance

FTIR Fourier Transform Infrared

UNF Unified Thread Standard

LDPE Linear Low-Density Polyethylene

PS Polystyrene

PP Polypropylene

MFR Melt Flow Rate

NC Nanoclay

PP-g-MA Polypropylene-Grafted-Maleic Anhydride

IUPAC International Union of Pure and Applied Chemistry

HDPE High Density Polyethylene

MA Maleic Anhydride

CNT Carbon Nanotube

PA6 Polyamide 6

SAOS Small Amplitude Oscillatory Shear

SEM Scanning Electron Microscopy

STD Specific Tactoids Dispersion

2M2HT Dimethyl Dihydrogenated tallow ammonium

MD Molecular Dynamics Simulations

MC Monte Carlo simulations

BD Brownian Dynamics

DPD Dissipative Particle Dynamics

PE Polyethylene

FF Force Field

DP Degree of Polymerization

NVT Canonical ensemble [fixed number of particles (N), volume (V) and temperature (T)]

NPT Isothermal-isobaric ensemble [fixed number of particles (N), pressure (P) and temperature (T)]

NVE Microcanonical ensemble [fixed number of particles (N), energy (E) and temperature (T)]

LAMMPS Large-scale Atomic/Molecular Massively Parallel Simulator

IBI Iterative Boltzmann Inversion

IM Inverse Monte Carlo

NEMD Non-Equilibrium Molecular Dynamics

CG Coarse-Graining

MMT Montmorillonite

PCFF Polymer Consistent Force Field

BI Boltzmann Inversion

VOTCA Versatile Object-oriented Toolkit for Coarse-graining Applications

GROMACS GROningen MAchine for Chemical Simulations

FEM Finite Element Method

FVM Finite Volume Method

NIR Near-Infrared spectroscopy

Part I

PREAMBLE

1

INTRODUCTION

1.1 MOTIVATION

An overview of the wide range of daily products will make clear that most are based on soft matter. Good examples are polymers, colloidal dispersions, liquid crystals and polymer nanocomposites. The latter have received tremendous attention due to their significantly enhanced physical (e. g., barrier to gases, flame retardancy, electrical conductivity) and mechanical properties when compared with the neat polymer or conventional *micro-* and *macro-*composites. Examples of nanoparticle species often dispersed in polymeric matrixes are carbon-based allotropes (e. g., nanotubes, fullerenes, graphene nanoribbons, nanohorns), inorganic layered and porous silicates (e. g., montmorillonite, mica, zeolite), cellulose nanowhiskers and particulate titanium dioxide. The selection of the type of nanoparticle to use dependson the polymer employed and on the desired properties. This work will focus on formulations comprising layered silicates, PLS.

The preparation of polymer-clay nanocomposites consists of the dispersion of the fillers in a polymer matrix by means of one of three possible strategies: i) *in-situ* intercalative polymerization, ii) solution intercalation, and iii) melt intercalation. The resulting morphologies may vary depending on the miscibility of the species and on the processing conditions. Nanoparticles can appear forming bulky agglomerates suspended in the matrix (poor dispersion), swollen structures due to intercalation of the polymer inside the clay galleries, complete exfoliated clay platelets caused by the structural break down of the layered structure (complete delamination), and/or a combination of them. *In-situ* polymerization and solution intercalation are able to achieve the desirable exfoliated morphology, since clay platelets are easily diluted in a hydrophilic medium. However, these techniques are more oriented to laboratorial practices and batch production, where a well controlled production environment is possible. Also, they require the use of expensive solvents and catalysts, which is not environmently attractive and may compromise the purity of the final nanocomposite. Currently, melt intercalation is accepted as the most promising PLS fabrication technique, since it is enviromentally sound efficient and uses conventional polymer compounding technologies (e. g., extrusion), hence can be easily scaled-up to industrial practice. However, since correlations between processing conditions and nanocomposites morphology remain unclear, a general procedure for tailoring the characteristics of these materials to a specific application is still lacking. To accomplish this, it is mandatory not only to understand the underlying dispersion mechanisms, but also how these are influenced by process and material parameters.

X-ray diffraction, XRD, and transmission electron microscopy, TEM, techniques are usual first choices to experimentally probe the structure PLS nanocomposites. XRD provides a convenient and precise way to quantify the interlayer spacing of silicate platelets up to ∼8 nm. TEM qualitatively provides a broader vision of the nanoparticles dispersion state, but sample preparation is lengthy and the area of analysis is quite small. Other techniques, such as nuclear magnetic resonance, NMR, and Fourier transform infrared spectroscopy, FTIR, have been used to investigate the surface chemistry, and the dynamics and conformation of the organic species (i. e., polymer and surfactant) in the nanocomposite. Rheological methods (e. g., small-amplitude oscillatory shear, creep & recovery/stress relaxation) have become popular due to the inherent simplicity regarding the operation, fast appraisal, and also because a direct correlation between structure and processability of these materials becomes readily attainable. Also, the rheological behaviour is very sensitive to morphological or composition changes in the composites. From an industrial perspective, this is of utmost importance, since it can supply a route for quality and process control. Moreover, a new generation of rheometers, with capabilities to perform measurements in real-time during and along the compounding process, definitely makes rheological practices even more appealing. These devices, denoted as on-line rheometers, possess all the operability options presented by standard benchtop machines, but use samples directly collected from the process, without any possible change in morphology or degradation. Thus, their use of to monitor the evolution of filler dispersion during compounding of polymeric systems seems particularly appealing.

From a practical point of view, it is still a challenge to develop polymer nanocomposites with pre-defined and controlled properties. Therefore, computer modeling and simulation is playing an increasing role towards material design and property predictions. Likewise, results from simulations can provide complementary information for experimental results, and supports the establishment of material specifications. These become more significant for materials having properties depending on multiscale features, extending over a wide range of length and time scales. The hierarchical characteristics of polymer nanocomposites start at the molecular scale - dictated by the surface energetics between polymer and clay particles -, passing through the mesoscopic scale - determined by diffusion and solubility parameters that lead to the equilibrium morphology of the nanocomposite - and, finally, the macroscopic scale - where properties depend on the overall synergies of the system components. While macroscopic and mesoscopic simulations are too coarse to account for the finer subtleties of the molecular scale, atomistic simulations are computationally demanding, which hinders the possibility of using them on a regular basis. Thus, the idea of multiscale simulation is to combine models and simulation techniques inherent to each scale and predict relevant properties that cannot be handled with simulations at a single scale solely. They are expected to generate results in a reasonable time-frame. Also, an entire description of the material behavior can be obtained (e. g., conformational state, dynamics, probability distribution functions). Several multiscale

methodologies were proposed in the past, depending on the type of problem in hands. The most common involves the *message-passing* through scales, in which simulations at the finer scale are used to define the parameters of the coarser scale model. Such mapping scheme, based on coarse-graining techniques, still remains one of the biggest challenges of multiscale modeling. Although mulsticale simulations of PLS nanocomposites have been performed, resulting in outstanding predictions of mechanical properties, a procedure allowing the study of dynamical and rheological parameters at the large-scale is still lacking.

1.2 OBJECTIVES

The complexity of tailoring PLS nanocomposites to yield specific properties demands a better knowledge of the link between their inherent *many-scale* hierarchical features and the technological aspects concerning their production. In turn, it requires adaptive characterization methods that establish a clear relationship between material properties and processing conditions. In the past, the University of Minho has developed on-line methods to monitor the extrusion process. Thus, the first part of this thesis envisions the availability of an on-line rheometer to detect eventual morphological changes of nanocomposites during extrusion compounding. The main goals corresponding to this part are:

- To validate the design and operability of a new prototype rotational rheometer;
- To evaluation the sensitivity of the instrument to morphological differences in PLS nanocomposites when both material formulation and processing conditions are altered;
- To scale-up the on-line rheometer for industrial practice.

Computational modeling may help to quantify or assess material characteristics that cannot be determined through experiments, nor being obvious at first hand. The second part of the thesis aims at providing additional insights into the relation between material properties and the *physico-chemical* nature of the nanocomposite systems. To this end, the main objectives are:

- To study the influence of coarse-graining on the equilibrium properties of simple polymeric systems;
- To generate predictions of rheological properties at the mesoscopic level through non-equilibrium simulations;
- To analyze in detail a PLS intercalated system through atomistic simulations;
- To develop a multiscale methodology able to simulate PLS systems at the mesoscopic scale and provide means to predict dispersion.

1.3 OUTLINE OF THE THESIS

The thesis is structured in four main parts:

I Preamble;

II On-line rheometry;

III Computational modelling;

IV Closure.

The first part includes the current chapter (Chapter 1), and provides a brief overview of the most relevant topics outlined throughout the thesis. The importance of on-line rheometry and multiscale modelling are emphasized, evidencing a motivation to the work. The main objectives are also summarized.

The second part is exclusively dedicated to the experimental based work developed in the thesis. Chapter 2 presents the new on-line rotational rheometer prototype, detailing its design, operation steps and validation. In the scope of PLS nanocomposites, the usefulness of the instrument to detect morphological changes during the compounding process, with respect to different material formulations and processing setup, is evaluated in Chapter 3 and Chapter 4.

The third part comprises theoretical and computational studies related to polymer solutions and PLS nanocomposites. Coarse-graining methodologies are used to map the structure and interactions from atomistic to mesoscopic models. In Chapter 5, the static and dynamical properties of a bulk polymeric system are analyzed in terms of the coarse-grained level chosen. The scaling laws governed by mesoscopic sytems are confronted with theoretical predictions of semidiluted polymer systems. In the sequence, in Chapter 6, the same systems were used for non-equilibrium simulations in order to predict some relevant rheological propeties. A protocol to adjust the system dynamics to the correct time-scale is also proposed. Chapter 7 presents atomistic and mesoscopic simulations of a PLS nanocomposite system. The former captures important morphological features at the gallery spacing length scale, while the latter provides information about the state of dispersion of the silicate particles. A step-by-step coarse-graining protocol is used to estimate the interactions of the system components.

Finaly, the thesis concludes (Chapter 8) with a general overview of the work developed and proposals for future research on the subjects covered.

Part II

ON-LINE RHEOMETRY

This part is reproduced from:

- S. Mould, J. Barbas, A.V. Machado, J.M. Nóbrega, and J.A. Covas. Measuring the rheological properties of polymer melts with on-line rotational rheometry. *Polymer Testing*, 30(6):602 - 610, 2011.
- S. T. Mould, J. M. Barbas, A. V. Machado, J. M. Nóbrega, and J. A. Covas. Monitoring the production of polymer nanocomposites by melt compounding with on-line rheometry. *International Polymer Processing*, XXVII(5):527-534, 2012.
- S. Mould, J. Barbas, A.V. Machado, J.M. Nóbrega and J.A. Covas. Preparation of polymer-clay nanocomposites by melt mixing in a twin screw extruder: using on-line SAOS rheometry to assess the level of dispersion. *International Polymer Processing. ACCEPTED*

2

MEASURING THE RHEOLOGICAL PROPERTIES OF POLYMER MELTS WITH ON-LINE ROTATIONAL RHEOMETRY

2.1 INTRODUCTION

The measurement in real time of the rheological properties of polymer systems during their manufacture and processing remains an important scientific and technological target. In fact, since the rheological response of a material to an imposed shear/normal stress/strain rate is sensitive to composition, morphology, degree of mixing, temperature, etc, the data measured in real time can be used to assist the definition of material recipes, the optimization of operating conditions and/or screw design, as well as for quality control and, ultimately, process control. Usually, during industrial extrusion and compounding only a few process parameters are continuously monitored (typically temperature, pressure and motor amperage), which do not provide a direct assessment of the material attributes, only an estimation of the flow and heat transfer conditions. Therefore, there might be a significant time lag between the detection in the laboratory of a quality non-conformity from measurements of material samples collected from the production line and the correction of the processing conditions, which may lead to significant material waste.

Moreover, if the rheological measurements can be carried out along the length of the equipment, the evolution of physical-chemical processes can also be followed. Pertinent examples include the in situ compatibilization of polymer blends (where a major - often complex - morphology evolution takes place within a short screw length) [7], the peroxide-induced degradation of polyolefins (which is dictated by the degradation rate of the peroxide) [8] and the manufacture of nanocomposites containing carbon nanotubes or organoclays [9] (in both cases, certain dispersion levels are necessary for the desired performance levels). Currently, it is quite clear that in these situations standard off-line measurements performed on samples collected from the equipment (either during or after processing) may provide misleading information, since during the sample preparation step, or during the heating prior to the rheological characterization, the physical-chemical processes that were taking place in the processing equipment might continue to evolve, i. e., the sample measured off-line might not be really representative of the material taken at a specific collection point [10].

During the last two decades, academic groups and rheometer manufacturers have been attempting to develop reliable, precise, simple to operate and economically attractive in-line and on-line rheometers. In-line measurements are of particular interest, as they avoid melt by-passes and the eventual need of purging a certain amount of polymer melt. The "partial Couette" geometry

proposed by Dealy [11] is able to measure the shear stress corresponding to a single shear rate (related to the process throughput). The slit in-line rheometer developed by Kalyon and co-workers [12] contains a mechanism for the adjustment of the gap, but the range of workable shear rates is narrow. Another approach for measuring viscosity as a function of shear rate consists in coupling ultrasound flow velocity measurements to pressure difference readings along a certain channel length [13, 14]. Preliminary experiments in pipe flow seem encouraging, although the breath of the shear rate range will depend on the resolution of the ultrasound system. Smith and Glasscock [15] presented an in-line micro-Fourier rheometer using a squeeze flow technique, capable of measuring the linear viscoelastic properties within a reasonable frequency range. However, the correlation between off-line and on-line data needs to be established for each fluid application, thus reducing the practical utility of the method. The use of semi-hyperbolic dies for measuring the transient extensional viscosity has also been investigated by several authors (see, for example, the recent study by Baird et al [16]). The majority of these devices consists of - or could be implemented as - instrumented dies. It seems difficult to envisage their application along an extruder axis.

Most commercial solutions use capillary or slit rheometers to provide on-line measurements. Generally, they continuously transfer melt from the main stream, which then feeds the rheometer at constant rate, as set by means of a gear pump. After the measurement, the by-passed melt merges with the main stream (see, for example [17–19]). Design variations and different automation levels exist, but it is normally possible to simultaneously obtain apparent viscosities at different shear rates, as well as transient extensional viscosities from "zero length" dies. Although these devices are usually inserted between the extruder and the die, it is conceptually possible (although apparently not tried) to fix them upstream. In this regard, the Piezo Axial Vibrator is particularly attractive, since its feed port has the geometry of a standard melt pressure transducer (standard 1/2 UNF thread) [20]. This apparatus generates an axial oscillation on the material sample and uses piezo elements to record the rheological moduli. However, it still requires improvements in robustness, handling and signal noise.

On-line solutions seem easier to adapt to different equipments, to calibrate, clean and maintain, provide simpler means of varying the shear rate/frequency and offer good temperature control. However, it is also important to ensure that these devices: i) minimize the time-lag between sample collection and measurement, ii) prevent material morphology changes both during sampling and measurement, iii) enable measurements along the axis of the extruder (under normal conditions, the morphology or chemical reaction of a given polymer system will have achieved steady-state or been completed well upstream of the die) and iv) are capable of performing measurements at temperatures dissimilar from the processing temperature (or even carry out temperature sweeps). Covas et al. [21] developed an on-line capillary rheometer capable of collecting quickly, but under adequate conditions, material samples from within an extruder, that could be fixed at different axial locations of the ma-

chine. The device was successfully used to uncover the viscosity evolution of various polymer systems along the screw, thus contributing to better understand the corresponding mixing and/or chemical mechanisms. Due to the destructive (or potentially destructive) nature of capillary rheometry during the characterization of systems like polymer blends and nanocomposites, an on-line rotational rheometer, working either in steady shear or oscillatory mode, was later developed [10]. After validating the device, the authors were able to demonstrate its usefulness by measuring the evolution of the rheological moduli (G' and G") of a non-compatibilized and equivalent compatibilized polymer blend. They also showed how off-line measurements of samples collected from the extruder can produce misleading results, due to the changes in their characteristics that are induced by the several thermal cycles that they are subjected to during sample preparation. The number of cycles is obviously minimized in on-line measurements. Despite the encouraging results, the reproducibility of the device was somewhat operator dependent, owing to its mostly manual operation.

This chapter presents a new version of the original on-line rotational rheometer concept that incorporates design improvements and automated operation. As most commercial off-line top of the bench instruments, the new on-line rheometer is able to operate under different modes, such as steady state, frequency sweep, strain sweep, creep & recovery and stress relaxation, but can be fixed along an extruder barrel. The device is experimentally assessed by comparing its measurements with those carried out using conventional off-line rheometry. The evolution along the extruder axis of the linear viscoelastic response of three different materials is used to illustrate the practical utility of the new tool.

2.2 EQUIPMENT AND OPERATION

The concept of the on-line rotational rheometer is shown in Fig. 2.1 (see also Ref. [10] for a detailed description). The idea is to collect melt (1) from within the extruder (2) via opening the rotating tap (3) and shape it as required - typically into a disk or a tapered disk for parallel plates and cone-and-plate measuring geometries, respectively - by squeezing it between the lower (4) and upper (5) plates. Measurements are undertaken using the motion, sensing and controlling capacities of a commercial rotational rheometer (in this case, the head of an Anton Paar DSR301 rheometer) that is coupled to the upper plate (5) and fixed to the device by means of the adapter (6). As in conventional off-line rheometry, the instrument can operate in steady and oscillatory modes, a variety of tests types being possible, namely isothermal steady shear, frequency sweep, amplitude sweep, time sweep and step stress/strain (creep & recovery / stress relaxation). Also, since the device possesses its own temperature control system (it uses a coil heater fixed inside the hollow wall of the testing chamber, not represented in the Fig. 2.1), tests at different constant temperatures (namely, distinct from the extruder set temperatures), or temperature sweeps, are also feasible. The compact design, the short thermal

history and the negligible shear rate the melt is subjected to upon collection and prior to the rheological measurement prevent any significant changes in morphology (for example via coalescence) or chemical conversion (including degradation).

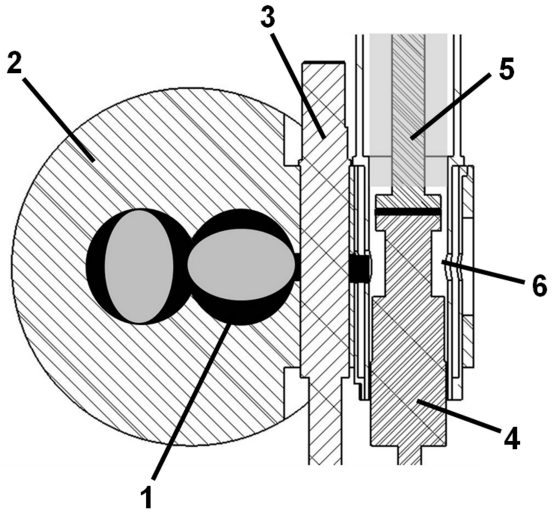

Figure 2.1: The on-line rheometer concept. 1 - melt; 2 - extruder; 3 - rotating tap; 4 - lower plate; 5 - upper plate; 6 - adapter for the rheometer.

The sequence of operations that make possible a rheological measurement are illustrated in Fig. 2.2. Fig. 2.2-a shows the extruder operating normally. At this stage, maintenance, cleaning and calibration of the on-line apparatus can be undertaken. Material flow from within the extruder towards the testing chamber will occur due to pressure difference when the rotating tap is opened (Fig. 2.2-b). The tap is closed when enough sample is available, preventing further melt influx (Fig.2.2-c). This is easy to detect, as melt will start emerging from a hole opposite to the inlet channel and visible to the operator. Typically, this operation takes less than 5 seconds. In order to manufacture a disk of sample material, the lower plate raises vertically to the pre-defined gap value (Fig. 2.2-d). Then, a cleaning ring slides downwards in order to wipe out any excess material around the edge of the plates (Fig. 2.2-e). A type K thermocouple embedded in the lower plate, with its measuring tip positioned very close to the surface in contact with the melt, makes it possible to monitor the average temperature and decide whether thermal equilibrium at the test temperature has been reached. Obviously, the time necessary to attain this equilibrium depends mainly on the difference between the incoming melt temperature and the required test temperature. It is relevant to recall here that viscous dissipation in co-rotating twin screw extruders can be quite significant, depending on the material and processing conditions, values of 20-60°C having been measured [22]. Once the rheological test has been performed, the cleaning ring and the lower plate retreat to their initial positions. The whole measuring system can be removed for (manual) cleaning.

As explained above, material inflow from within the extruder towards the testing chamber occurs due to pressure difference, when the rotating tap (3)

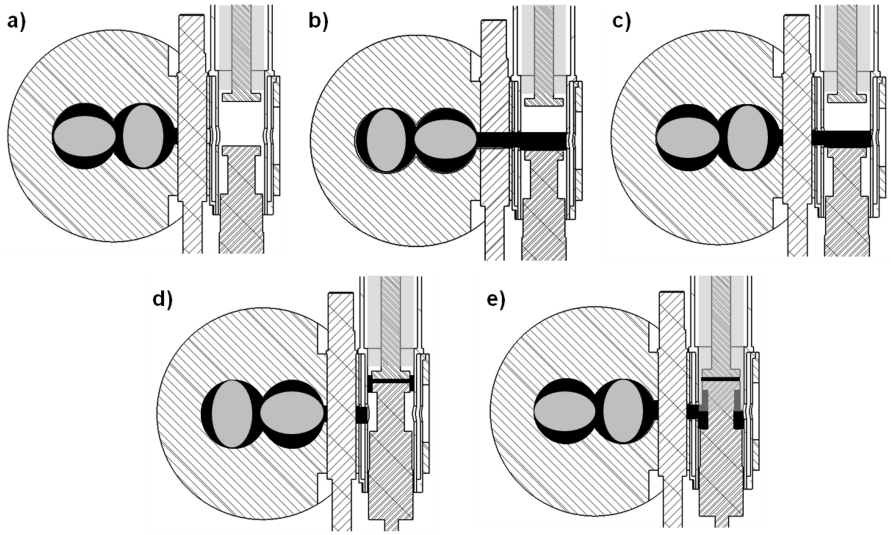

Figure 2.2: Operation sequence prior to the rheological test; (a) normal extruder operation; (b) melt flows from the extruder into the rheometer testing chamber; (c) sample collection is interrupted; (d) the lower plate raises to the pre-defined gap value; (e) the cleaning ring removes the excess material surrounding the measuring geometry.

(Fig. 2.1) is opened. In the case of the co-rotating twin screw extruder, melt pressure develops only in the fully filled sections of the screw, i. e., at restrictive zones comprising neutral or negatively staggered kneading disks and/or left handed elements, as well as along a few conveying screw turns upstream [23]. It has been reported that most changes in morphology, mixing levels and chemical conversion occur precisely at these locations [7]. Thus, taking advantage of the modular construction of most twin screw extruders, modified barrel segments containing several rotating taps can be conveniently inserted between original extruder barrel segments, to divert and characterize rheologically material samples at the most relevant screw locations. Fig. 2.3 provides a general view of the on-line rheometer when inserted at a given position along the barrel of a Leistritz LSM 30.34 laboratory twin screw extruder. If enough modified barrel elements are available, rheological measurements at small axial increments (typically 1D, where D is the screw diameter) are possible, i. e., a detailed evolution of the rheological response of a given material can be obtained. It is also worth mentioning that, in practice, these modified barrel elements can also accommodate other available on-line devices, namely an on-line Capillary Rheometer [21] and an on-line optical sensor for the measurement of Residence Time Distribution [24].

Sampling along the axis on an extruder might raise the question of whether the material present in the testing chamber of the on-line rheometer is fully molten, or whether solid polymer particles, even if distorted and smaller in size, are still present. Survival of the latter would obviously influence the rheological behavior and could generate ambiguous results or interpretations. To account for this possibility, the rotating tap (3) of Fig. 2.1 is in fact a three-way rotating valve, as depicted in Fig. 2.4. When the valve is in its closed position

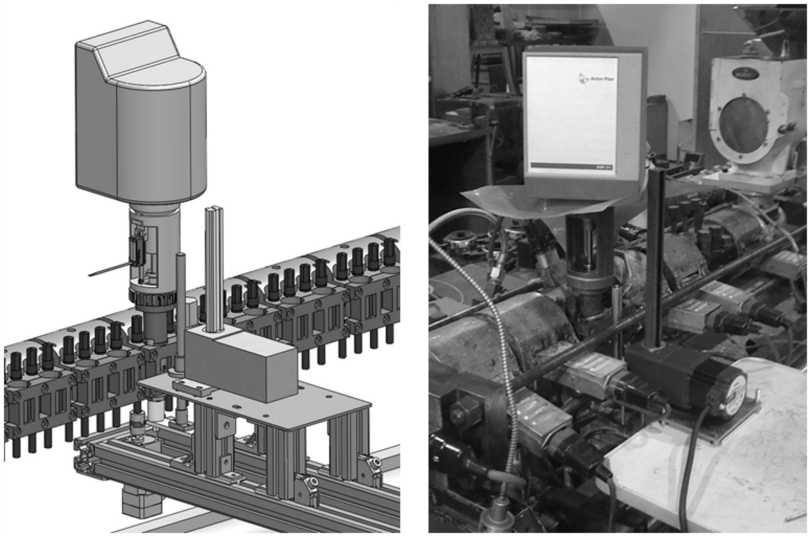

Figure 2.3: General view of the on-line rheometer when inserted at a given position along the barrel of a twin screw extruder.

(Fig. 2.4, left) the extruder operates normally. When it rotates 120° (Fig. 2.4, center), material is diverted from inside the extruder and can be directly collected by the operator, who can observe its physical appearance and/or save it for subsequent off-line characterization (for example, via electron microscopy and FTIR). This method of quick sampling was previously developed by the authors [10] and has been extensively used to study the evolution of morphology and/or chemical conversion of various polymeric systems [7] and to assess the predictions of processing software [22]. Upon further 120° rotation (Fig. 2.4, right), melt will flow into the on-line rheometer.

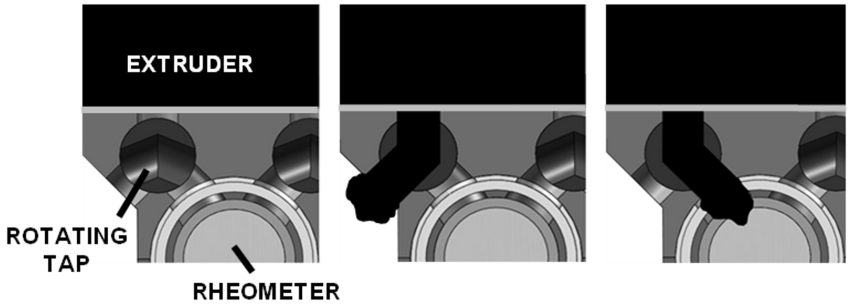

Figure 2.4: Three-way rotating valve. *Left*: closed position; center: sample collecting by the user; *right*: sample collection to the rheometer.

As represented in Fig. 2.5, the automatic control of the three-way valve (Fig. 2.4) and of all the operations preceding a rheological test (Fig. 2.2) is made via a software written in LabView®, specifically developed for that purpose. In turn, the RheoPlus® software supplied by Anton Paar controls the experiment. The movements associated to each operation step are created by a rotating step motor that operates the three-way valve, a linear step motor that drives the lower plate and a linear mini actuator that triggers the movement of the clean-

ing ring (see identification of this hardware in Fig. 2.6). The motion control software drives the motors and the actuator through a PCI motion controller card from National Instruments inserted on the computer, communication between them being guaranteed by a Universal Motion Interface, also from National Instruments. In addition, the same software guides the user through the various preparation steps of an experiment, including the definition of the various experimental parameters, material collection, shaping of the sample and thermal stabilization. The former include the gap between plates, the test temperature, the material sampling time and the thermal stabilization time. The device can work either in automatic or manual mode. Emergency stops have been provided. The user is continuously informed about the current step of the sequence, the time elapsed and the temperature of the testing chamber. When the thermal stabilization time is over, the RheoPlus® software is used to perform the experiment. Once this is completed, the motion control software is again used to make the on-line rheometer ready for cleaning or maintenance.

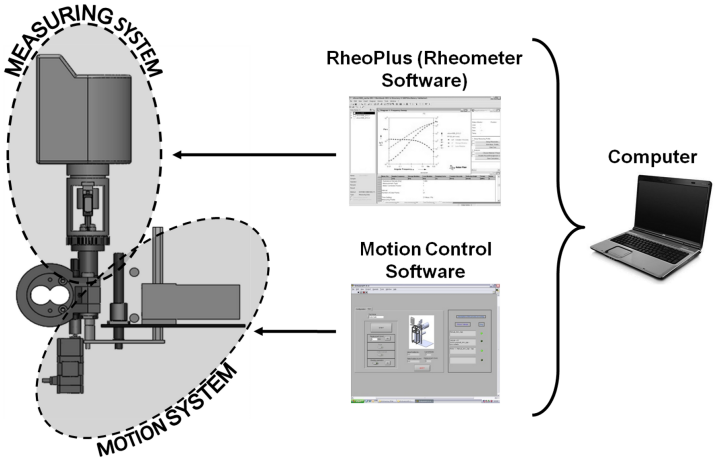

Figure 2.5: On-line rheometer control. *Top*: software used; *left*: operation sequence, *right*: distribution of steps between both programs.

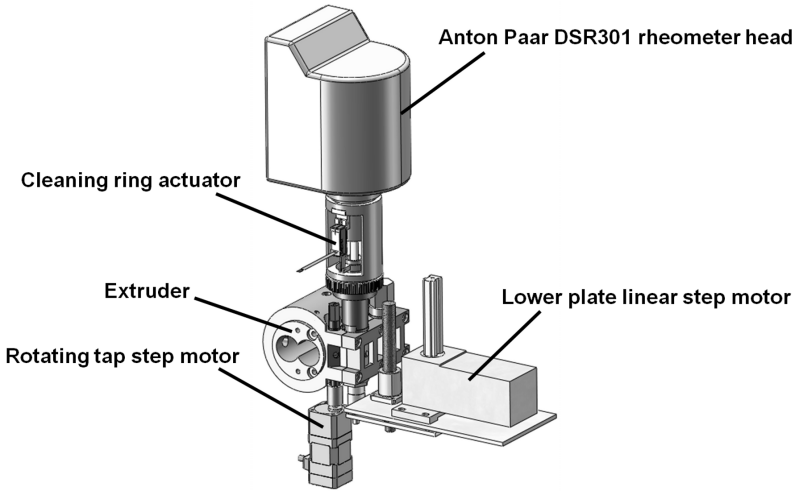

Figure 2.6: Motors and actuator used in the on-line rheometer.

2.3 MATERIALS

The materials presented in Table 2.1 were used to experimentally determine the sensitivity limits and assess the on-line rheometer. The two oils from Wacker exhibit a known constant viscosity along a relatively wide shear rate interval at room temperature. LDPE, PS and PP are polymers extensively used for packaging applications via blow molding, sheet extrusion and thermoforming and injection molding, respectively. Once the on-line rheometer was validated, the materials shown in Table 2.2 were compounded in a Leistritz LSM 30.34 laboratorial modular intermeshing co-rotating twin screw extruder and the evolution along the barrel of their dynamic rheological response was monitored. Dellite 67G is a naturally occurring montmorillonite modified with a high content of quaternary ammonium salt (dimethyl dihydrogenated tallow ammonium).

2.4 EXPERIMENTAL VALIDATION

The validation of the measurements made by the new on-line rheometer was divided in three stages, essentially following the strategy adopted to assess the original version [10]:

- room temperature off-line validation and determination of sensitivity limits, using two silicone oils of known viscosity;
- high-temperature off-line validation, using two high consumption polymers (LDPE and PS);
- high temperature on-line validation for another widely used polymer (PP).

The equivalent conventional off-line rheological characterization was performed either in a ARG2 (TA Instruments) or in a MCR 300 (Anton Paar) bench top rheometer, under identical experimental conditions, using a parallel plate configuration with a diameter of 25 mm and a gap of 1 mm (the plates diameter of the on-line rheometer is 20 mm and a gap of 0.8 mm was used). The frequency sweeps were performed from high to low frequencies. The disks for off-line characterization were prepared by compression molding under a pressure of 20 ton and a temperature of 210°C, 180°C and 200°C for PS, LDPE and PP, respectively.

2.4.1 *Room temperature off-line validation*

Fig. 2.7 compares the dynamic response (in terms of the complex viscosity, $|\eta^*|$, storage and loss moduli, G' and G'', respectively) of the two silicone oils with known viscosities, as measured by the MCR 300 and the on-line rheometer working off-line (i. e., in both cases, the gap between the plates was manually filled with oil). The extent of the linear viscoelastic response was determined off-line in the MCR 300, before performing the frequency

Table 2.1: Materials used for validation.

Material	Producer	Acronym	Grade	Viscosity/MFR
Silicone oil	Wacker	Oil 100	AK100000	100 Pa.s (room temperature)
Silicone oil	Wacker	Oil 1000	AK 1000000	100 Pa.s (room temperature)
Low-density Polyethylene	LyondellBasell	LDPE	Lupolen 1840	0.25 g/10min (190°C/2.16 kg)
Polystyrene	Polimeri Europa	PS	Edistir N1840	10 g/10min (200°C/5 kg)
Polypropylene	LyondellBasell	PP	Moplen HP500N	12 g/10 min (230°C/2.16 kg)

Table 2.2: Materials used for on-line measurements along an extruder.

Material	**Producer**	**Acronym**	**Grade**	**MFR/basal distance**
Polypropylene	LyondellBasell	PP	Moplen HP500N	12 g/10 min (230°C/2.16 kg)
Polypropylene -grafted-maleic anhydride	Crompton	PP-g-MA	Polybond 3200	115 g/10 min (190°C/2.16 kg)
Montmorillonite clay	Laviosa	NC	Dellite 67G	d_{001} = 3.45 nm

sweeps (a 1% strain was applied). The agreement between the two sets of data is satisfactory (average deviation of 5 and 8% in G' and 10% and 14% in G'' for Oil 100 and Oil 1000, respectively), specially for values of moduli beyond 1-10 MPa (similar differences were obtained with the original version [10]). The higher differences below this range are probably related to friction effects in the prototype rheometer, but the data for Oil 100 measured by the MCR 300 seems dubious (the MCR 300 has a torque resolution of 0.1 μNm, but measurements below 0.6 μNm seem unreliable).

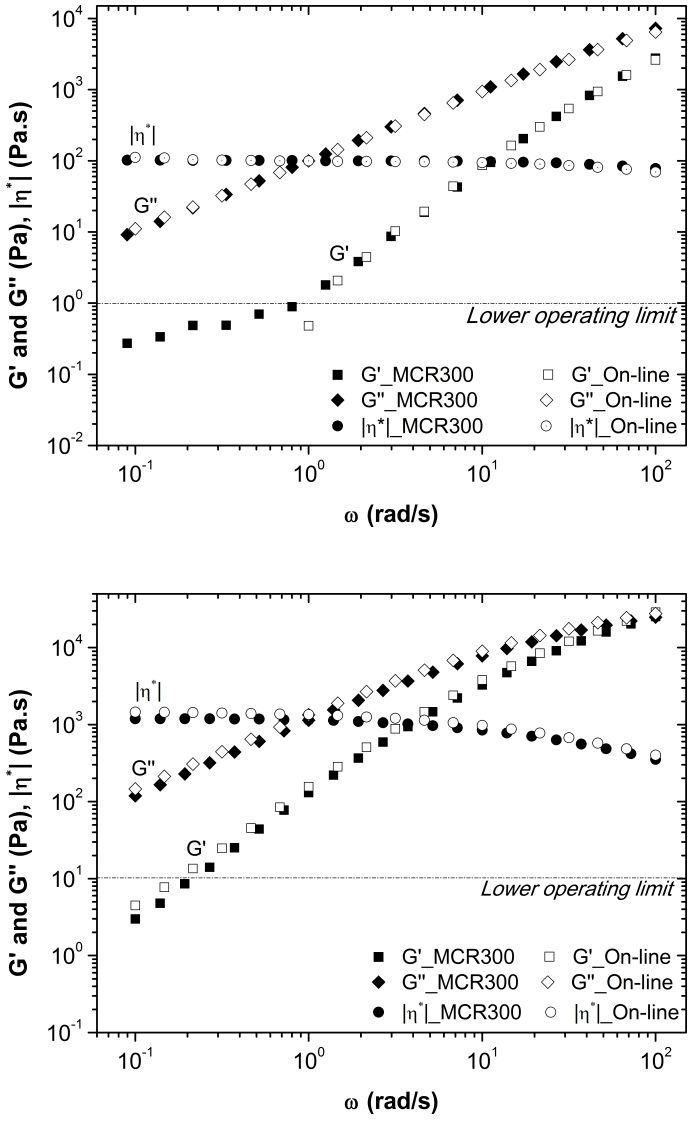

Figure 2.7: Linear viscoelastic behaviour of two silicone oils at 23°C, as measured by the Anton Paar MCR 300 rheometer and prototype rheometer working off-line (*top*: Oil 100; *bottom*: Oil 1000).

2.4.2 *High-temperature off-line validation*

The results with the silicone oils essentially provided a mechanical validation of the set up (in terms of mechanical stiffness, motion transmission and alignment of components). The assessment at high temperatures was carried out for two polymers with good thermal stability, PS and LDPE. Also, PS has a viscosity that is quite sensitive to temperature changes, while LDPE is usually a very elastic material (the grade chosen is also known as IUPAC-X and is extensively used by the academic community for rheology studies [25, 26]).

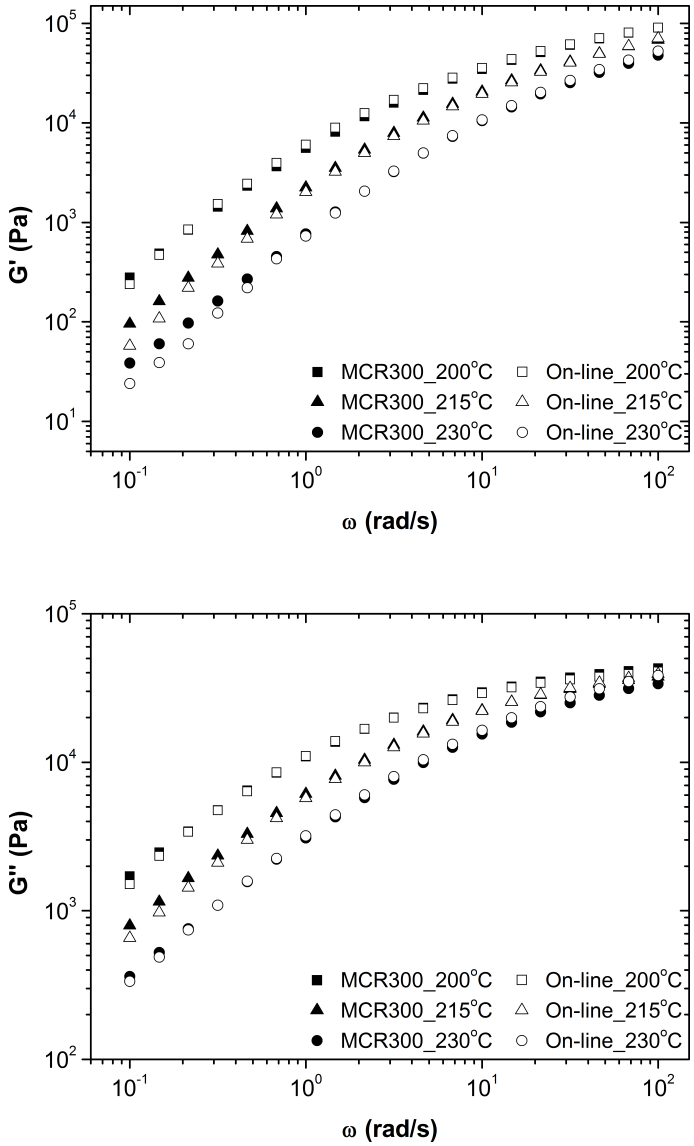

Figure 2.8: Linear viscoelastic behaviour of PS at 200°C, 215°C and 230°C, as measured by the Anton Paar MCR 300 rheometer and prototype rheometer working off-line.

Fig. 2.8 compares the variation of the dynamic moduli G' and G'' of PS with changes in frequency from 0.1 to 100 rad/s, at three different tempera-

tures (200°C, 215°C and 230°C), as measured by the Anton Paar MCR 300 and by the prototype rheometer working off-line. The superposition between the two sets of curves is virtually perfect for frequencies above 1rad/s (differences of 3%). Below this threshold the differences are of the order of 11%. Figures 2.9 and 2.10 concern the rheological behavior of LDPE. Fig. 2.9 contrasts the linear viscoelastic response at 180°C measured by the ARG2 (TA Instruments) rheometer and the prototype rheometer working off-line, while Fig. 2.10 compares the steady shear viscosity at the same temperature. The agreement between the data is very good throughout the frequency/shear rate. Overall, the deviation between the values measured by the two commercial rheometers and the prototype equipment is lower than 5%, which is well within the experimental error of this type of instruments.

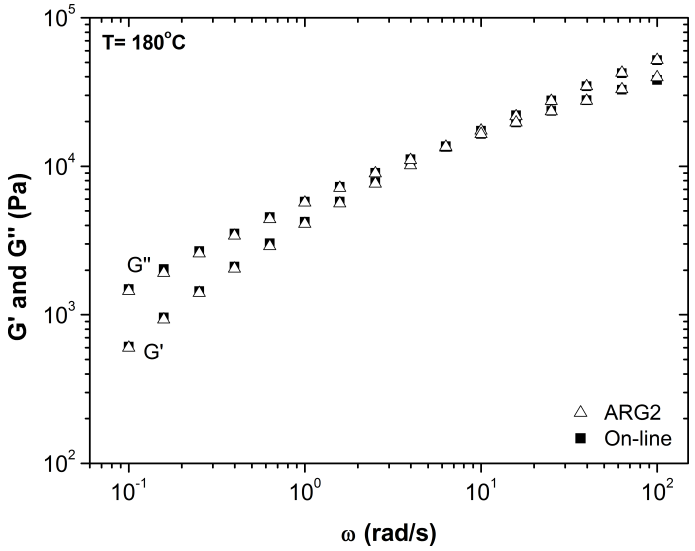

Figure 2.9: Linear viscoelastic behaviour of LDPE at 180°C, as measured by the ARG2 (TA Instruments) rheometer and prototype rheometer working off-line.

2.4.3 *On-line validation*

Before proceeding with the comparison of data measured off-line (with the commercial rheometers) and on-line with the new instrument, it is worth verifying the performance of the latter in terms of the capacity of independent temperature control. In fact, since the equipment will be physically coupled to an extruder, it will be exposed to conducted and irradiated heat from the heater bands of the latter.

Fig. 2.11 presents the general layout of the modular Leistritz LSM 30.34 twin screw extruder used in this work, which has a *L/D* (length to screw diameter ratio) of 29 and a screw diameter of 30 mm, together with the screw profile utilized in the experiments, adopting the usual nomenclature to describe it. The screw comprises three mixing zones with different axial lengths, composed of staggered kneading disks and a left handed element, separated by conveying

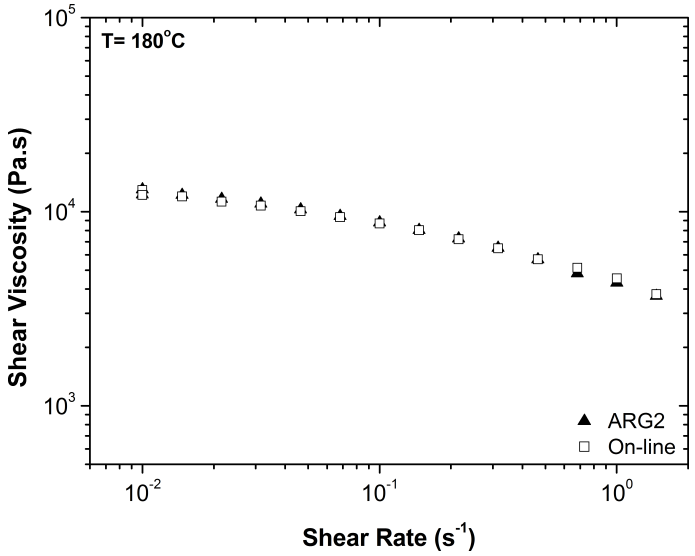

Figure 2.10: Shear viscosity of LDPE at 180°C, as measured by the ARG2 (TA Instruments) rheometer and prototype rheometer working off-line.

zones that will work partially filled if typical operating conditions are chosen. Melting is expected to occur immediately upstream of the first restrictive zone. Two modified barrel segments, each able to accommodate the on-line rheometer and to collect material from within the extruder from 4 distinct locations, were inserted in-between original barrel segments, in order to become contiguous with the first two screw mixing zones (in the downchannel direction). All extrusion runs reported here were performed with barrel and die set at 200°C, screws rotating at 100 rpm and a feed rate of 3 kg/h.

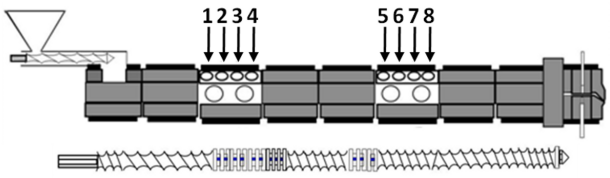

Figure 2.11: Twin screw extruder fitted with two modified barrel segments (with sampling ports) to accommodate the on-line rheometer and screw profile used in the experiments: **xxRy** - conveying element, where *xx* is the pitch (mm) and *R(=120)/y* is the length (mm); **LH**, left handed element; **xKByy** - kneading block, where *x* is number of discs and *yy* the staggering angle (in degrees).

The response of the temperature control system of the prototype to changes in the set values is depicted in Fig. 2.12. Initially, both extruder barrel and rheometer testing chamber were set to 220°C. As seen in the initial part of the graph, there is a fine agreement between set and measured temperature. When the former was changed to 250°C, the control system acted immediately and a new stable test chamber temperature, coincident with the set value,

was reached after approximately 12 minutes. When the set temperature was changed back to 220°C, the system took identical time to stabilize at this temperature. It is worth noting that these experiments were made with an empty rheometer, thus facing the thermal resistance of the air. As discussed above, the time required for melt temperature stabilization prior to a rheological measurement depends basically on the difference between the inlet melt temperature and the test temperature. The former can be higher than expected, due to the role of viscous dissipation in twin screw extruders. Using a 1 mm gap between plates, experiments with the original version of the on-line rheometer showed that, generally, stabilization time lasts around 20 and 50 seconds for temperature differences of 20 and 60°C, respectively, when testing PP and HDPE melts [10].

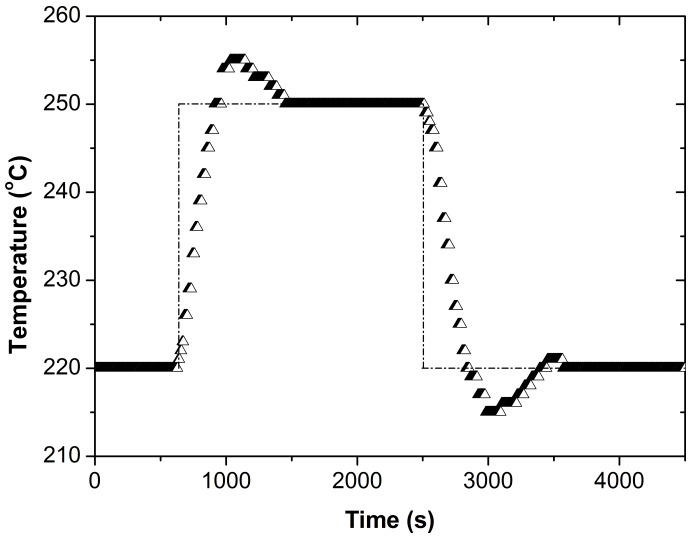

Figure 2.12: Response of the temperature control system of the prototype to changes in the set temperature.

Fig. 2.13 compares the linear viscoelastic response (G' and G'') of PP at 200°C, as measured both off-line and on-line at sampling ports 3 and 5 (see Fig. 2.11). The differences between the two measurements are of the order of 21% and 19% at locations 3 and 5 respectively, which is significant. Off-line measurements require the following sequence: i) collect a sample from the same barrel location of the on-line measurement and quench it in liquid nitrogen; ii) manufacture a disk (thickness of 1 mm, diameter of 20 mm) by compression molding; iii) position, re-heat and test the disk in the ARG2. These thermal cycles favor degradation, hence it is probably not a coincidence that the moduli measured on-line are a little higher than those measured off-line. In fact, the absence of a process stabilizer makes PP prone to thermo-oxidative degradation [27]. When the contrast between off-line and on-line measurements at the same locations are made for the PP/PP-g-MA system (same PP and 5% in weight of PP-g-MA), a better agreement is obtained, as seen in Fig. 2.14. In fact, the differences reduce now to approximately 6.5% and 13% at sampling ports 3 and 5 respectively, i. e., comparable to those observed for the

high-temperature off-line validation. PP/PP-g-MA being more thermally stable than PP, these results provide evidence that the poor mismatch between off-line and on-line measurements for PP is due to its thermal degradation.

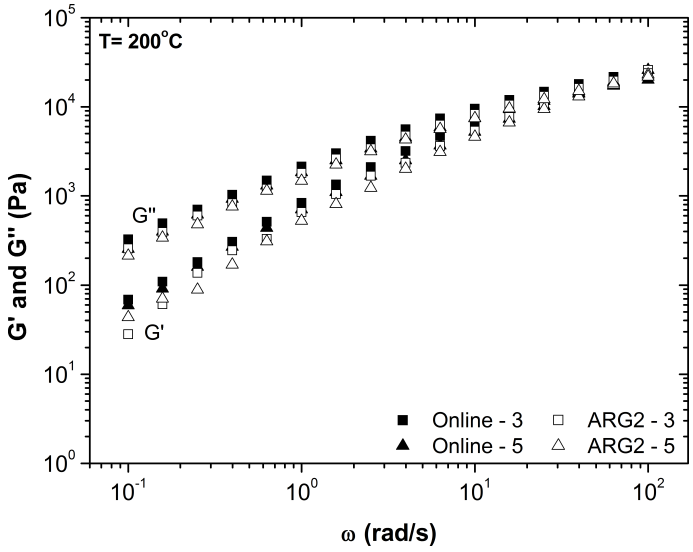

Figure 2.13: Linear viscoelastic behaviour of PP at 200°C, as measured by the ARG2 (TA Instruments) and on-line rheometers at sampling ports 3 and 5.

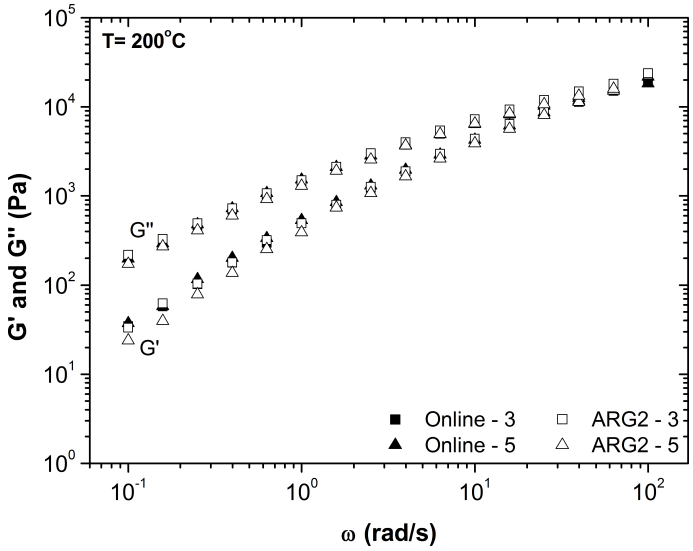

Figure 2.14: Linear viscoelastic behaviour of PP/PP-g-MA at 200°C, as measured by the ARG2 (TA Instruments) and on-line rheometers at sampling ports 3 and 5.

2.5 ON-LINE MEASUREMENTS ALONG THE AXIS OF AN EXTRUDER

As a demonstration of the usefulness and aptitude of the new on-line instrument, results of measurements made along the screw axis for three different, although related, polymer systems, are presented and discussed.

Fig. 2.15 depicts the variation of G' and G'' with frequency for PP (same material as in Fig. 2.13) at axial positions 3, 5 and 7 (Figure 2.11). The slight, although progressive, decrease of the moduli along the extruder referred above is now clearer. This behavior has been observed before [8], thus stressing again the benefit of using process stabilizers with this polymer.

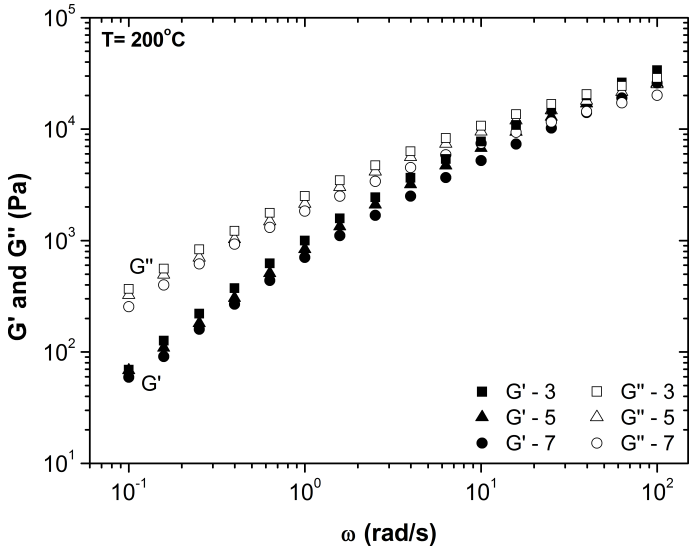

Figure 2.15: Linear viscoelastic behaviour of PP at 200°C, as measured on-line.

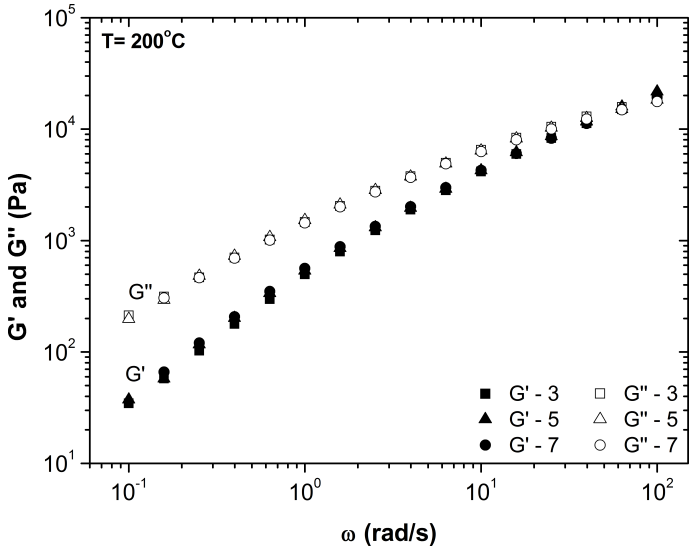

Figure 2.16: Linear viscoelastic behaviour of PP/PP-g-MA at 200°C, as measured on-line.

PP grafted with maleic anhydride (PP-g-MA) is often used for in-situ compatibilization of polymer blends, as adhesive for multilayer systems, or as coupling agent for glass fibers and fillers [28]. In relation to plain PP, a decrease of the rheological moduli is anticipated, due to chain scission during grafting of MA groups onto the polymer backbone [27, 29]. The rheological response of this system is pictured in Fig. 2.16. Comparison with Fig. 2.15 confirms the shift of the curves to lower moduli values and the better thermal stability.

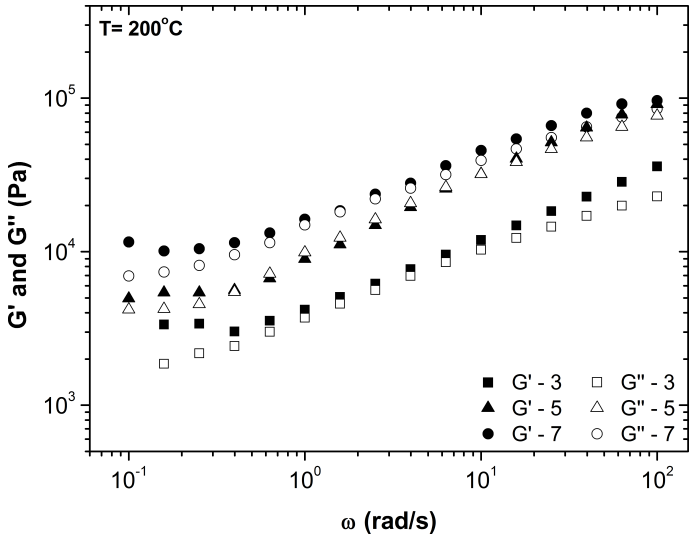

Figure 2.17: Linear viscoelastic behaviour of PP/PP-g-MA/NC at 200°C, as measured on-line.

In a third extrusion step, the PP/PP-g-MA system was compounded with 8.8% *w/w* of a montmorillonite organoclay, in order to produce a nanocomposite (a true nanocomposite is obtained when sufficient clay intercalation and clay exfoliation are achieved). The rheological curves of Fig. 2.17 were obtained for a constant strain of 0.1%, in order to ensure that the response would stay within the linear viscoelastic regime. The results present a number of interesting features:

- as expected, the presence of the clay shifts the curves to higher moduli values (near one order of magnitude relative to plain PP);
- while for molten PP, $G'' > G'$ during most of the frequency range (see Fig. 2.15), elasticity increases for the composite (both moduli have similar values);
- G' seems to level-off at frequencies below 0.4 s^{-1}, which is usually attributed to the deformation and recovery of the dispersed filler [30–33];
- an evolution along the barrel is clearly observed. Since, in principle, at constant clay content, the finer the dispersion the higher the moduli [9], the gradual increase in the moduli values should be due to progressively higher dispersion levels, as the material flows through successive mixing zones.

2.6 CONCLUSIONS

An on-line rotational rheometer was designed to collect melt samples at specific locations along the barrel of an extruder and characterize them either in steady shear or oscillatory modes. Operation of the instrument is controlled and assisted by a motion control software, specifically developed for this purpose and by the RheoPlus® software from Anton Paar, which is associated to the DRS 301 measuring head, produced by the same manufacturer.

Validation of the measurements performed by this device was made by direct comparison with similar measurements carried out by commercial bench top rheometers, including off-line measurements at room temperature with two silicone oils of known viscosity, off-line measurements at high-temperature using two polymers and on-line measurements with one polymer. In all cases, the agreement between the two sets of data was quite good. Thus, the validation step was considered as successful.

The instrument was then used to monitor the evolution of the rheological behavior of three polymer systems along the axis of a twin screw extruder. The results again evidenced the sensitivity and reliability of the apparatus and were in line with observations reported in the literature.

3

MONITORING THE PRODUCTION OF POLYMER/LAYERED-SILICATE NANOCOMPOSITES BY MELT COMPOUNDING WITH ON-LINE RHEOMETRY

3.1 INTRODUCTION

Since it was reported that the addition of a small percentage of an organoclay or of carbon nanotubes (CNT) to a polymer matrix could result in final excellent mechanical and physical properties, nanocomposites gained a wide interest for both academia and industry [34–48].

These materials are often prepared using melt compounding techniques that are readily available in industry (and thus allow companies of quite different sizes and working in a variety of application fields to explore their benefits), provide good production yields and automatic operation, are environmentally friendly and capable to generate the hydrodynamic stresses required to achieve sufficiently good dispersion. Intermeshing co-rotating twin screw extruders are particularly popular for this purpose.

Generally, high filler dispersion levels are required to take full advantage of their characteristics. In the case of organoclays, intercalation and exfoliation into the polymer matrix is mandatory [49, 50] whereas for CNT full dispersion is important for mechanical reinforcement, but the presence of some aggregates might be favourable for electrical conductivity [48]. Dispersion is influenced by material and processing parameters. For layered silicatebased clays, the former encompass the organic modifier, the properties of the polymer matrix and the type and concentration of the compatibilizer [51]; for CNT's agglomerate size, structure and cohesion, surface energy and purity are dominant [52]. In turn, the processing parameters determine the velocity fields, stress levels and residence times, which are obviously conditioned by the type of mixing equipment [48, 53–55]. The geometry of the equipment and the operating conditions control the mixing rate and the final dispersion level. However, and despite the significant number of studies on the topic, clear correlations between processing parameters and state of dispersion are still lacking, with contradictory results being reported. Information on the morphological evolution along the screws is scarcer [51, 56–58], although it would contribute to assess the influence of screw geometry and to better understand the underlying mixing mechanisms.

Direct assessment of (distributive and dispersive) mixing necessitates the use of electron microscopy techniques that are expensive and time consuming, often involve elaborate sample preparation and entail an extensive statistical analysis of a sufficiently high number of filler particles/fibers. Thus, the indirect characterization of dispersion by other techniques (such as X-ray diffraction, rheology, infra-red analysis), or the direct measurement of relevant fi-

nal features (tensile properties, electrical conductivity) are often adopted. It has been extensively shown that the rheological response of nanocomposites is sensitive to changes at different length scales [31, 42, 51, 59–62]. Thus, as rheometers are readily available in most laboratories, sample preparation is not too complicated and measurements are relatively straightforward, rheology is currently one of the most used methods to characterize dispersion. For example, the linear viscoelastic response of extruded samples produced under a variety of processing conditions can be employed to select the most adequate compounding condition for a specific nanocomposite. Rheological measurements of samples along the screw are much rarer. Lertwimolnun and Vergnes [57] reported results from dead-stop experiments with nanoclay composites, where the machine was stopped after reaching steady state operating conditions, the barrel was rapidly cooled, the screws were removed and material samples were collected from several axial locations. For a few processing conditions, the authors reported a reversion of the evolution of dispersion along the screws, which they attributed to a combination of local high temperature and long residence time, that induced either a degradation of the organic intercalant or an expulsion of the already intercalated polymer chains. In fact, these phenomena could also eventually develop under quiescent conditions while the barrel was being cooled, during compression molding of a disk for the subsequent rheological test, or even while waiting for thermal equilibrium between the plates of the rheometer, prior to the measurement. Similarly, in the case of CNT nanocomposites aggregate re-agglomeration has been reported when flow is interrupted, or when the material is subjected to repetitive thermal cycles [63, 64].

The advantages of on-line measurements are obvious: i) the number of thermal cycles necessary for sample preparation and thermal equilibrium are minimized, ii) if the rheological measurements can be performed along the length of the equipment, the evolution of physical-chemical processes can be followed, iii) periodic measurements at a certain location can be useful for quality and process control. Most commercial online instruments transfer melt from the main stream, which then feeds a capillary or slit die at constant rate by means of a gear pump. Generally, after the measurement the by-passed melt merges with the main stream. However, practice has shown that oscillatory rheometry is more adequate for the characterization of nanocomposites than capillary rheometry, because it preserves the initial sample morphology, is sensitive to small variations in dispersion and can deliver a rather complete rheological description. In the previous chapter (Chapter 2), a computer controlled on-line rheometer capable of quickly collecting material samples from within an extruder at different axial locations and performing the same measurements of typical bench top commercial instruments, was presented and validated experimentally. The instrument was designed to: i) minimize the time-lag between sample collection and measurement, ii) prevent material morphology changes both during sampling and measurement, iii) enable measurements along the axis of the extruder, and, iv) perform trials at temperatures other than the processing temperature.

3.2 MATERIALS AND EXPERIMENTAL DATA

3.2.1 *Materials*

The materials used in this study are listed in Table 3.1, together with their main characteristics. They include commercial polypropylene (PP), polypropylene grafted with maleic anhydride (PP-g-MA), polyamide-6 (PA6) and nanoclays (Cloisite 20A, Dellite 43B and Dellite 67G). The compositions produced are given in Table 3.2. For each polymer matrix, the amount and type of nanoclay was varied. When comparing nanoclay types, the amount of the latter was changed to keep the same inorganic content.

Table 3.1: Materials and main characteristics.

Designation	Material	Producer	Grade
PP	Polypropylene	LyondellBasell	Moplen HP500N
PA6	Polyamide 6	Rhodia	Technyl C206
PP-g-MA	Polypropylene-grafted -maleic anhydride	Crompton	Polybond 3200
D67G	Montmorillonite	Laviosa	Dellite 67G
D43B	Montmorillonite	Laviosa	Dellite 43B
C20A	Montmorillonite	Southern Clay Products	Cloisite 20A
C30B	Montmorillonite	Southern Clay Products	Cloisite 30B

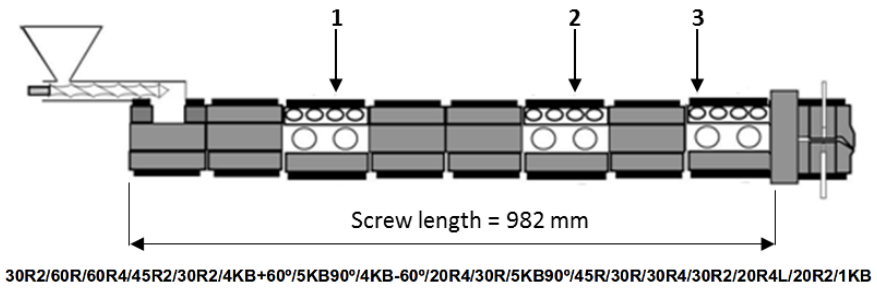

Figure 3.1: Extruder layout and screw configuration.

Table 3.2: Compositions produced and corresponding set screw speed.

PP wt.%	**PP-g-MA** wt.%	**PA6** wt.%	**Nanoclay type**, wt.%	**Screw-speed** (min^{-1})
95	5	-	-	100
86.2	5	-	D67G, 8.8	50,100,200
90.6	5	-	D67G, 4.4	100
77.4	5	-	D67G, 17.6	100
87.3	5	-	C20A, 7.7	100
-	-	100	-	100
-	-	91.7	D43B, 8.3	50,100,200
-	-	95.8	D43B, 4.2	100
-	-	83.4	D43B, 16.6	100
-	-	92.9	C30B, 7.1	100

3.2.2 *Processing conditions*

All nanocomposites were manufactured in a Leistritz LSM 30.34 intermeshing co-rotating twin-screw extruder. Fig. 3.1 shows schematically the screw profile, the barrel configuration, as well as the locations where on-line measurements were performed. For all PP and PA6 compositions, a flat barrel and die set temperature profile was adopted, at 200°C and 240°C, respectively. The throughput was fixed at 3 kg/h via a gravimetric feeder, the screw speed(s) being identified in Table 3.2.

3.2.3 *On-line rheological measurements*

For each sample, frequency sweeps from 100 to 0.1 rad/s were performed under a constant strain of 1%, at 200°C (PP matrix) or 240°C (PA-6 matrix), using parallel-plate geometry. The gap and diameter of the plates were 1 mm and 2.0 cm, respectively.

3.2.4 *X-ray diffraction (XRD) measurements*

The X-ray diffraction patterns were obtained using a Bruker diffractometer (AXS Nanostar-D8 Discover) equipped with a CuKα generator (k = 1.5404 Å) at 40 kV and 40 mA, in a 2λ range from 0.08 to 108. The organoclays were analyzed directly, whereas the nanocomposites were beforehand compression molded into disks with a diameter of 20 mm and a thickness of 4 mm.

3.3 MONITORING THE PRODUCTION OF POLYMER NANOCOMPOSITES

The effect of material and process parameters (composition and screw-speed) on the linear viscoelastic response will be discussed first, all the rheological measurements having been performed at sampling location 3 (see Fig. 3.1). Then, the evolution of the rheological behaviour along the extruder axis of some compositions will be reported.

3.3.1 *Effect of composition*

Fig. 3.2 and 3.3 illustrate the effects of the addition of filler to PP and percentage, respectively. As expected, these results show that nanocomposite melts exhibit an anomalous rheological response. PP+5%PP-g-MA behaves as a typical polymer melt, with a loss modulus (G'') larger than the storage modulus (G') throughout the frequency range analysed and slopes of approximately 1 and 2, respectively, in the terminal region. The addition of nanoclay (C20A or D67G) brings about an increase of G' particularly at low frequencies, or the development of a nonterminal plateau solid-like behavior, which is often reported and associated with the existence of a network microstructure containing solid particles [30, 31]. This increase is more noticeable for D67G. As expected, both G' and G'' increase as the amount of the nanoclay increases (Fig. 3.3). At the high frequency range, G' approaches the value of the matrix, which may be interpreted as indication that segmental motion of the polymer matrix determines the material response at short time scales [65].

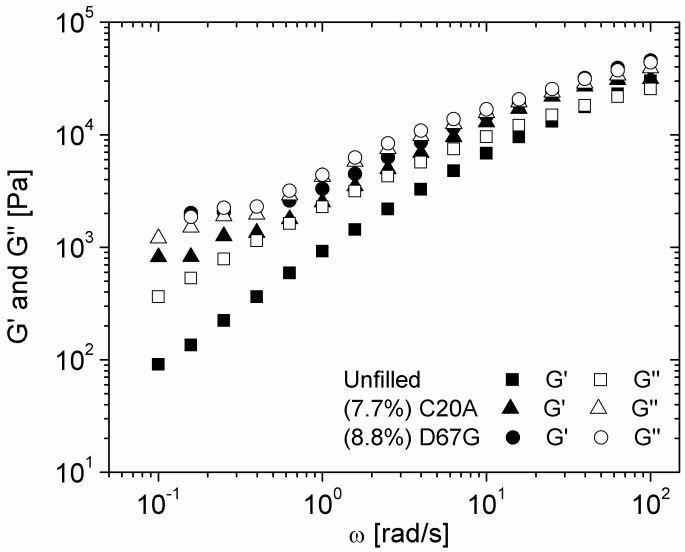

Figure 3.2: Effect of the addition and type of nanofiller for PP+5%PP-g-MA compositions.

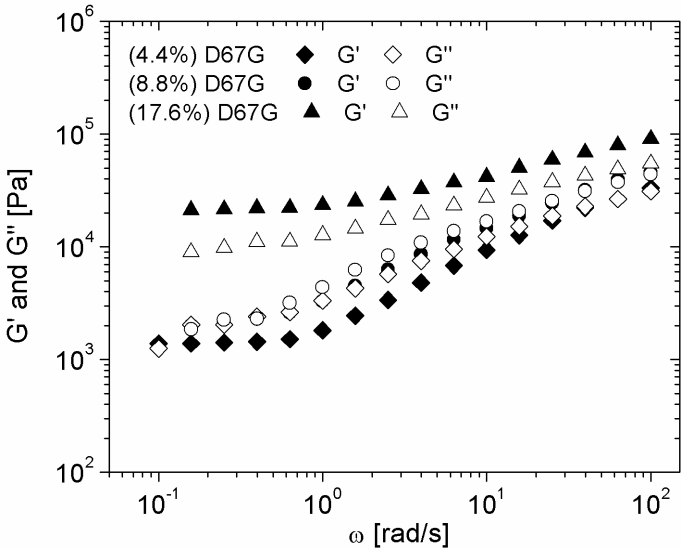

Figure 3.3: Effect of the amount of nanofiller (Dellite) for PP+5%PP-g-MA compositions.

The level of dispersion of the nanoclays in the polymer matrix was assessed by XRD. As shown in Figs. 3.4 and 3.5, which also display the XRD pattern of the fillers, the peaks corresponding to the lamellar structure of the nanoclays are still present in the nanocomposites, evidencing that the growth in elasticity was mainly obtained by melt intercalation. The lower intensity of the peak for the compositions with 4.4% of Dellite (Fig. 3.5) is due to the lower amount of nanoclay. Therefore, these results confirm the well-known difficulty of dispersing organoclays in a PP matrix, even with the addition of a compatibilizer [51, 57]. XRD and rheological data are not always coherent. The dynamic data in Fig. 3.3 for 4.4% and 17.6% DG7G show solid-like behaviour at low frequencies, unlike the 8.8% composite. XRD data in Fig. 3.5 indicates identical dispersion in all cases. In fact, XRD and rheology not only probe materials at different length scales, but also analyse quite different volumes of sample.

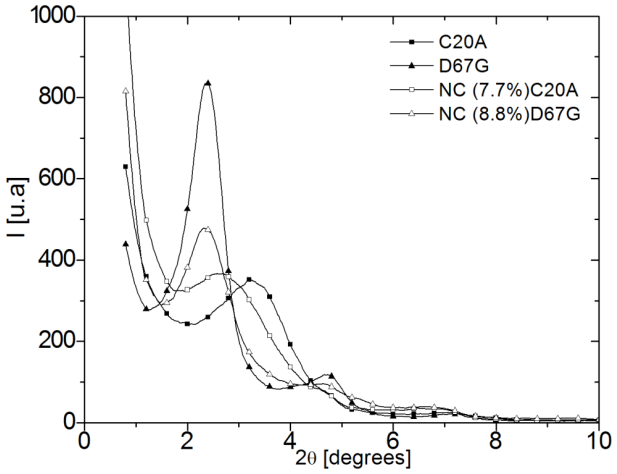

Figure 3.4: XRD of C20A, D67G, PP+5%PP-g-MA+7.7%C20A and PP+5%PP-g-MA+8.8%D67G.

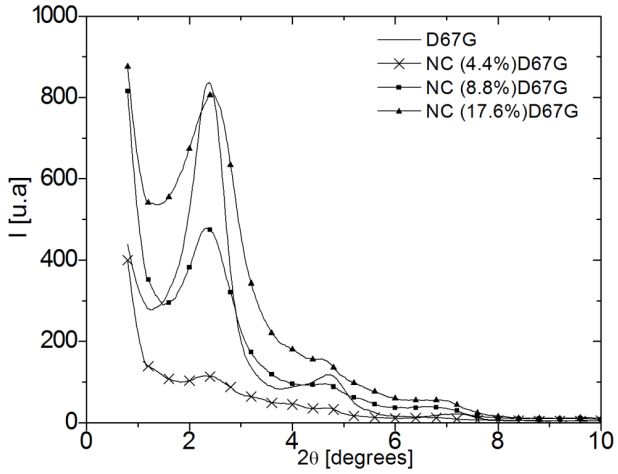

Figure 3.5: XRD of PP+5%PP-g-MA with different amounts of D67G.

Upon incorporating organoclays in PA6, similar rheological effects were observed, as seen in Figs. 3.6 and 3.7 for the type and amount of filler, respectively. As before, Dellite induces a higher raise of the moduli, especially in the low frequency range. Also, as the percentage of filler progressively increases, G' increases from values lower than G'' (at 4.1%), to values of the same order of magnitude (at 8.3%), and to $G' > G''$ and a quasi-solid behaviour at 16.6%. A comparison of Figs. 3.3 and 3.7 cannot be done, as the nanocomposites contain different grades of organoclay, due to the different polarity of the matrices. Nevertheless, it is still interesting to observe that similar levels of filler added to PP (with compatibilizer) and PA6 induce different magnitudes of the moduli, with higher values being attained for the latter. The polarity of PA6 should facilitate reaching a finer dispersion. In the case of the composite with 8.3% D43B, G' becomes lower than G'' at higher frequencies and higher than G'' at lower frequencies (Fig. 3.6), which is unusual and is difficult to account for.

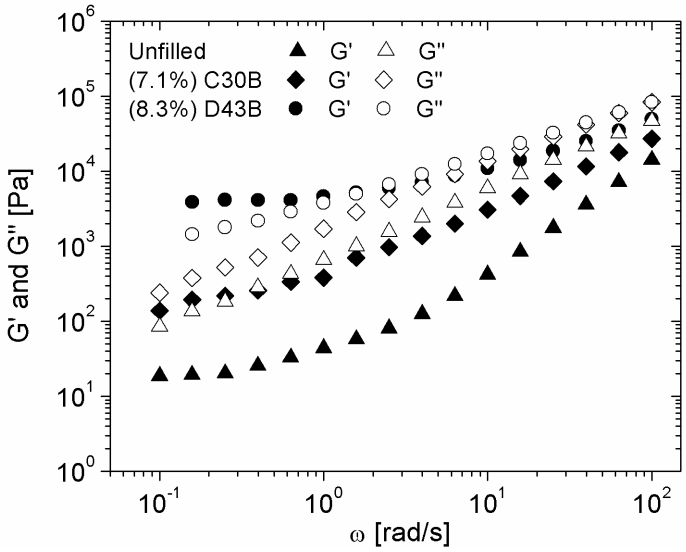

Figure 3.6: Effect of the addition and type of nanofiller for PA6 compositions.

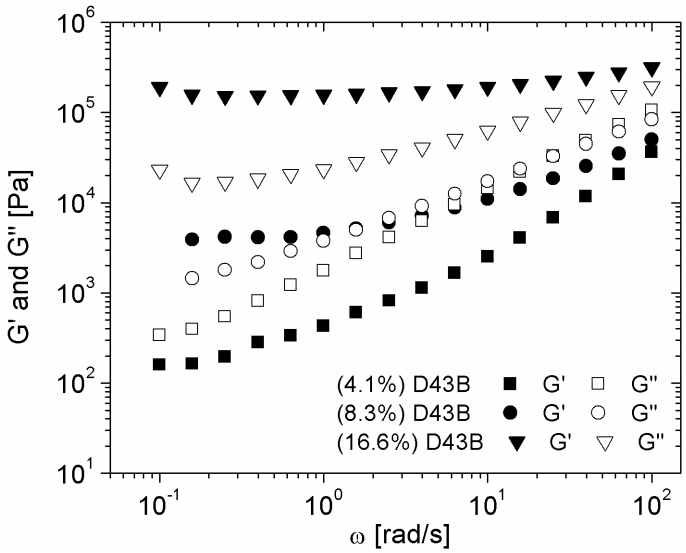

Figure 3.7: Effect of the amount of nanofiller (Dellite) for PA6 compositions.

The XRD characterization of the C30B and D43B clays and their PA6 nanocomposites is made in Fig. 3.8. In the composites, the peak corresponding to the lamellar structure of D43B disappears, while the peak concerning C30B remains, but shifted to lower angles.

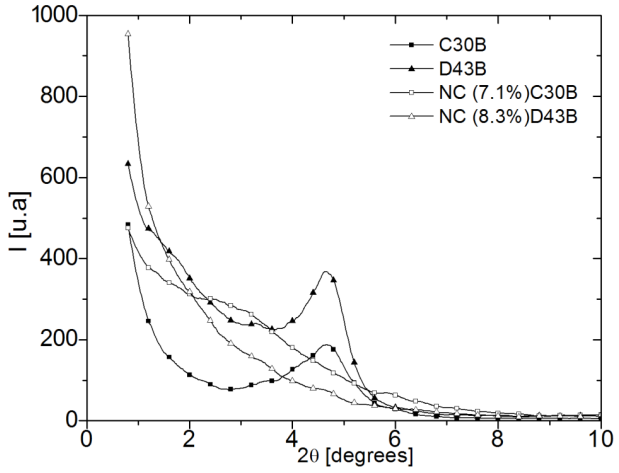

Figure 3.8: XRD of C30B, D43B, PA6+5%+7.1%C30B and PA6+8.3%D43B.

These results indicate a better dispersion of D43B than C30B, an exfoliated morphology being anticipated. This is in good agreement with the curves of Fig. 3.6, which show that the nanocomposite containing D43B has a higher G' and a better defined plateau at low frequencies.

3.3.2 *Effect of screw speed*

The effect of screw speed (at constant feed rate) on the rheological parameters of the PP and PA6 nanocomposites is illustrated in Figs. 3.9 and 3.10,

respectively. No direct correlation seems to exist between G' and G'' and screw speed. Nevertheless, in both cases the highest dispersion (higher G') is achieved at the highest screw speed tested. For PP+PP-g-MA+C20A nanocomposites, Vergnes [51] found out that the state of intercalation is globally unaffected by the processing parameters (independent variation of feed rate and screw speed), but the level of exfoliation grows when the feed rate decreases and the screw speed increases. In fact, dispersion should result from the creation of sufficiently high hydrodynamic stresses during enough time [66, 67].

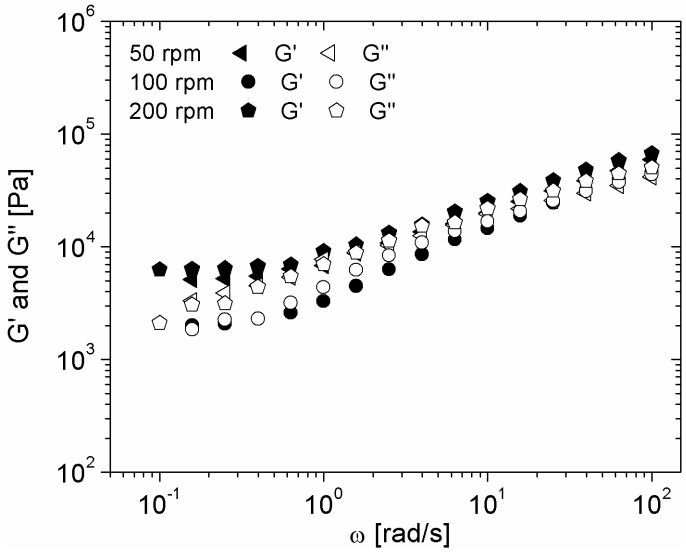

Figure 3.9: Effect of screw speed on G' and G'' of PP+5% PP-g-MA+8.8% D67G.

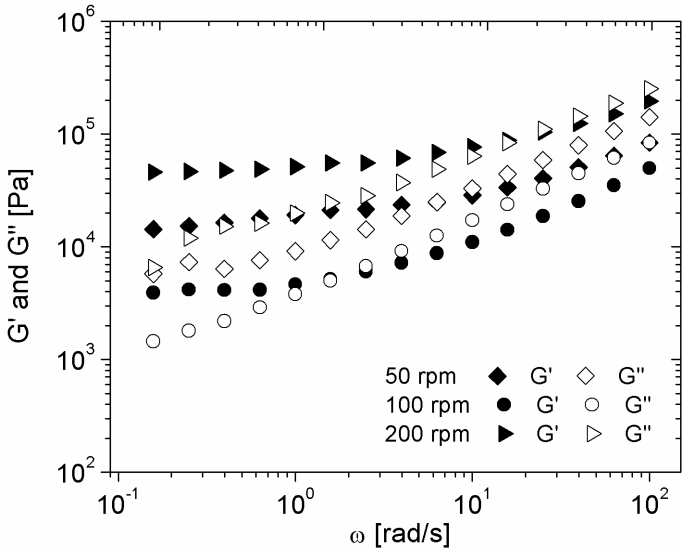

Figure 3.10: Effect of screw speed on G' and G'' of PA6+8.3% D43B.

Upon increasing the screw speed the shear intensity escalates, but the residence time for flow is reduced. The rheological properties of the components and the screw profile also play a role. Thus, monitoring the evolution of dispersion along the extruder axis could assist in better understanding the influence of processing conditions on dispersion.

3.3.3 *Measurements along the extruder axis*

The evolution of the moduli of the PP and D67G nanocomposite (relative to the unfilled polymer) is shown in Fig. 3.11 at three frequency values. As expected, G' and G'' increase along the extruder up to L/D = 20, as a consequence of increasing dispersion. Most probably the rise is not linear, most of the dispersion taking place upon melting [51]. Surprisingly, a decrease between locations 2 and 3 was measured, which cannot be attributed to matrix degradation as shown in [68]. Similar results were reported by [57], no explanation being offered.

The rheological measurements performed on an equivalent PA6 composition followed a similar trend (see Fig. 3.12). However, in this case the downstream deterioration of G' and G'' can be attributed to matrix degradation [58]. Nonetheless, it is interesting to point out that before degradation sets in an increase of the storage modulus of circa 400 times was observed, i. e., extensive dispersion is achieved.

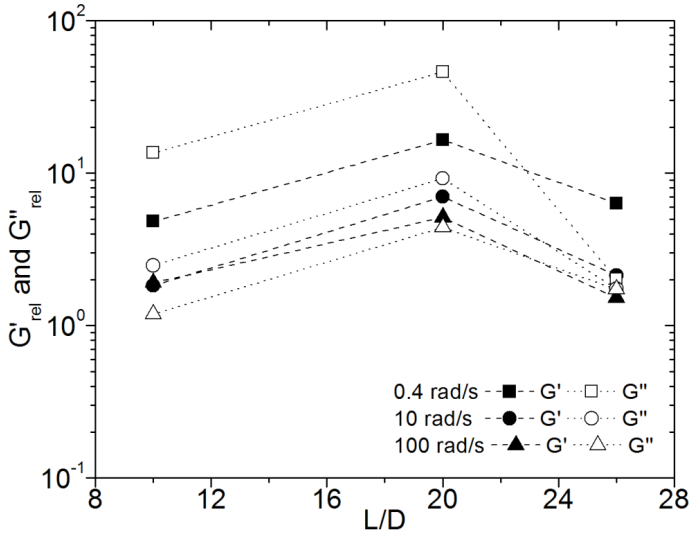

Figure 3.11: Evolution of G' and G'' of PP+5%PP-g-MA+8.8%D67G along the screw axis.

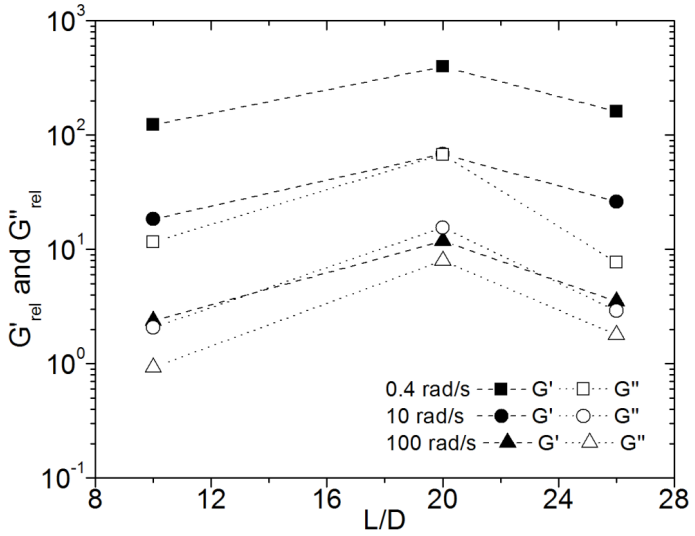

Figure 3.12: Evolution of G' and G'' of PA6+8.3% D43B along the screw axis.

3.4 CONCLUSIONS

The prototype on-line oscillatory rheometer employed is sensitive to changes in morphology that result from variations in material, composition and processing conditions.

The addition of nanofillers promotes a significant increase of the linear viscoelastic moduli, particularly at low frequencies, that grows with dispersion and filler content. In general, the rheological data could be correlated with off-line XRD spectra. Changes in screw speed induce a complex rheological material response, due to the interplay between hydrodynamic stresses, residence time and velocity fields, with the possibility of material degradation also playing a part. Measurements along small axial increments of the twin screw extruder would contribute to clarify this topic.

In general, the results demonstrate the practical utility of the new on-line device for research, quality control and optimization of the manufacture of polymer nanocomposites by melt compounding.

4

PREPARATION OF POLYMER-CLAY NANOCOMPOSITES BY MELT MIXING IN A TWIN SCREW EXTRUDER: USING ON-LINE SAOS RHEOMETRY TO ASSESS THE LEVEL OF DISPERSION

4.1 INTRODUCTION

Academic and industrial research on the preparation, properties and applications of polymer-clay nanocomposites has been intense, as attested by the numerous reviews published in the last years [39, 47, 69–82]. Presently, considerably improved mechanical performance, thermal stability, barrier characteristics and fire retardation properties of a given polymer can be obtained at very low clay loadings. Increased biodegradability of biodegradable polymers has also been reported [83]. Although different approaches have been utilized for the preparation of these materials, namely *in situ* template synthesis by sol-gel technology, *in situ* intercalative polymerization, solution intercalation, or melt mixing, the latter seems to be preferred method in practice. Particularly when using twin screw extruders, it is possible to generate the stresses and times required for diffusion of the polymer inside the confined spaces between clay lamella (intercalation), as well as the high levels of shearing necessary for exfoliation [84]. Also, the process is continuous, environmentally benign, allows the use of polymers which are not suitable for the other preparation routes and can be adapted to the specificities of a given material or process due to the modular construction of twin screw extruders [37, 77, 80].

The performance of a polymer-clay nanocomposite is determined by the composition, properties of its ingredients, chemical affinity between polymer and organoclay and processing conditions (screw profile, operating conditions, feeding sequence), as most of these parameters will influence evolution of dispersion and its final level. The effect of processing conditions has been extensively investigated [51, 57, 85–94]. This influence implies that during practical compounding stringent process control and periodic monitoring of the characteristics of the nanocomposite being manufactured are imperative.

On-line and in-line monitoring techniques are particularly attractive for this purpose. Optical and spectroscopic methods have been applied to assess the extent of exfoliation in polymer-clay nanocomposites. Optical transmission measurements showed that transmission increases with increasing extent of exfoliation, because light scattering due to the presence of clay aggregates reduces [95, 96]. It was observed that the development of an exfoliated structure results in an intense increase of fluorescence [97, 98]. However, the technique used required that the fluorescent tracer (Nile blue) was incorporated into the clay galleries before compounding. In-line near-infrared spectroscopy, together with appropriate chemometrics using off-line data, pro-

vided a good correlation with dispersion [99, 100]. On-line dielectric relaxation spectroscopy revealed that clay fillers impact on nearly all relaxation processes changing both the characteristic frequency and strength of the relaxation [95, 101]. Recently, Kracalik et al. [102] subjected the nanocomposites emerging from the die to a Rheotens (Göttfert Ltd., Buchen, Germany) extensional experiment and demonstrated that the sensitivity of melt strength correlates well with dynamic rheological data measured by rotational rheometry.

Together with transmission electron microscopy (TEM) and X-ray diffraction (XRD), rotational rheometry (in small amplitude oscillatory shear, SAOS) is frequently used to assess dispersion in polymer-clay nanocomposites. In a storage modulus (G') versus frequency plot, an increase of G' at low frequency is usually interpreted as evidence of greater dispersion [51, 93, 103–106]. The exponent of a power law fitted to the variation of complex viscosity ($|\eta^*|$) with frequency was shown to increase with dispersion [104, 105]. The growth in melt yield stress (σ_0) was related to an intensification of clay exfoliation [51, 57, 62, 93].

Therefore, the use of on-line rotational rheometry to monitor the preparation of polymer-clay nanocomposites by melt mixing seems of significant practical interest. Although an isothermal frequency sweep in SAOS typically takes several minutes, the technique remains suited for process monitoring due to the richness of the information provided, at least during the initial process development and optimization stages. Such a rheometer was previously developed and experimentally validated [10], an improved version with automated operation has been introduced in Chapter 2. Since the device was designed to perform measurements at various locations along the barrel of the extruder, it was successfully used to provide data on the axial evolution of dispersion of polymer-clay nanocomposites [107]. In this chapter, the on-line rheometer is fixed between an industrial extruder and a multi-rod die and the capacity to discriminate the effects of changes in clay type and content, screw speed and feed rate are investigated, as a requirement for process monitoring ability. The analysis is supported by XRD and electron microscopy data.

4.2 EXPERIMENTAL

4.2.1 *Materials*

The materials used in this work, a general purpose commercial polypropylene homopolymer (PP), a compatibilizer (polypropylene grafted with maleic anhydride, PP-g-MA) and two commercial natural montmorillonite clays modified with a quaternary ammonium salt, are presented in Table 4.1. A stabilizer pack was also incorporated. The compositions of the nanocomposites prepared are identified Table 4.2.

Table 4.1: Materials used in this chapter.

Designation	Material	Grade	MFR
PP	Polypropylene	LyondellBasell Moplen HP500N	12 g/10 min (230°C/2.16 kg)
PP-g-MA	Polypropylene-grafted -maleic anhydride	Crompton Polybond 3200	115 g/10 min (190°C/2.16 kg)
D67G	Montmorillonite	Laviosa Dellite 67G	–
C20A	Montmorillonite	Southern Clay Cloisite 20A	–

Table 4.2: Compositions and corresponding operating conditions.

PP wt.%	**PP-g-MA** wt.%	**Dellite 67G** wt.%	**Cloisite 20A** wt.%	**Stabilizer** wt.%	**Operating conditions**
94.2	5	-	-	0.8	300 r.p.m., 50 kg/h
89.2	5	-	5.0	0.8	300 r.p.m., 50 kg/h
86.5	5	-	7.7	0.8	300 r.p.m., 50 kg/h
86.5	5	-	7.7	0.8	230 r.p.m., 50 kg/h
86.5	5	-	7.7	0.8	150 r.p.m., 50 kg/h
86.5	5	-	7.7	0.8	300 r.p.m., 40 kg/h
85.4	5	8.8	-	0.8	300 r.p.m., 50 kg/h

4.2.2 *Experimental setup*

All materials were prepared in a Maris TM45 twin-screw extruder (screw diameter, D =45 mm, length to diameter ratio, L/D =36). The screws con-

tained four mixing zones consisting of staggered kneading disks (proprietary design). Polymer and filler were fed separately by gravimetric feeders. The barrel and die set temperature were kept constant at 180°C, while screw speed and feed rate were varied as shown in Table 4.2. During the experiments, melt temperature at the die ranged between 210 and 221°C, melt pressure between 8.6 and 12 bar and motor amperage between 25 and 41 A.

On-line rheological measurements were performed between extruder and die, after diverting the required amount of melt to the device. The set-up has been validated in Chapter 2. The extrudate was cooled down in water and pelletized, samples being collected for off-line rheological, structural (XRD) and morphological (SEM and TEM) characterization. Fig. 4.1 illustrates the experimental set-up.

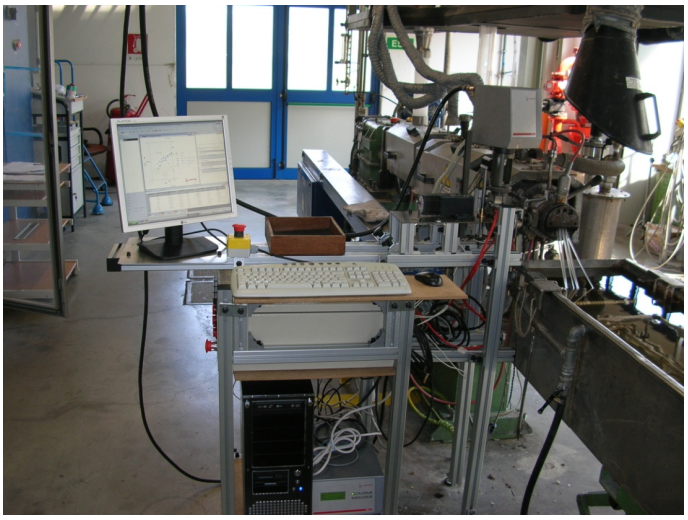

Figure 4.1: Experimental set-up.

4.2.3 *Characterization*

ON-LINE OSCILLATORY RHEOMETRY. As most rotational rheometers, the prototype can operate in various modes, but only SAOS experiments were performed. In order to make a measurement, the melt is diverted from the main stream (between extruder and die) by means of an adapter connecting it to the testing chamber of the rheometer. Once sufficient material sample has been collected, the incoming flow is interrupted by rotating a valve. The operation takes approximately 12-15 seconds and creates negligible shear rates, to prevent changes in morphology. As described in detail in Chapter 2, an automatic sequence is then initiated, comprising squeezing the sample between the parallel plates (with a diameter of 20 mm) until the pre-defined gap (1 mm) is obtained, and wiping the excess material around the plates by sliding a cleaning ring. The rheological test starts when the sample reaches thermal equilibrium at the experiment set temperature (due to the difference between inlet melt temperature and set value of 200°C, equilibration time varied be-

tween 3 and 4 minutes). For each sample, frequency sweeps from 100 to 0.1 rad/s were performed under a constant strain of 1%.

OFF-LINE OSCILLATORY RHEOMETRY. Tests were performed in a strain controlled ARG2 (TA Instruments) using parallel plates with a diameter of 25 mm and a 1 mm gap. The discs were manufactured by compression molding at 200°C. In the same way of the on-line tests, isothermal at 200°C frequency sweeps from 100 to 0.1 rad/s were performed for each sample under a constant strain of 1%.

X-RAY DIFFRACTION. Diffraction patterns were obtained using a AXS Nanostar-D8 Discover diffractometer (from Bruker) equipped with a CuKα generator (λ = 1.5404 Å) at 40 kV and 40 mA, in a 2θ range between 0.08 and 10°. The organoclays were analyzed directly, whereas the nanocomposite samples were previously compression molded into disks with a diameter of 20 mm and a thickness of 4 mm.

ELECTRON MICROSCOPY (SEM AND TEM). Samples for scanning electron microscopy (SEM) were beforehand embedded in a resin, subjected to a lapping procedure to obtain a flat surface, and coated with a gold thin film. The analysis of 3 mm^2 of each sample was performed in a Leica Cambridge S360 microscope. Transmission electron microscopy (TEM) microphotographs were taken of samples with a thickness of 70 nm, cut using a diamond knife of a Leica ultramicrotome at -60°C. The cut sections were transferred onto copper grids and then examined without staining in a Philips CM120 TEM. The Equivalent Circle Diameter (ECD) was quantified on a 0.2 mm^2 area using an Image Analysis software interpolation. The Specific Tactoids Dispersion (STD) was determined as the number of clusters per unit area and per unit filler concentration; the error associated with the measurements is around 10%.

4.3 MONITORING THE PRODUCTION OF POLYMER NANOCOMPOSITES

The effect of material and process parameters (composition and screw-speed) on the linear viscoelastic response will be discussed first, all the rheological measurements having been performed at sampling location 3 (see Fig. 3.1). Then, the evolution of the rheological behaviour along the extruder axis of some compositions will be reported.

4.4 RESULTS AND DISCUSSION

4.4.1 *On-line vs. off-line measurements*

Fig. 4.2 compares the on-line and off-line rheological data (complex viscosity, $|\eta^*|$, and storage modulus, G') obtained for the nanocomposite with Dellite 67G, i. e., PP+5%PP-g-MA+7.7%D67G. The agreement seems good, similar differences having been obtained for the remaining samples. Earlier work

[10, 68] showed that the average deviation between the results obtained on-line and off-line for various commercial polymer melts, polymer blends and polymer-clay nanocomposites varied between 3 and 13%. Frequently, in the case of polypropylene-based systems, the moduli measured on-line were a little higher than those measured off-line. This was attributed to degradation of the samples measured off-line, as they are subjected to additional thermal cycles required for manufacturing discs and heating them up to the test temperature. Since the system used here was stabilized, the above feature is not present in Fig. 4.2. In the remaining of this work, only on-line rheological data will be presented.

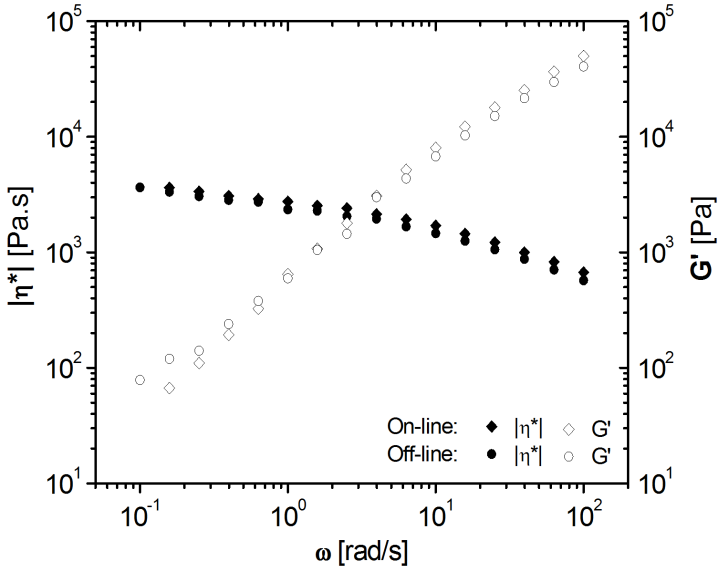

Figure 4.2: On-line vs. off-line rheological data for PP+5%PP-g-MA+7.7%D67G.

4.4.2 *Effect of clay type*

The effect of changing clay type on the measured rheological properties is depicted in Figure 4.3. Both curves show an increase of G' at low frequencies, but Cloisite 20A exhibits higher values than Dellite 67G. This would indicate *a priori* that a better dispersion was achieved with the former.

Even though the two organoclays have the same surfactant (dimethyl dihydrogenated tallow ammonium, 2M2HT), Cloisite 20A has lower particle size (its initial average particle size is 5 μm, while that of Dellite 67G is approximately 9 μm [69]. The XRD diffractograms of Fig. 4.4 indicate that the initial basal spacing of C20A is smaller than that of D67G (2.7 nm versus 3.7 nm, as estimated using Bragg's law [57]. The net result of processing under identical conditions is also indicated in Fig. 4.4: while for C20A the clay interlayer spacing increased to 3.0 nm, thus indicating that some degree of intercalation was achieved, the value of 3.4 nm for D67G points towards little intercalation, or

even collapse of the clay galleries. In any case, these results are coherent with the rheological data.

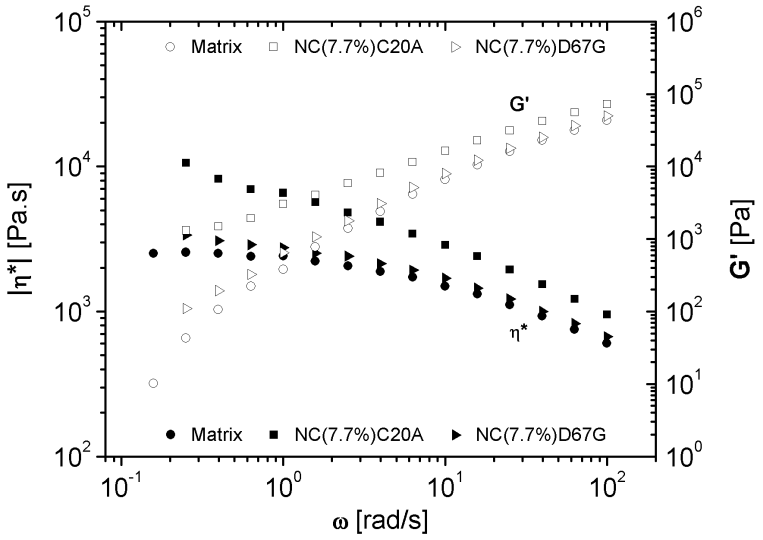

Figure 4.3: On-line rheological data for PP+PP-g-MA (matrix), PP+5%PP-g-MA+7.7%D67G (NC(7.7%)D67G) and PP+5%PP-g-MA+7.7%C20A (NC(7.7%)C20A).

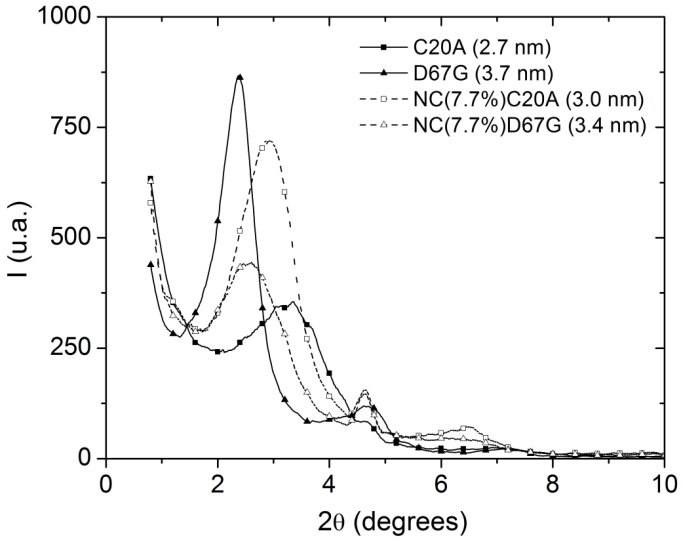

Figure 4.4: XRD diffractograms of C20A, D67G, PP+5%PP-g-MA+7.7%C20A (NC(7.7%)C20A) and PP+5%PP-g-MA+7.7%D67G (NC(7.7%)D67G).

Morphological analysis by SEM (Fig. 4.5) and TEM (Fig. 4.6) corroborates these observations. The white zones in the SEM micrographs of Fig. 4.5 are clay agglomerates and the dark background is the PP/PP-g-MA matrix. Agglomerates are clearly smaller and more homogeneous in the system prepared with C20A. Fig. 4.6-a (composite containing C20A) shows that the stacked layer structures are thinner than in Fig. 4.6-b. For C20A, the number of tac-

toids per unit area is 90 and the specific tactoids dispersion (STD) is 12, whilst for D67G the corresponding values are 152 and 17, respectively.

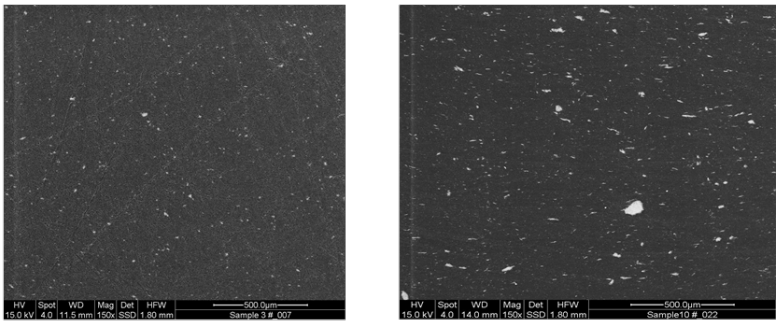

Figure 4.5: SEM micrographs of a) PP+5%PP-g-MA+7.7%C20A and b) PP+5%PP-g-MA+7.7%D67G.

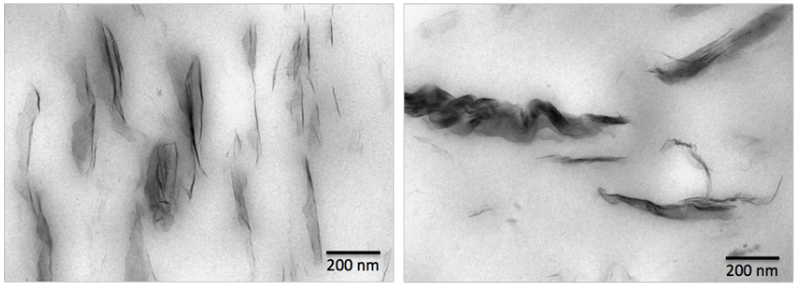

Figure 4.6: TEM micrographs of a) PP+5%PP-g-MA+7.7%C20A and b) PP+5%PP-g-MA+7.7%D67G.

4.4.3 *Effect of clay content*

Fig. 4.7 depicts the effect of altering clay content from 5 to 7.7 wt.% on complex viscosity and storage modulus of the nanocomposites. As expected, not only the global values of the rheological parameters increase, but the plateau of G' at low frequency seems more prolonged. These changes could result directly from differences in organoclay loading, but alterations in the extent of dispersion could also make a contribution. After correcting the hydrodynamic effect due to the filler amount (vertical shift of the complex viscosity curves), the values of the apparent melt yield stress were determined as 477 and 1257 Pa for the samples with 5 wt.% and 7.7 wt.%, respectively, i. e., a better dispersion seems to be achieved with 7.7 wt.%.

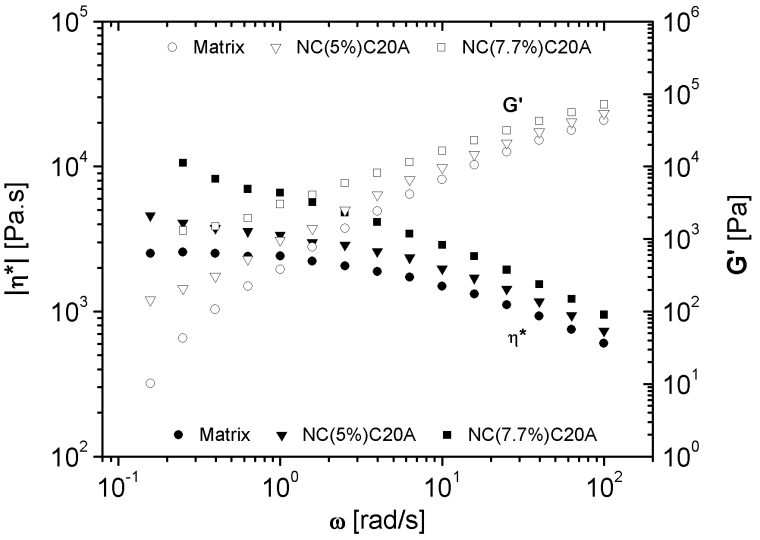

Figure 4.7: On-line rheological data of PP clay-nanocomposites containing different clay content (5 and 7.7% C20A).

Opposite results were obtained with other techniques. As seen in Fig. 4.8, the lamellar distance of the nanocomposite prepared with 5 wt.% of C20A is somewhat higher than that having 7.7 wt.% (3.4 nm versus 3.0 nm). From TEM micrographs, the corresponding number of tactoids per unit area is 44 and 90, respectively, and STD is 9 and 12. These values being smaller for the nanocomposite prepared with less clay, they also indicate better dispersion. While XRD and TEM analyze the extent of dispersion in a small area of the sample (the former in terms of intercalation, the latter detecting both intercalation and exfoliation), rheology is sensitive both to dispersion and filler content, which could explain the different conclusions.

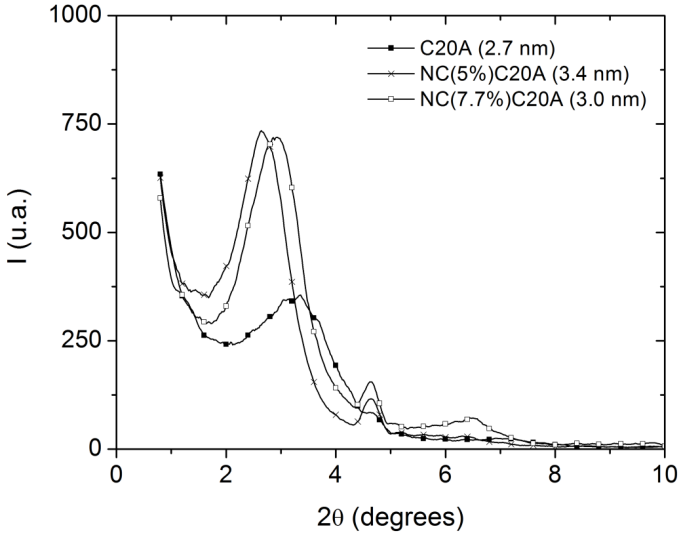

Figure 4.8: XRD diffractograms of PP-clay nanocomposites containing different clay content (5 and 7.7% C20A).

4.4.4 *Effect of feed rate*

Shifting the feed rate from 40 to 50 kg/h does not seem to produce meaningful differences in the linear viscoelastic response of the material (Fig. 4.9). This apparent insensitivity is confirmed by XRD (Fig. 4.10), which points to comparable lamellar distances for the two nanocomposites (2.9 nm for the one produced at 40 kg/h, 3.0 nm for that manufactured at 50 kg/h). Similarly, SEM micrographs (Fig. 4.11) exhibit equivalent morphologies. TEM analysis indicated that the nanocomposite prepared at 40 kg/h presented a lower number of tactoids per area and a lower STD (60 and 8, respectively for the sample produced at 40 kg/h, as opposed to 90 and 12, respectively, at 50 kg/h). This effect is in line with most previous studies, which report that lower feed rate values improve exfoliation levels because of the corresponding increase of residence time [51, 54, 57, 93].

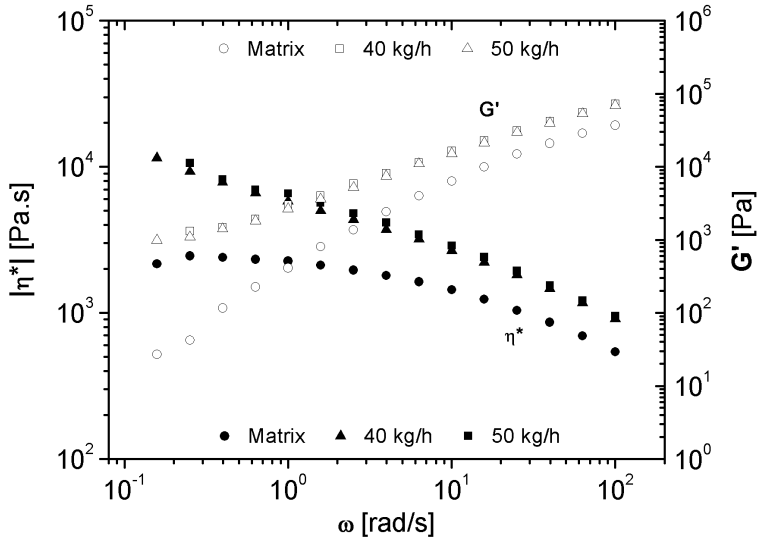

Figure 4.9: On-line rheological data of PP clay-nanocomposites prepared using different feed rates.

4.4.5 *Effect of screw speed*

According with the rheological data plotted in Fig. 4.12, the nanocomposite prepared at the medium screw speed (230 r.p.m.) appears to be better dispersed than the remaining (150 and 300 r.p.m.), which present a similar response (the Apparent Yield Stresses for 150, 230 and 300 r.p.m. are 1259, 1710 and 1386 Pa, respectively). The rheological measurements seem to be more sensitive than XRD (Fig. 4.13), which indicates equivalent lamellar distance regardless of the screw speed. Similarly, SEM micrographs (not shown) indicated similar dispersion for all samples. However, from TEM observations the number of tactoids per unit area and STD for the samples prepared at 150 and 300 r.p.m., were calculated as 98 and 90, and 13 and 12, respectively, i. e., within experimental

accuracy, the nanocomposites show comparable dispersion levels.

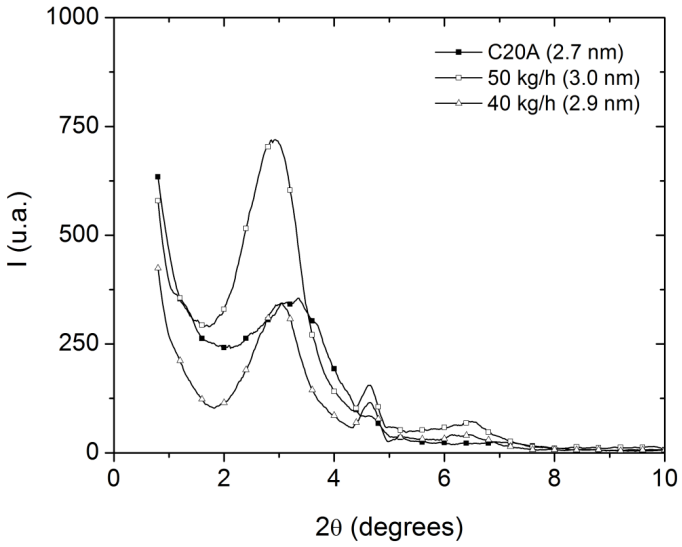

Figure 4.10: XRD diffractograms of PP clay-nanocomposites prepared using different feed rates.

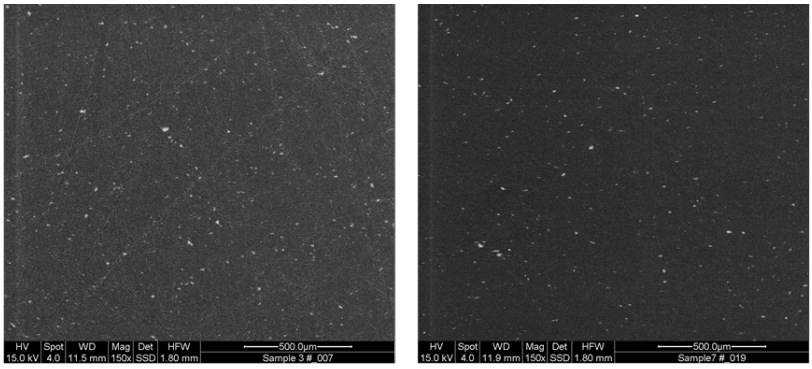

Figure 4.11: SEM micrographs of PP-clay nanocomposites prepared with different feed rates (left: 40 kg/h; right: 50 kg/h).

Screw speed is usually reported to promote dispersion [51, 54, 57, 86, 88, 89, 92, 93] due to the greater intensity of the hydrodynamic stresses created by the higher shear rates, that should particularly promote exfoliation. This would explain why XRD diffractograms, being mostly sensitive to intercalation, remained similar. However, high screw speeds could eventually promote degradation of the surfactant and, eventually, of the polymer, causing a decrease of the viscosity [91, 108]. In fact, as seen in 4.12, the complex viscosity for the nanocomposite prepared at 300 r.p.m. is lower than the remaining.

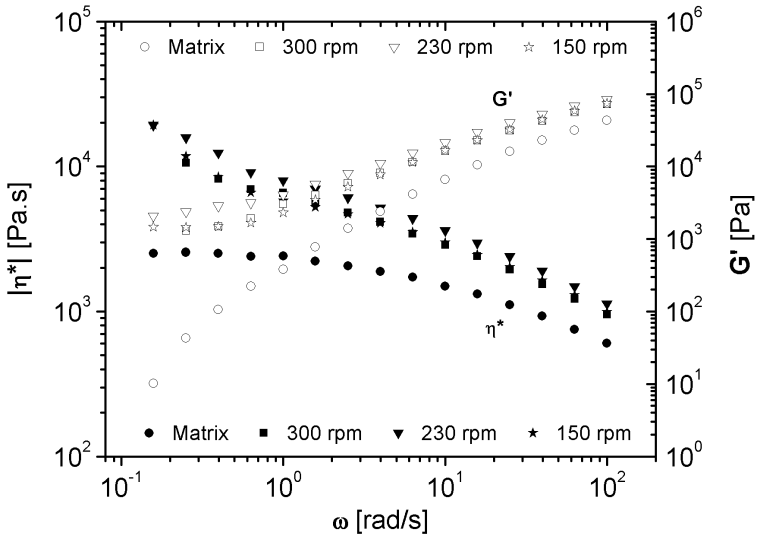

Figure 4.12: On-line rheological data of PP-clay nanocomposites prepared using different screw speeds.

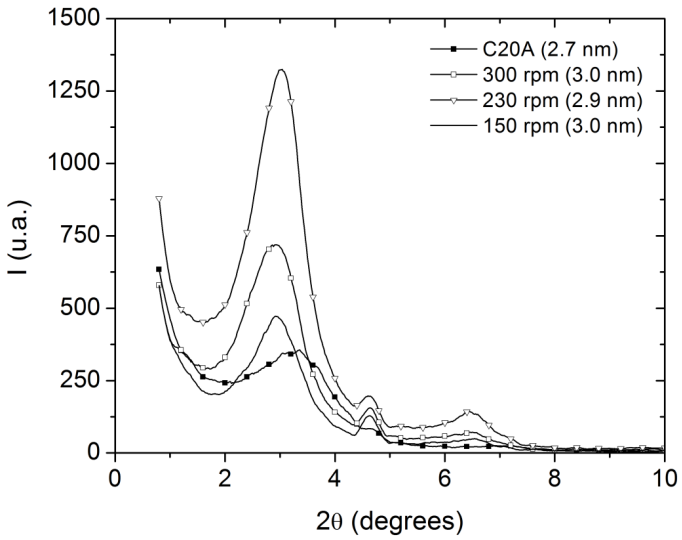

Figure 4.13: XRD diffractograms of PP-clay nanocomposites prepared using different screw speeds.

4.5 CONCLUSIONS

The linear viscoelastic response of a polymer-clay nanocomposite is frequently utilized to estimate the extent of dispersion of the clay in the matrix. Therefore, on-line rotational rheometry seems interesting to monitor the preparation of polymer-clay nanocomposites, with a view to process development and/or monitoring. This work investigated whether the technique would be sensitive to a change of clay type and to moderate changes in clay content, feed rate and screw speed.

First, it was shown that equivalent on-line and off-line rheological data showed good agreement. Rheology exhibited at least the same sensitivity of the other well-known characterization methods utilized to assess dispersion, electron microscopy (SEM and TEM) and X-ray diffraction, with obvious practical advantages. The trends observed by the various techniques were generally identical, particularly between rheology and TEM, given the sensitivity of the two techniques to both intercalation and exfoliation.

Part III

COMPUTATIONAL MODELLING

This part is reproduced from:

- S. T. Mould, R. Toth, P. Posocco, S. Pricl, M. Fermeglia, J.A. Covas, and J. M. Nóbrega. Mesoscopic simulations of polymer solutions: effect of the coarse-graining level on the structural and dynamical properties. *TO BE SUBMITTED*
- S. T. Mould, J. A. Covas, and J. M. Nóbrega. Non-equilibrium dissipative particle dynamics simulations of polymers undergoing steady and unsteady shear flows: the role of the friction parameter on the time scalability. *TO BE SUBMITTED*
- S. T. Mould, J. A. Covas, and J. M. Nóbrega. Towards a multiscale approach to predict the large-scale morphology of polymer/layered-silicate nanocomposites. *TO BE SUBMITTED*

5

MESOSCOPIC SIMULATIONS OF POLYMER SOLUTIONS: EFFECT OF THE COARSE-GRAINING LEVEL ON THE STRUCTURAL AND DYNAMICAL PROPERTIES

5.1 INTRODUCTION

Since the appearance of bakelite in the early twentieth century, many polymeric materials emerged in order to satisfy the needs of a challenging market. Their variety is outstanding (e. g., thermoplastics, dispersions, colloids, rubbers, thermosets, etc) and their properties can be easily tailored by controlling their chemistry, structure and processing. Unfortunately, the theoretical understanding and ability to predict the performance of these materials as lagged behind the practical advances.

It is well-known that atomistic simulations (either performed using *molecular dynamics*, MD, or *Monte Carlo*, MC simulations) can accurately predict the properties of some systems. However, the performance of polymeric materials is highly dependent on their inherent large dimensions and prolonged relaxations times, which are in general difficult to cope with by such methods at an affordable computational cost. To overcome this problem, many authors proposed coarse-grained models, which have the potential to accurately reproduce the systems detailed structure and dynamics. Several schemes have been suggested, some being based on parameter adjustments to relate the results of simulations with experimental data [109], while others, rely on the idea of *message passing* through scales, i. e., the parameters for the coarse system are obtained from lower scale (e. g., atomistic) simulations [110–114].

Theoretical scaling laws are commonly related to dimensions consistent with the Kuhn monomer [115, 116]. At this length scale, coarse-grained united-atom models are able to mimic most of the subtleties of a real system. For instance, particles may represent single monomers, functional groups, or even groups of small molecules of a solvent. Many systems have been studied, including *n*-alkanes [117], flexible polymers [109, 118–120], polymers with tacticity [121–123], polymers with a rigid backbone [124–126], polymer brushes [127], and dendrimers [128]. Despite the computational cost, some authors took the coarse-graining idea further, by averaging position and momenta of large amounts of atoms onto mesoscopic entities, thus extending the length and time scales accessible with these simulations. The averaged internal degrees of freedom are represented as fluctuations provided by a stochastic term combined with dissipative forces to correct the dynamics. The theoretical basis is described by the Mori-Zwanzig formalism [129, 130], which derives the equations of motion of coarse-grained systems by means of a projector operator ansatz. The formalism has been generalized to other mesoscopic models [131] such as *Brownian Dynamics* (BD) and *Dissipative Particle Dynam-*

ics (DPD). The components of the system free-energy can be evaluated from atomistic simulations by a general method such as the *potential of mean force*. Creating such a simple scheme for polymers is a difficult task, since features like chemical composition and architecture are fingerprints that affect their intrinsic properties. The development of strategies that preserve such detailed information on a coarse manner is definitively a challenge. Still, detailed analyses of structural, dynamic and rheological properties have been performed [2, 132–135].

In a mesoscopic framework, length scales are of the order of several monomers and the predictions given by theory are scarcely applicable. The level of coarse-graining being an arbitrary choice, questions remain about its influence on the scaling laws and its role in preserving the characteristics of the underlying atomistic system. Apparently, only Guerrault et. al. [133] addressed this issue for a systematic multiscale approach. This work aims at providing a more detailed insight on the influence of coarse-graining level on the structural and dynamical properties of a linear polyethylene (PE) system. The study begins with detailed atomistic MD simulations, in order to gather the information needed to estimate the mesoscopic interactions for three distinct coarse-graining levels. Combinations of these interactions allowed to characterize the Hamiltonian of the material in the mesoscopic simulations. Coarse-grained simulations are then carried out using the DPD model of Hoogerbrugge and Koelman [136], due to its versatility to model the mesoscopic details of complex fluid systems, has been successfully adopted in a variety of scientific niches (e. g., polymer science, rheology and biophysics). Since a single stochastic force between particles is required, local momentum is conserved and hydrodynamics effects appear naturally in the model. The friction parameter also plays an important role on the simulations time scale mapping [137, 138] and, consequently, the magnitude of the dynamical properties. To evaluate the dependence of the scaling laws on coarse-graining, the predictions are compared with theory, simulations and experimental data obtained in the literature.

This chapter is organized as follows. Section 5.2 presents the methodology used for the atomistic simulations of all-atom PE. This involves 3D periodic cell construction, energy minimization, density equilibration and production runs. The steps for the generation of the mesoscopic force field are summarized in Section 5.3. In Section 5.4), which is dedicated to the mesoscopic framework, the DPD model is briefly described. The factors required to convert physical to reduced units are also presented, together with the coarse-grained systems and simulation parameters. Section 5.5 discusses the results, starting from static properties from local structural details given by the distribution functions, to global chain dimensions. The global dynamics are studied in terms of the mean-square displacements and the time-mapping necessary to tune the mesoscopic time scale. The dynamical analysis is further extended to the local details provided by the relaxation modes. The discussion is concluded with an analysis of the effect of the molecular weight on the system dynamics and self-diffusion coefficient. Finally, Section 5.6 summarizes the work and highlights the major conclusions.

5.2 ATOMISTIC SIMULATIONS

The driving forces governing *intra-* and *inter*-molecular interactions are given by the COMPASS force field (FF) [139]. This FF belongs to the group of Class-II force fields, that is parameterized via an analytic representation of the *ab initio* potential energy surface and further optimized empirically to yield good agreement with experimental data. Since it is computationally prohibitive to simulate real polymer chains at this level of detail, the assumption that much shorter chains possess some of the properties of corresponding high molecular weight chains needs to be made. In fact, experimental results showed that bulk polyethylene develops a constant density of 0.76 g/cm^3 at 450 K for chains with at least 28 constitutive repeating units [140, 141]. Accordingly, at this density and temperature, a 3D periodic cubic cell was built, containing the initial conformations of ten distinct well equilibrated chains, each with a degree of polymerization $DP = 100$ (≈2800 g/mol), using the protocol originally proposed by Theodorou and Suter [142], as implemented in the *Amorphous Cell builder* module of *Materials Studio* (v.*5.0, Accelrys, San Diego*).

A chain containing 100 monomers is obviously rather short. For PE, neutron spin echo experiments showed that the entanglement molecular weight appears to be slightly lower than the molecular weight of the chains considered here [4, 143, 144]. Yet, simulations have shown that for the same molecular weight, entanglements influence the polymer dynamics only marginally [1]. In order to relax the system energy, ten simulated annealing cycles were performed, each cycle consist of: i) temperature equilibration at 450 K under the canonical ensemble (NVT) conditions; ii) system heating and equilibration at 800K; iii) system cooling back to 450 K; iv) system energy minimization. The MD runs were carried out using the Berendsen thermostat [145] with a time-step of 1 fs during 500 ps per heating/cooling stage. Long-range electrostatics were dealt with the Ewald summation scheme [146] and the minimization algorithm used was the Hessian-free truncated Newton algorithm [147], with stopping tolerances of 10^6 kcal and 10^8 N, for energy and force, respectively. After each minimization step the total energy was computed and the topology stored. The topology corresponding to the lowest energy was selected for further MD simulations in the isothermal-isobaric (NPT) ensemble using the Nosé-Hoover thermostat/barostat, to yield the equilibrium density at atmospheric pressure (1 bar) and 450 K. After five runs (i. e., 250 ps) a value of 0.766 g/cm^3 was obtained, which is in good agreement with both experiments [141] and previous simulations [148]. Simulations at other temperatures performed using the same method produced the results shown in Table 5.1, which also well compare with experimental data [149].

Once the equilibrium density was attained, the final production run was performed for 80 ns at 450 K in order to evaluate the system dynamics. To avoid possible artifacts influencing the atomic trajectories, the simulation was carried out at equilibrium (NVE) conditions. The thermodynamics were carefully monitored along the entire simulation to detect the eventual occurrence of an energy drift. The dynamical and structural parameters were averaged ev-

Table 5.1: Simulated, ρ_{sim}, and experimental, ρ_{exp}, densities of PE (2800 g/mol) at 450 K and 1 bar.

T (K)	$\boldsymbol{\rho_{sim}}$ (g/cm^3)	$\boldsymbol{\rho_{exp}}$ (g/cm^3) [149]
415	0.786	0.778
430	0.779	0.770
450	0.766	0.760
470	0.755	0.750

ery 100 ps. All simulations described in this work were performed employing the LAMMPS simulation package (*version 19-May-2011*) [150].

5.3 BUILDING THE EMPIRICAL MESOSCOPIC FORCE FIELD

In the coarse-grained depiction, polymer chains are viewed as a sequence of beads connected by flexible springs, each representing an ensemble of *n*-consecutive monomers. Thus, the position of each bead, $\mathbf{R}_i^{CG}$, coincides with the position of the center of mass of the assemblage of atoms belonging to these *n*-consecutive monomers, λ:

$$\mathbf{R}_i^{CG} = \frac{1}{M}\sum_{\boldsymbol{i=1}}^{\boldsymbol{I\cdot\lambda}} m_i \mathbf{r}_i \tag{5.1}$$

where m_i and $\mathbf{r}_i$ are the mass and position of atom i in the atomistic system and M is the total mass of the coarse-grained particle. Here, λ is a symbolic representation of the coarse-grained level. The choice of its value is arbitrary: it should assure a balance between accuracy - to reproduce the details of the underlying system - and efficiency of time integration. Considering that beads are spherical and that their diameter depends on λ, if λ is too small beads may experience a strong influence of the excluded volume interactions with their neighbors. This could jeopardize the soft nature of the interactions required for a mesoscopic model, as discussed below. Additionally, if the purpose of the simulations is to cover long time dynamics, a small λ will not require a substantial increase of the time step. Lastly, a too low λ level may deter the use of a coarse-grained model from the computational time point of view. Conversely, an excessively large λ may risk the subsistence of some relevant details, which consequently affects the mapping resolution. A suitable value of λ should not yield a bead dimension greater than the tube diameter described by the reptation theory for undiluted systems, nor greater than the length of a local subchain that influences the dynamics of the system, in the case of diluted systems.

The force field governing coarse-grained systems at a fixed λ is obtained from atomistic simulations following the concept of potential of mean force,

$$U_\lambda\left(\mathbf{R}^N\right) = -k_B T \ln g_\lambda\left(\mathbf{R}_i\right). \tag{5.2}$$

where k_B and T are the Boltzmann's constant and temperature, respectively, and g_λ represents the distribution function described by the coarse-grained coordinates. For simplicity, g_λ is split into four independent components, a non-bonded contribution, defined by the pair correlation function, and three intramolecular contributions, described by bonded, angular and dihedral distribution functions. Thus, it is assumed that each contribution of the potential energy is pairwise additive and is obtained from the Boltzmann inversion of the separate distribution functions, according to

$$\begin{aligned} U_\lambda\left(\mathbf{R}^N\right) = & \sum_{i<j}^{N} u_\lambda^{nb}\left(R_{ij}\right) + \\ & + \sum_{i=1}^{n_{chains}} \sum_{j=(i-1)\cdot n_b+1}^{i\cdot n_b-1} u_\lambda^{b}\left(R_{jj+1}\right) + \\ & + \sum_{\theta} u_\lambda^{\theta}\left(\theta\right) + \sum_{\phi} u_\lambda^{\phi}\left(\phi\right), \end{aligned} \tag{5.3}$$

where,

$$u_\lambda^{nb}\left(R_{ij}\right) = -k_B T \ln\left(\frac{P_\lambda^{nb}\left(r\right)}{4\pi r^2}\right), \tag{5.4}$$

$$u_\lambda^{b}\left(R_{jj+1}\right) = -k_B T \ln\left(\frac{P_\lambda^{b}\left(r\right)}{4\pi r^2}\right), \tag{5.5}$$

$$u_\lambda^{\theta}\left(\theta\right) = -k_B T \ln\left(\frac{P_\lambda^{\theta}\left(\theta\right)}{\sin\theta}\right), \tag{5.6}$$

$$u_\lambda^{\phi}\left(\phi\right) = -k_B T \ln\left(P_\lambda^{\phi}\left(\phi\right)\right). \tag{5.7}$$

In these equations, P_λ refers to the distribution functions of each contribution without normalization. Since each contribution is handled separately, possible correlations between them are ignored.

Here, the potential of mean force was computed by averaging the distribution functions from the MD-NVE trajectories at 450 K and is shown in Fig. 5.1. Three levels of coarse-graining were considered (λ = 10, 12.5 and 20), corresponding to 10, 12.5 and 20 monomers per bead, respectively. To account for chain end effects, inner and outer groups of groups of n-monomers were discriminated and denoted as type-B and type-A, respectively. A total of nine interactions were then present: three non-bonded (A/A, B/B and A/B), two bonded (AB and BB), two angular (ABB and BBB), and two dihedral (ABBB and BBBB). For the sake of clarity, interactions between dissimilar particles

were omitted in Fig. 5.1. The effective interaction potentials were further parameterized and fitted according to a set of fitting functions. For the non-bonded and bonded interactions, the fitting functions assumed by Guerrault et. al. [133] were used, the angular interaction is a cosine function suggested by Padding et. al. [2], and the dihedral potential was fitted to a harmonic function. All fitting functions are summarized below:

$$u_{\lambda}^{nb,fit}(R) = a_0 e^{-(R/a_1)^2} + a_2 e^{-(R/a_3)^2}, \tag{5.8}$$

$$u_{\lambda}^{b,fit}(R) = b_0 e^{-(R/b_1)^2} + b_2 e^{-(R/b_3)^2} + b_4 R^{b_5}, \tag{5.9}$$

$$u_{\lambda}^{\theta,fit}(\theta) = c_0 (1 + \cos\theta)^{c_1}, \tag{5.10}$$

$$u_{\lambda}^{\phi,fit}(\phi) = d_0 (1 - d_1 \cos\phi)^{d_2}. \tag{5.11}$$

If λ is too high, the statistical noise becomes pronounced due to excessive particle overlapping. These fluctuations seem more severe in the very short range of the non-bonded and bonded distributions (see figures Fig. 5.1-a and Fig. 5.1-b) and along the whole distribution of the angular and dihedral interactions. This explains why it was not possible to account for dihedral potentials for $\lambda = 12.5$ and $\lambda = 20$. The above equations form the functional of the mesoscopic force field considered in the work. The fitted potentials can be found in Table 5.2.

5.4 MESOSCOPIC SIMULATIONS

5.4.1 *The DPD model*

DPD is a mesoscopic particle-based simulation technique commonly used in the simulation of soft-condensed matter [151]. Each particle of the system is a coarse representation of the averaged coordinates of sub-particles (e. g., atoms) belonging to a finer system. The interactions between mesoscopic particles are isotropic, soft-repelling and influenced by: a non-bonded conservative force, $\mathbf{F}^C$, a dissipative force, $\mathbf{F}^D$, and a stochastic force, $\mathbf{F}^S$. Their sum yields the following DPD Langevin equation:

$$\dot{\mathbf{p}}_i = \sum_{j \neq i} \mathbf{F}^C + \sum_{j \neq i} \mathbf{F}^D + \sum_{j \neq i} \mathbf{F}^S. \tag{5.12}$$

While the conservative force is directly related to the total potential energy (Hamiltonian) of the system (sum of non-bonded and bonded interactions), the combination of stochastic and dissipative forces reproduces the internal degrees of freedom within the particles. In classical DPD, these are represented by

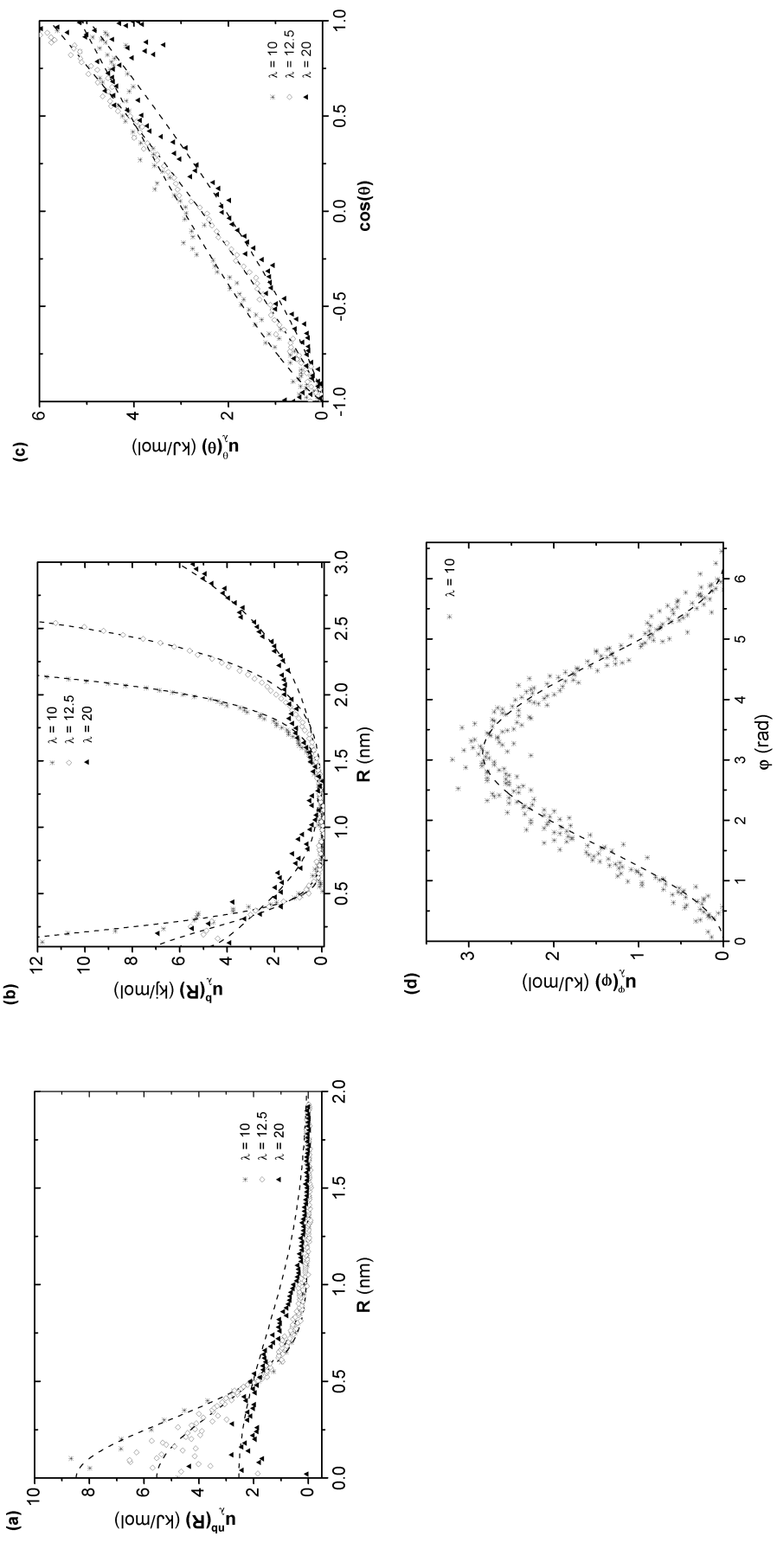

Figure 5.1: The contributions of the potential of mean force for λ =10, 12.5 and 20. Symbols represent the potentials determined from the atomistic distribution functions of λ-mer groups, and dashed lines are the fitted functions from Eqs.(5.8)-(5.11): (a) non-bonded potentials between B-type particles, (b) bonded potentials between B-type particles, (c) angular potentials of a triplet consisting on B-type particles, and, (d) dihedral potential of quadruplet consisting of B-type particles at $\lambda = 10$.

Table 5.2: Fitting parameters

$\lambda =$	**10**			**12.5**			**20**		
Non-bonded	B/B	A/A	A/B	B/B	A/A	A/B	B/B	A/A	A/B
a_0	8.24745	9.62008	3.40352	5.0974	0.08123	2.50569	1.23918	0.49884	1.05157
a_1	-0.414	-0.3505	-0.43501	0.48223	1.69605	0.51984	0.8387	1.10636	0.61181
a_2	0.22738	0.83634	3.40352	0.43286	5.72206	2.50569	1.23918	0.49884	1.42309
a_3	-0.80523	-0.9552	-0.43501	0.80748	0.40237	0.51984	0.8387	1.10636	0.8425
Bonded	BB	AB		BB	AB		BB	AB	
b_0	0.1678	1.00429		3.83848	2.06039		1.09434	1.72647	
b_1	-0.59088	0.32396		-0.33952	-0.37335		-0.14913	-0.56076	
b_2	26.2699	16.42728		3.83848	2.06039		1.09434	1.72647	
b_3	-0.22923	0.28143		-0.33951	-0.37335		-0.14913	-0.56076	
b_4	0.00376	0.00319		0.00379	0.00703		0.03751	0.03285	
b_5	10.61902	10.7977		8.60515	7.94174		4.75491	4.74844	
Angular	BBB	ABB		BBB	ABB		BBB	ABB	
c_0	3.01903	1.95901		2.57399	2.14049		2.0547	1.8776	
c_1	0.77229	1.52854		1.16889	1.3697		1.27012	1.33042	
Dihedral	BBBB	ABBB		BBBB	ABBB		BBBB	ABBB	
d_0	1.41666	1.70434		–	–		–	–	
d_1	1.0	1.0		–	–		–	–	
d_2	1.0	1.0		–	–		–	–	

$$\mathbf{F}_{ij}^{C} = a_{ij}\left(1 - r_{ij}/r_c\right)\mathbf{e}_{ij}, \tag{5.13}$$

$$\mathbf{F}_{ij}^{S} = \sigma\omega_S\left(R_{ij}\right)\zeta_{ij}\mathbf{e}_{ij}, \tag{5.14}$$

$$\mathbf{F}_{ij}^{D} = -\gamma\omega_D\left(R_{ij}\right)\left(\mathbf{e}_{ij}\cdot\mathbf{v}_{ij}\right)\mathbf{e}_{ij}; \tag{5.15}$$

where a_{ij} is the repulsive force parameter, r_c the range of interaction, $\mathbf{e}_{ij}$ is the unit vector pointing from j to i, $\mathbf{v}_{ij}$ is the relative velocity between particles i and j, ζ_{ij} is a symmetric Gaussian white-noise term with zero mean and unit variance, σ is the amplitude of the stochastic fluctuations, and γ is the friction coefficient. The interaction landscape of the stochastic and dissipative forces is defined by the weighting functions ω_S and ω_D, respectively. Eq.(5.12) *per se* does not provide a correct equilibrium distribution of the canonical ensemble, unless the stochastic and dissipative terms follow the fluctuation-dissipation theorem. Español and Warren [152] solved the time evolution of the distribution over the state space in the DPD equations in terms of the Fokker-Planck equation and found that the equilibrium distribution holds if

$$\begin{cases} \left[\omega_S\left(R_{ij}\right)\right]^2 = \omega_D\left(R_{ij}\right) = \omega\left(R_{ij}\right); \\ \sigma^2 = 2\gamma k_B T. \end{cases} \tag{5.16}$$

where $\omega\left(R_{ij}\right)$ is a quadratic function that fades beyond an arbitrary cutoff radius, R_c,

$$\omega\left(R_{ij}\right) = \begin{cases} \left(1 - R_{ij}/R_c\right)^2 & \text{if } R_{ij} < R_c \\ 0 & \text{else.} \end{cases} \tag{5.17}$$

The involvement of the dissipative and stochastic forces constitutes the DPD thermostat that is in charge of keeping the system under thermal equilibrium during the simulation.

5.4.2 *Scaling Parameters*

DPD simulations are usually performed in reduced units. The base units of length, $\hat{\sigma}$, energy, $\hat{\epsilon}$, and mass, $\hat{\mu}$, were chosen such that $\hat{\sigma} = \left(m_{bead}\rho^*/\rho_{MD}\right)^{1/3}$, $\hat{\epsilon} = k_B T/T^*$ and $\hat{\mu} = m/m^*$. The parameters with superscript asterisks indicate reduced values. To scale the length units, the mesoscopic density was set as identical to the atomistic density at 450K. The reduced temperature was chosen as 1 and the units of mass refers to the total mass of the coarse-grained particle. The scaling convention is summarized in Table 5.3.

Apart from driving the system to thermal equilibrium, the magnitude of the stochastic and dissipative forces inexorably influence the particle inter-diffusion. With the aim of predicting the real system dynamics in DPD simulations, Eriksson et. al. [153–155] suggested a bootstrapping algorithm to estimate $\omega\left(r\right)$ by means of the autocorrelation of the force fluctuations. In this

Table 5.3: Scaling convention of the physical magnitudes for each of the coarse-graining levels dealt in this work. $\hat{\sigma}$, $\hat{\epsilon}$ and $\hat{\mu}$, represent the base units of length, energy and mass, respectively.

	$\lambda = 10$	$\lambda = 12.5$	$\lambda = 20$
$\hat{\sigma}$ (nm)	0.775	0.835	0.976
$\hat{\epsilon}$ (kJ/mol)	3.738	3.738	3.738
$\hat{\mu}$ (g/mol)	280.54	350.68	561.09

formulation, the amplitudes of noise and friction are implicit in the weight functions. Another possibility is to adjust the dissipative and stochastic forces until the shape of the velocity autocorrelation function curve matches that resulting from atomistic simulations [156]. Karniadakis et. al. [157], calculated the friction force coefficients directly from atomistic simulations through the time-correlation function of the difference between the pairwise instantaneous force between clusters of atoms and the clusters average pair force. Furthermore, since the pairwise force between two clusters is generally not parallel to the line linking their center of masses, these authors decided to represent friction with radial and perpendicular components that are thermostated independently. In their mesoscopic simulations of polymers, Kindt and Briels [137] introduced the concept of scaling of the friction coefficient. It was found that time-dependent properties coincide if a scaling of the time axes is performed. Therefore, combining this procedure with a suitable time-mapping [158], the essential dynamics can be extrapolated to longer times by means of mesoscopic simulations.

The friction coefficient plays an important part when studying the evolution of a dynamical property in a certain time window. By setting the atomistic time scale as reference, for a time-dependent property ξ, the time shift δ is

$$\delta = \frac{t_{\xi_{MD}}}{t_{\xi_{\gamma}}}. \tag{5.18}$$

This equation provides the time-mapping required to calibrate the reduced mesoscopic time in relation to the real time dictated by the atomistic simulation. Even if this scaling appears to be rather simple, it has been validated on several polymeric systems [135, 158].

5.4.3 *Simulation parameters*

Table 5.4 identifies all the mesoscopic systems simulated in this work. Three distinct initial configurations were generated for each system and equilibrated during $2 \cdot 10^5$ timesteps (sufficient to equilibrate the system to $k_B T = 1.0$). After equilibration, data production runs lasting $2 \cdot 10^7$ steps were performed and trajectories were sampled every 10^4 timesteps. The cutoff radius was set according to the level of coarse-graining and the corresponding interaction

limit of the non-bonded potential. The timestep was set to 0.001 in all cases. With the purpose of assessing different time frames that can be tuned by the magnitude of the dissipative friction coefficient, each system in 5.4 was simulated with γ ranging between 10 and 350.

Table 5.4: Simulated systems (nomenclature: CG-X/Y, with X standing for λ level and Y standing for number of particles per chain), chain molecular weight M_w (g/mol), number of chains n_{chain} and side length of the cubic simulation cell L^* (reduced units).

System	N	M_w	n_{chain}	L^*
CG-10/5	5	1400	340	13.04
CG-10/10	10	2800	175	13.04
CG-10/20	20	5600	85	13.17
CG-10/50	50	14000	34	13.17
CG-10/100	100	28000	34	16.4
CG-12.5/5	5	1750	340	13
CG-12.5/8	8	2800	220	13.2
CG-12.5/20	20	7000	85	13.04
CG-12.5/50	50	17500	34	13
CG-12.5/100	100	35000	34	16.4
CG-20/5	5	2800	350	13.2
CG-20/10	10	5600	175	13.2
CG-20/20	20	11200	85	13.04
CG-20/50	50	28000	34	13
CG-20/100	100	280000	34	16.4

5.5 RESULTS AND DISCUSSION

5.5.1 *Distribution functions*

In order to evaluate the accuracy of the adopted force field (Section 5.3), it is necessary to compare the distribution functions given by DPD simulations with the corresponding atomistic distributions used in Eqs. (5.4)-(5.7). For each λ level, this comparison was made between chains with the same molecular weight. Fig. 5.2 to Fig. 5.4 compare the results obtained for CG-10/10, CG-12.5/8 and CG-20/5 with the corresponding atomistic results. In each case, a low and a high DPD friction coefficient were used, in order to ascertain whether this parameter influences the local chains structure, since apart from being a dynamic parameter, it also influences the strength of $\omega_D(R)$. The fact that $g_\lambda^{nb}(0) > 0$ in both the atomistic and mesoscopic simulations reflects the soft nature of the interactions.

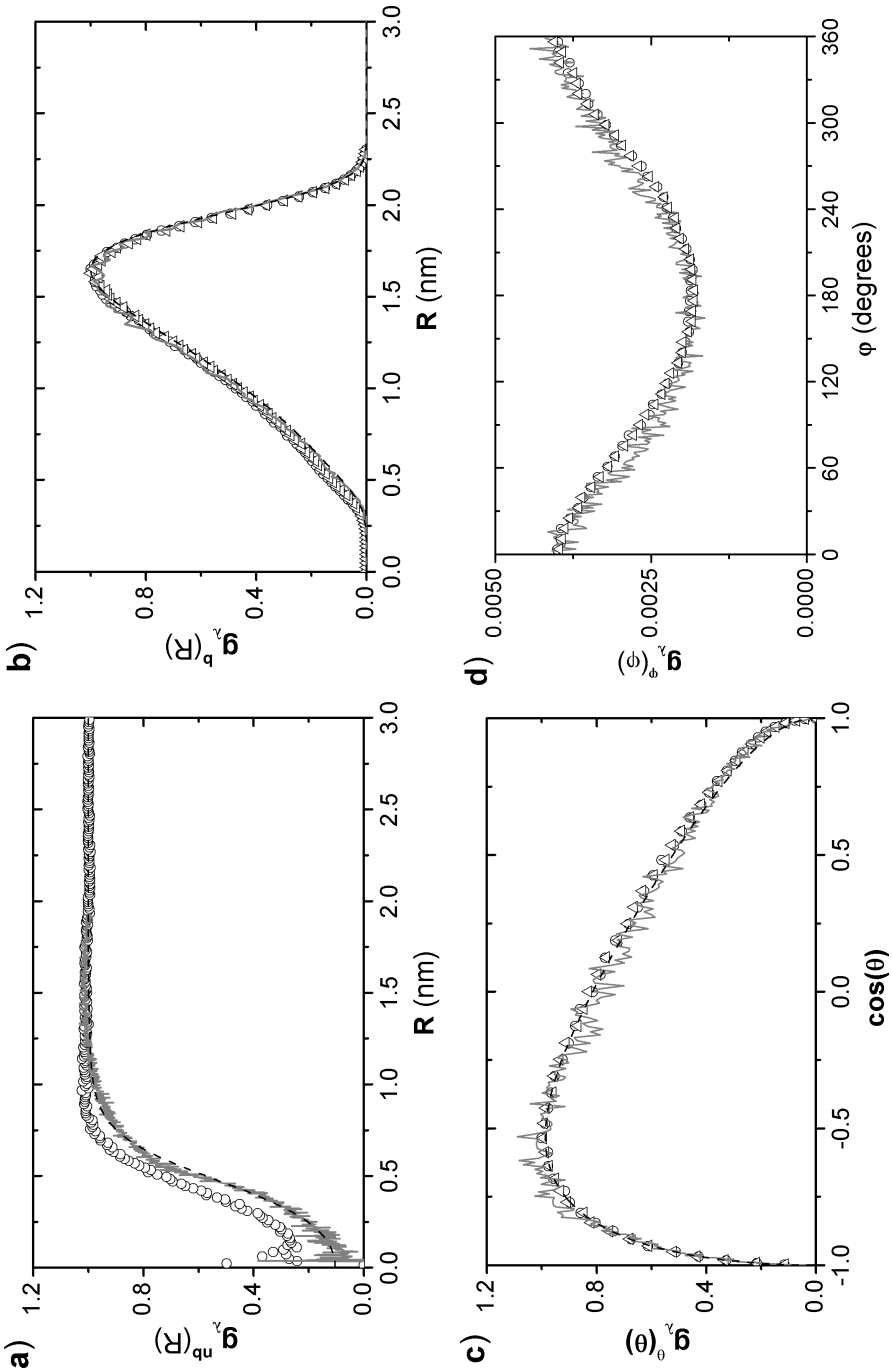

Figure 5.2: Distribution functions of CG-10/10 and 10-mer groups from atomistic simulations; a) non-bonded, b) bonded, c) angular, and, d) dihedral distribution functions (see also Table 5.4 for system identification). Symbols △ and ◯ represent DPD simulations using γ 10 and 350, respectively. Solid lines refer to atomistic simulations, dashed lines to the inverted fitting functions $g_\lambda^{fit} = \exp^{-u_\lambda/k_BT}$.

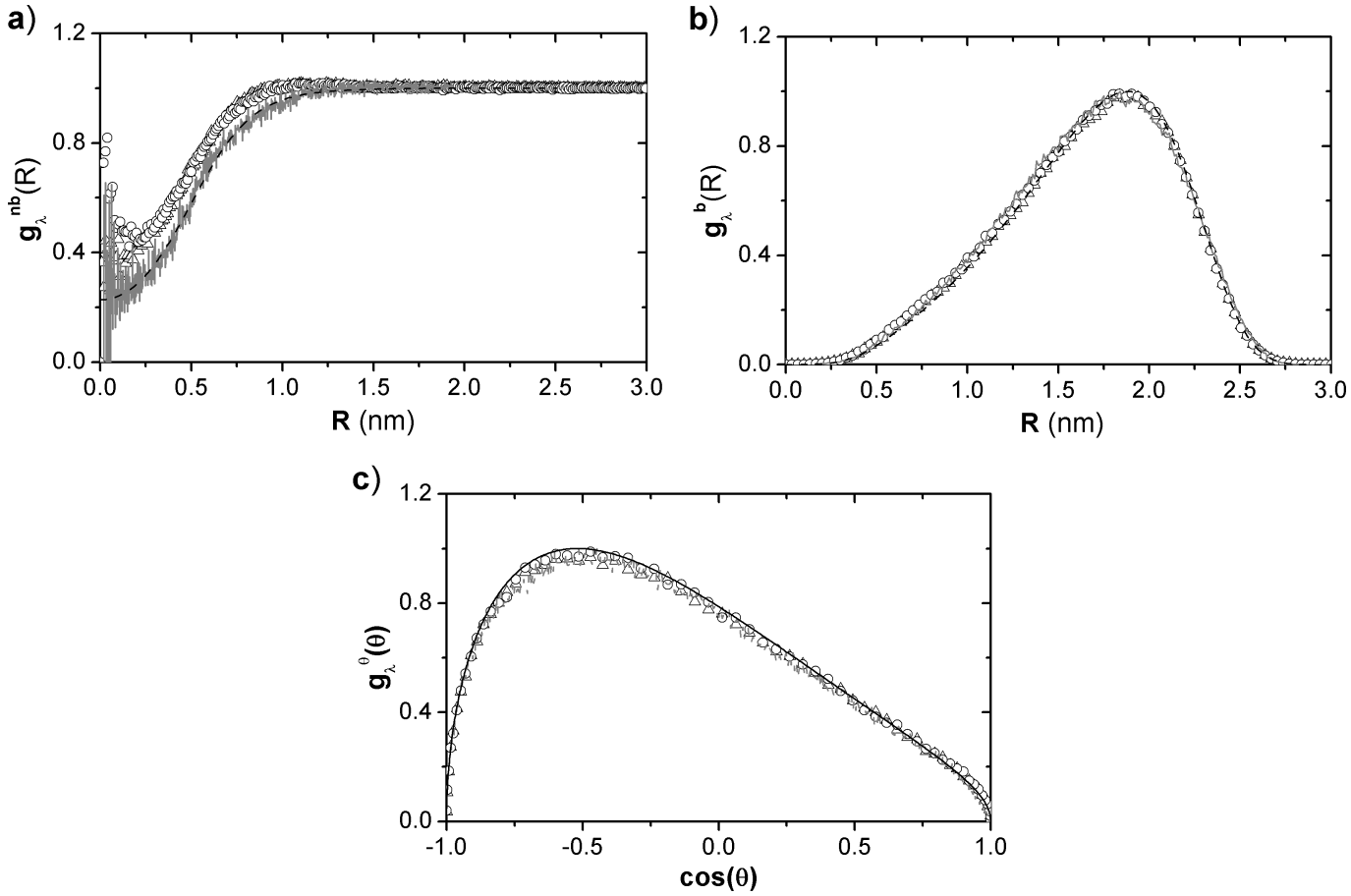

Figure 5.3: Distribution functions of CG-12.5/8 and 12.5-mer groups from atomistic simulations; a) non-bonded, b) bonded, c) angular distribution functions (see also Table 5.4 for system identification). Symbols △ and ◯ represent DPD simulations using γ 10 and 350, respectively. Solid lines refer to atomistic simulations, dashed lines to the inverted fitting functions $g_\lambda^{fit} = \exp^{-u_\lambda / k_B T}$.

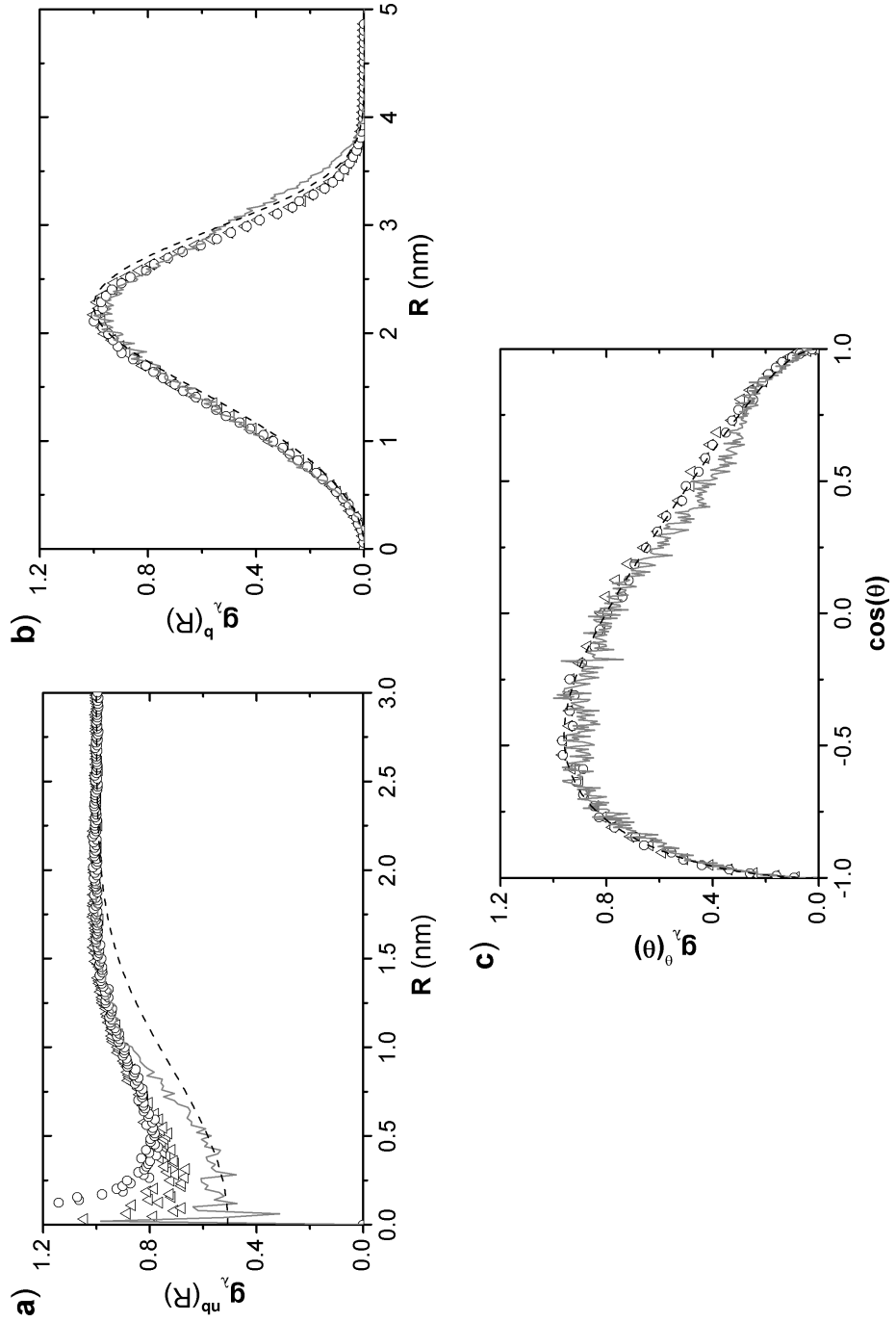

Figure 5.4: Distribution functions of CG-20/5 and 20-mer groups from atomistic simulations; a) non-bonded, b) bonded, c) angular distribution functions (see also Table 5.4 for system identification). Symbols △ and ◯ represent DPD simulations using γ 10 and 350, respectively. Solid lines refer to atomistic simulations, dashed lines to the inverted fitting functions $g_\lambda^{fit} = \exp^{-u_\lambda/k_BT}$.

At short radial distances the results deviate considerably from the atomistic simulations, the differences increasing with λ. This loss of resolution indicates that important packing effects are being ignored or underestimated, resulting in excessive bead overlapping due to weak repulsive interactions. The differences are also influenced by the choice of γ. This fact can be better understood after computing the existing excluded volume v between coarse-grained pairs of particles in the entire system, calculated from

$$v = -\int \left(g_{\lambda}^{nb} - 1\right) d^3r, \tag{5.19}$$

where the term in the integral is the so-called Mayer f-function [159]. For $\gamma = 10$ the excluded volumes are $v_{\lambda=10} = 0.336$, $v_{\lambda=12.5} = 0.307$ and $v_{\lambda=20} = 0.2132$, whereas for $\gamma = 350$ the values 0.32, 0.221 and 0.027 are obtained, respectively, i. e., the repulsive interactions weaken as λ increases. Setting a large γ enhances particle overlapping, this becoming more drastic at higher coarse-graining levels. The non-bonded radial distribution function in Fig. 5.4 also shows a deviation from the inverted potential of mean force curve in relation to the atomistic result. As the non-bonded potential of mean force was computed following a simple Boltzmann inversion without any further refinement, perhaps more subtle methodologies such as *Iterative Boltzmann Inversion*, IBI, [112] or *Inverse Monte Carlo*, IM [111], would be more effective. Although IBI and IM are commonly used for building united-atom force fields, Lahmar et. al. [134] obtained good results using IBI with coarse-grained particles representing ten polyethylene monomers. Conversely, all the intramolecular distribution curves compare very well, even at the highest λ.

5.5.2 *Chain dimensions*

The global dimensions of polymer chains are usually measured in terms of the mean-square radius of gyration, $\langle R_g^2 \rangle$, and mean-square end-to-end distance, $\langle R_{ee}^2 \rangle$. The scaling with molecular weight $\langle R_g^2 \rangle \sim M_w^{\mu}$ and the relation $6\langle R_g^2 \rangle / \langle R_{ee}^2 \rangle$ can provide an understanding of the statistics followed by the polymer chains. These quantities are plotted in Fig. 5.5. While the ratio $6\langle R_g^2 \rangle / \langle R_{ee}^2 \rangle$ approaches unity for $M_w \approx 5000$ g/mol, a relation $\langle R_g^2 \rangle \sim M_w^{1.0}$ exists. According to random walk statistics of the freely jointed chain, these results demonstrate chain ideality. Although similar trends are observed at all λ, it seems from Fig. 5.5-a that for shorter chains the differences are slightly more pronounced, as they are more sensitive to chain end effects. The positive contribution of the excluded volume to the conformation state of the chains can be neglected (chain ideality). Data in Fig. 5.5-b are in good agreement not only with those published for united-atom molecular dynamics simulations [1], but also with the results from other mesoscopic simulations [2] and experiments [3].

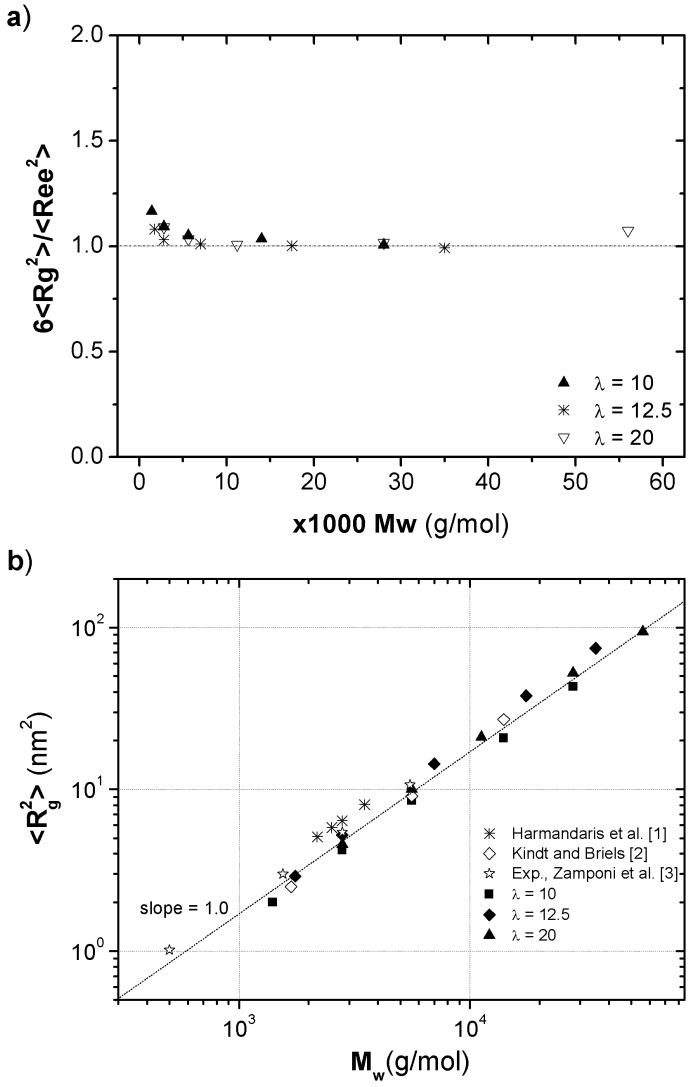

Figure 5.5: Influence of the molecular weight and coarse-graining level on chain structure. a) $6\langle R_g^2\rangle/\langle R_{ee}^2\rangle$ and b) $\langle R_g^2\rangle$ as a function of M_w. Results obtained from united-atom simulations [1], mesoscopic simulations [2] with particles representing 10 monomers, and experimental results [3] are also shown for comparison. In both plots the dashed line represents ideal chain predictions.

Table 5.5 compares different coarse-graining levels and the atomistic simulation. Even though the reproducibility of $\langle R_{ee}^2\rangle$ is only satisfactory, the statistics seem to be preserved.

As for the influence of the friction coefficient on the structural properties, Lahmar et. al. [138] argued that neither the shape of the radial distribution function nor the chain architecture are affected. The first argument is verified here, as seen in Fig. 5.2 through Fig. 5.4. Indeed, despite the fluctuations in the vicinity of $r = 0$, no substantial differences in the distribution functions were found. Nevertheless, M_w affects the way γ impacts on chain architecture (column bars in Fig. 5.6). Using the same λ as Lahmar et. al. [138], no discrepancy in the results is detected when M_w is small, but differences increase with M_w.

Table 5.5: Chain dimensions in terms of $\langle R_g^2 \rangle$ (nm^2) and $\langle R_{ee}^2 \rangle$ (nm^2) for atomistic and coarse-grained systems with the same chain molecular weight M_w (g/-mol). $6\langle R_g^2 \rangle / \langle R_{ee}^2 \rangle$ is the characteristic ratio.

System	M_w	$\langle R_g^2 \rangle$	$\langle R_{ee}^2 \rangle$	$6\langle R_g^2 \rangle / \langle R_{ee}^2 \rangle$
Atomistic	2800	5.10	28.81	1.06
CG10/10	2800	4.20	23.07	1.09
CG12.5/8	2800	5.22	30.38	1.03
CG20/5	2800	4.56	25.12	1.09

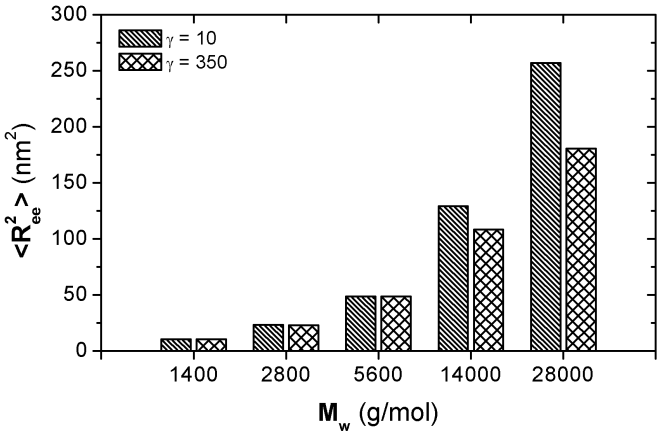

Figure 5.6: Effect of $\langle R_{ee}^2 \rangle$ on M_w for two γ values.

5.5.3 *Mean square displacement and time scaling*

As shown above, the mesoscopic force-field reproduces satisfactorily the chain dimensions computed by atomistic results and theory. The principle of time scaling was summarized in Section 5.4.2. The mean-square displacement of the center of mass of the chains, $\phi_{c.m.}$, and of the coarse-grained groups of monomers, ϕ_λ, estimated from the atomistic trajectories were determined as:

$$\phi_{c.m.}(t) = \left\langle \left[\mathbf{R}_{c.m.}(t) - \mathbf{R}_{c.m.}(0) \right]^2 \right\rangle \tag{5.20}$$

and

$$\phi_\lambda(t) = \frac{1}{N} \sum_{i=1}^{N} \left\langle \left[\mathbf{R}_{\lambda,i}(t) - \mathbf{R}_{\lambda,i}(0) \right]^2 \right\rangle, \tag{5.21}$$

The same calculations were performed considering the trajectories resulting from mesoscopic simulations.

The scaling rule of Eq.(5.18) can be used to extrapolate the long time dynamic behavior predicted by the mesoscopic simulations. As depicted in Fig. 5.7, the results superimpose well on a single master curve describing the entire shape of the mean-square displacement. The short and long time responses are covered by atomistic and mesoscopic simulations, respectively. At short times, the mesoscopic ϕ_λ diverges from the atomistic result, indicating that

the dynamics are less accessible. These differences become more pronounced with increasing λ. As will be discussed in the following section, this can be ascribed to the inability of DPD simulations to cover the fastest relaxations. At each λ level, the behaviour of $\delta(\gamma)$ can be estimated by fitting the results to a power-law,

$$\delta(\gamma) = b\gamma^{-\alpha} \tag{5.22}$$

Table 5.6 presents the corresponding coefficients.

Table 5.6: Time-mapping coefficients of a power-law for each λ.

λ	b	α
10	9652.76	-0.809
12.5	13884.88	-0.844
20	10290	-0.998

The dynamics of untangled polymer chains are usually expressed in terms of the Rouse [160] and Zimm [161] models. Both assume the motion of a Gaussian chain consisting of n beads connected to a heat bath and free of excluded volume effects. The two models differ in terms of their kinetics. While in the Rouse model the mobility of the beads is uniquely restrained by a constant background friction and the possibility of hydrodynamic interactions is disregarded, in the Zimm model the motion of a bead is affected by the motion of all neighboring beads, linear momentum is conserved and hydrodynamics is present. Consequently, the corresponding scaling laws are also different. For the mean-square displacement of monomers, the subdiffusive regime under the longest relaxation time, τ_1, predicted by the Rouse model scales as $\phi_1(t) \sim t^{1/2}$, whilst in the Zimm model it scales as $\phi_1(t) \sim t^{2/3}$. In this regime, the dynamics is dictated by a slowdown of diffusion, caused by the time spectrum of local conformational chain relaxations. Here, τ_s denotes the time at which the sub-diffusive regime sets in. For longer times ($t > \tau_1$), it is anticipated that the monomers evolve over a distance comparable to R_g, after which a purely diffusive regime sets in (Fickian diffusion). For both models, this regime scales as $\phi_1(t) \sim t^1$. The different time regimes are clearly noticeable in Fig. 5.7 as changes of the slopes of the $\phi_\lambda(t)$ curves. The intermediate slopes, characterizing the slowdown of diffusion, seem to increase with the magnitude of λ. In all cases an 8% deviation between the atomistic ($\phi_{\lambda=10} \sim t^{0.58}$, $\phi_{\lambda=12.5} \sim t^{0.60}$ and $\phi_{\lambda=20} \sim t^{0.65}$) and the mesoscopic results ($\phi_{\lambda=10} \sim t^{0.63}$, $\phi_{\lambda=12.5} \sim t^{0.65}$ and $\phi_{\lambda=20} \sim t^{0.70}$), was found.

The impact of λ on the chain dynamics can be readily identified if ϕ_λ is compared with the monomeric mean-square displacement (star symbols in Fig. 5.7), which scales Rouse-like ($\phi_{\lambda=1} \sim t^{0.5}$). The differences between curves are due to resolution inefficiencies caused by the stiffening of the chains with increasing λ and by a compressibility issue (further discussed in Section 5.5.6). The slopes pertaining to the atomistic system deviate from a typical Rouse

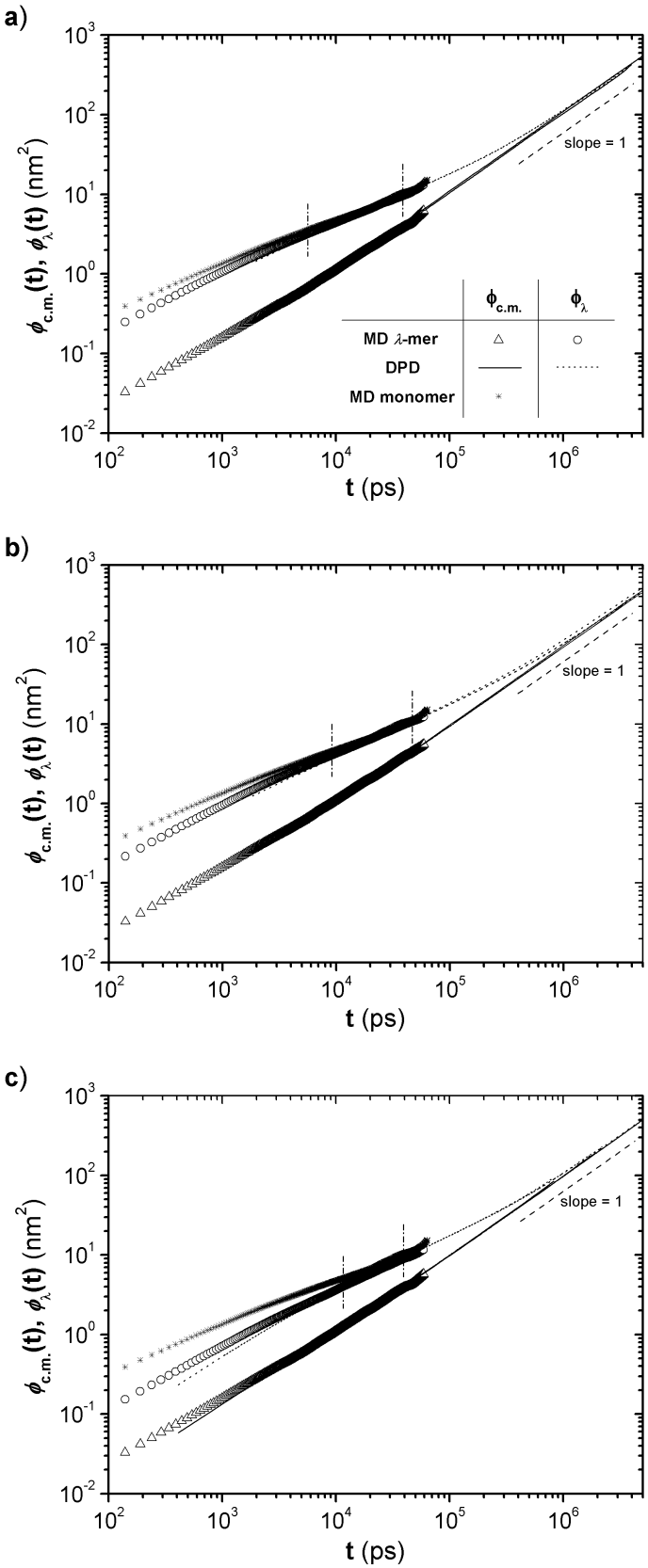

Figure 5.7: Mean-square displacements of the chain center of mass $\phi_{c.m.}$ and mesoscopic particles ϕ_λ after time-mapping: a) $\lambda = 10$, b) $\lambda = 12.5$, and c) $\lambda = 20$. Symbols represent the mean-square displacement of the corresponding λ-mer groups of atomistic monomers. Vertical dashed lines represent the boundaries of the region where the slopes were analyzed.

behaviour, as inferred by the monomeric mean-square displacement to higher values for larger λ-mer collections. Scaling of the mesoscopic system at the lowest coarse-graining level seems to follow Zimm's prediction. In the particular case of polyethylene, Guerrault et. al.[133] showed that the minimum accessible coarse-graining level suitable for DPD simulations is 8 monomers per DPD particle. Lower values compromise the softness of the interactions. Even if the minimum λ level taken in this work is 10, the dynamics for a $\lambda = 8$ system will probably be rather similar. Apart from the increase in slope, the intermediate regime narrows, meaning that the local conformational details and the faster dynamics become gradually absorbed as the system coarsens. If λ would be further increased, ultimately $\tau_s \approx \tau_1$ and ϕ_λ would lay over $\phi_{c.m.}$.

5.5.4 *Sub-diffusive relaxation analysis*

This section investigates the relaxation dynamics of the system in terms of Rouse modes. These are defined as

$$\mathbf{X}_k(t) = \frac{1}{N}\sum_{i=1}^{N}\mathbf{R}_i(t)\cos\left[\frac{k\pi}{N}\left(i-\frac{1}{2}\right)\right] \qquad k = 1, \ldots, N-1 \tag{5.23}$$

where N is the number of particles in the chain, k is the mode number and $\mathbf{R}_i$ is the position of particle i. The *zeroth* mode, $k = 0$, is related to the translational motion of the chains center of mass. The internal motions represented by the N/k segments within the chain are connected with the remaining modes ($k > 0$). As k increases, the sensitivity to local details increases. According to the Rouse theory, the relaxation of each mode is expressed by an exponential decay resulting from the normalized mode auto-correlation function,

$$C_k(t) = \langle \mathbf{X}_k(t) \cdot \mathbf{X}_k(0) \rangle \,/\, \langle \mathbf{X}_k^2 \rangle = \exp(-t/\tau_k), \tag{5.24}$$

where τ_k is the relaxation time corresponding to mode k. This equation also applies to the Zimm model. If the longest relaxation time is to be calculated, the equation above remains as the auto-correlation function of the end-to-end vector. However, the addition of intermolecular constraints into the equations of motion compromises the exponentiality of Eq. (5.24). It turns out that in order to account for the deviations of the Rouse theory, the local dynamics are better described by the following stretched exponential form [2, 162–164]:

$$C_k(t) = \exp\left[-(t/\tau_k^*)^{\beta_k}\right], \tag{5.25}$$

where the relaxation time τ_k^* and the stretching parameter β_k depends on mode number k and chain length. If $\beta_k = 1$, k slows down as predicted by the Rouse model, otherwise it deviates from a purely exponential relaxation.

It is important to investigate to which extent the mesoscopic simulations at different λ levels replicate the underlying mode relaxations. Fig. 5.8 plots the stretching parameters of atomistic and mesoscopic systems as a function of wavelength. For the sake of coherence between λ levels and the molecular weight represented by the sub-segments, wavelengths were expressed in terms of M_w/k. In all cases, the sub-chains exhibit β_k values lower than unity. The non-exponential character of the relaxation modes may be interpreted in terms of hierarchical kinetic constraints [162]. These arise from local hindrances to segment motion, as a result of the cooperativity between non-bonded interactions between neighbour particles and chain stiffness created by intra-molecular potentials. The kinetic constraints become stronger at smaller M_w/k, with $\beta_k \approx 0.8$ at the lower wavelength limit. The result is similar to that reported by Shaffer [162] for short chains free of entanglement constraints. The mesoscopic data evidences an absence of β_k values for the smaller scale modes (open symbols in Fig. 5.8). Such fast relaxations are not handled by the DPD simulations performed here, unless γ values higher than 350 are assumed and complemented by a reduction of the time-step (see Fig. 5.7). The soft nature of the non-bonded interactions used in the mesoscopic simulations facilitates particle mobility, which explains the existence of a slight discrepancy between the non-exponential strength of the two models. It is also possible that entanglement constraints present in the atomistic system might slow down diffusion.

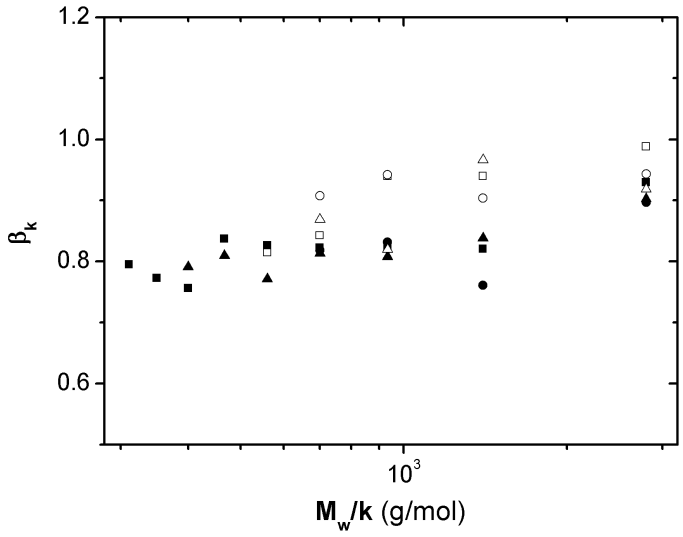

Figure 5.8: Stretching parameters obtained from CG-10/10 (□), CG-12.5/8 (△), CG-20/5 (◯) and corresponding *10*-mer (■), *12.5*-mer (▲) and *20*-mer (●) groups obtained from the MD simulation.

The fitted relaxation time, τ_k^*, in Eq.(5.25) is strongly influenced by the deviations of the relaxation function. Thus, the average mode relaxation times are computed instead, since they take into account the entire shape of the normalized mode relaxation function. Using the fitted parameters, they are obtained from

$$\langle \tau_k \rangle = \int_0^\infty \exp\left[-\left(t/\tau_k^*\right)^{\beta_k} \right] dt = \frac{\tau_k^*}{\beta_k} \Gamma\left(\frac{1}{\beta_k}\right), \tag{5.26}$$

where Γ is a gamma function. The corresponding effective relaxation rates of the modes, as defined by the Rouse theory are

$$W_k^{eff} = \left[4 \langle \tau_k \rangle \sin^2\left(\frac{k\pi}{2N}\right) \right]^{-1}. \tag{5.27}$$

Eq. (5.22) is again used to convert the mesoscopic time into the physical time dictated by the atomistic simulations. Fig. 5.9 compares $\langle \tau_k \rangle$ and W_k^{eff} for different length scales and λ levels. The dashed and dotted lines in Fig. 5.9-a represent the slopes predicted by the Rouse and Zimm theories, respectively. The good correspondence between $\langle \tau_k \rangle$ values of the mesoscopic and atomistic simulations suggests that time mapping with the coefficients given in **??** prevails for dynamical properties other than $\phi(t)$. Nonetheless, small differences exist. The exponent x of the $\langle \tau_k \rangle \sim (M_w/k)^x$ scaling rule related to the coarse-grained representations of the atomistic system is 1.87, 1.89 and 1.95 for λ equal to 10, 12.5 and 20, respectively, while DPD simulations yield 1.74, 1.75, 1.81, respectively. This represents a deviation of approximately 7%, which is close to that reported above for the sub-diffusive regimes of ϕ_λ. The relaxation shown by the largest length scale ($k = 1$) refers to the longest relaxation time, τ_1, and represents the complete rotation of the entire chain. Within this time scale the differences are negligible, λ having virtually no effect over the long time relaxation. Fig. 5.9-b represents W_k^{eff} against M_w/k and provides a good perception of the effect of λ on the mode relaxation. The atomistic results show that the relaxations at the smaller length scales take longer times, whereas at higher length scales they seem to reach a constant value. According to the Rouse theory, W_k^{eff} should be constant along the whole range of relaxations. Thus, its increase at low M_w/k means that chains are stiffer at short scales and the effect is aggravated as λ increases. These predictions also hold for the mesoscopic systems. This response unveils one of the motives why sub-diffusive regimes scale differently depending on the coarse-graining level. When dealing with coarse-grained representations, either consisting of mesoscopic particles or of λ-mer atomistic blobs, it is assumed that the atoms form stiff sections of the fully atomistic chain. The results obtained here indicate that, as the number of monomers inside the coarse-grained representation increases, the effect of chain stiffness is sensed at bigger wavelengths. This demonstrates how the magnitude of the coarse-graining level affects the resolution of the system.

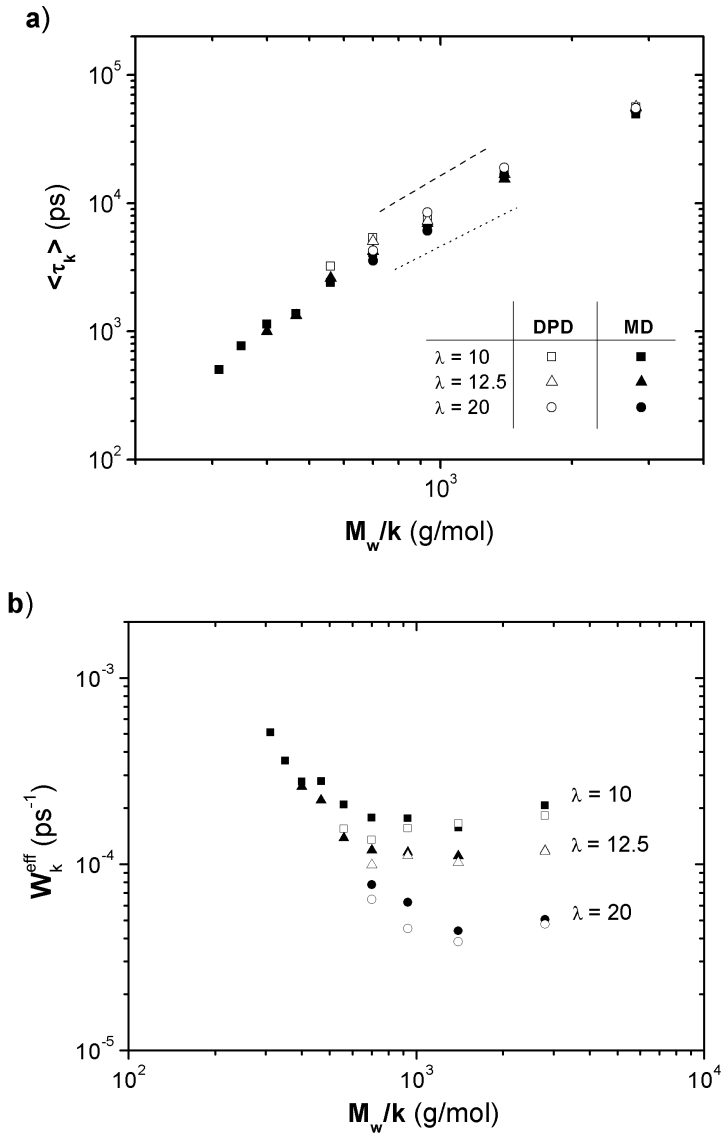

Figure 5.9: Sub-diffusive analysis in terms of a) $\langle\tau_k\rangle$ and b) W_k^{eff}. Dashed and dotted lines in a) represent the trends of Zimm and Rouse models, respectively.

5.5.5 *Segmental relaxation*

The time dependence of the bond displacements is too fast to be coped with mesoscopic simulations. Therefore, the segmental relaxation time, τ_s was estimated from the atomistic trajectories by means of the coherent dynamic structure factor for a single chain, defined as

$$S'(q,t) = \frac{1}{N}\sum_{i,j}\left\langle \exp\left\{ i\mathbf{q}\cdot\left[\mathbf{r}_i(t) - \mathbf{r}_j(0)\right]\right\}\right\rangle, \tag{5.28}$$

In this equation, $\mathbf{q}$ is the scattering vector and i and j denote atoms belonging to the same chain. Since an isotropic bulk system is being studied, Eq. (5.28) can be reduced to [115]

$$S'(q,t) = \sum_{i,j} \left\langle \sin\left[|\mathbf{q}||\mathbf{R}_{ij}(t)|\right] / |\mathbf{q}||\mathbf{R}_{ij}(0)| \right\rangle , \tag{5.29}$$

with $|\mathbf{R}_{ij}|$ denoting the magnitude of $\mathbf{r}_i(t) - \mathbf{r}_j(0)$ and $|\mathbf{q}|$ referring to the magnitude of the scattering vector. Since a coarse-grained framework is assumed, $\mathbf{R}(t)$ represents the center of mass of n consecutive monomers with respect to the λ levels assigned. Knowing the maximum bond length, b_{max}, the corresponding wavelengths of the scattering vector ($|\mathbf{q}|/2\pi = 1/b_{max}$) can be directly assessed for each λ and dynamic structure factor. From the bond distribution functions displayed in Fig. 5.2 to Fig. 5.4, the maximum bond length is found as 2.15, 2.5 and 3.5 nm, for λ equal 10, 12.5 and 20, respectively. Hence, the corresponding magnitude of the wavelength vectors is $|\mathbf{q}|_{\lambda=10} = 2.9\ \text{nm}^{-1}$, $|\mathbf{q}|_{\lambda=12.5} = 2.5\ \text{nm}^{-1}$ and $|\mathbf{q}|_{\lambda=20} = 1.8\ \text{nm}^{-1}$. The time instant when the normalized dynamic structure factor depicted in Fig. 5.10 reaches the value $1/e$ is τ_s. The arrows in the figure indicate the segmental times for each λ level.

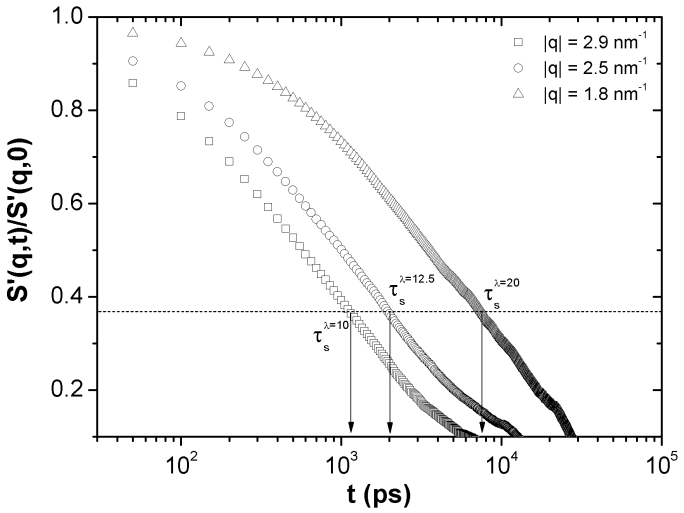

Figure 5.10: Single-chain normalized dynamic structure factor of the atomistic system. The $|\mathbf{q}|$ values shown refer to b_{max} of each coarse-grained representation. The horizontal dashed line indicates $S(t,q)/S(0,q) = 1/e$, and the arrows point to τ_s.

5.5.6 *Molecular weight dependence*

The dynamic properties of the systems having the same molecular weight were discussed in Section 5.5.3. It was concluded that near to the lower coarse-graining limit ($\lambda \approx 10$), the mean-square displacement of particles scales as $\phi_\lambda(t) \sim t^{0.63}$ along intermediate time scales ($\tau_s < t < \tau_1$).

It is also important to study the influence of chain length on the mean-square displacement of particles. Fig. 5.11 clearly shows that, as the molecular

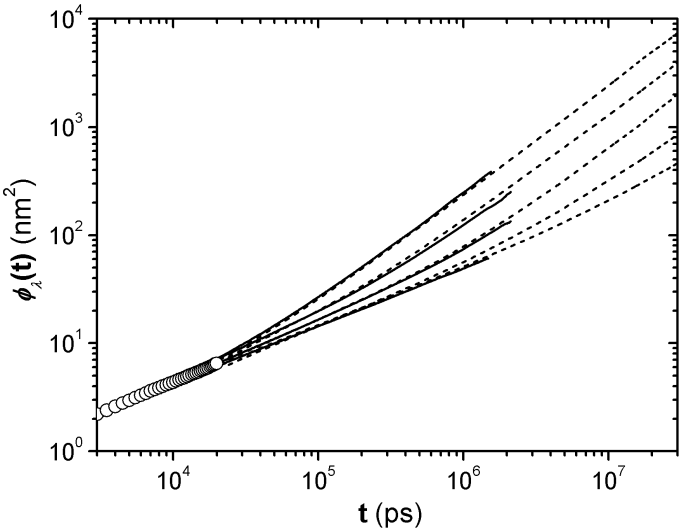

Figure 5.11: Particle mean-square displacement $\phi_\lambda(t)$ vs t, for systems with λ=10. Data from top to bottom corresponds to CG-10/5, CG-10/10, CG-10/20, CG-10/50 and CG-10/100. Continuous and dashed lines are simulations corresponding to γ equal 350 and 10, respectively. Open symbols is the 10-mer $\phi_\lambda(t)$ obtained from the MD simulation.

weight increases (i. e., by increasing N), diverse sub-diffusive behaviours arise - from $g_\lambda(t) \sim t^{0.66}$ for CG-10/5, to $g_\lambda(t) \sim t^{0.5}$ for CG-10/50 and CG-10/100. This scaling is similar to those presented by diluted (Zimm-like) and semidiluted (Rouse-like) solutions. It is accepted that the Zimm model adequately describes the dynamics of dilute polymer solutions, i. e., when chains are hydrodynamically coupled to a solvent and separated from each other (coiled chains with ideal conformation). A semidiluted regime is reached when the concentration of molecules reaches a critical overlap concentration, c^*. Beyond this threshold, the chains start to interpenetrate and the hydrodynamic interactions are screened by surrounding chains [115, 165]. The system begins to react in the same way as a viscous untangled polymer melt, with its dynamics described by the Rouse model. The characteristic length scale separating the two types of dynamics is denoted as hydrodynamic screening length, ξ_h. At length scales shorter than ξ_h chains are considered as diluted, while above ξ_h the characteristic length of chains overlap and screening of hydrodynamic interactions and excluded volume takes place.

In the presence of θ-solvents, the chain statistics are nearly ideal at all length scales and concentrations, no changes occurring in polymer conformation. The systems considered here have identical particle concentration. However, it is known that, on the limit of c^*, the hydrodynamic interactions apply over length scales comparable to the size of the entire chain ($c^* = 3M_w/4\pi n_A R_g^3$) and their magnitude decreases with molecular weight. Therefore, systems with different c/c^* ratio will experience dissimilar dynamics. Each chain is assumed as a sphere with a diameter equal to ξ_h, which is approximately R_{ee} [166], and volume V_{ξ_h}. For each system, the corresponding

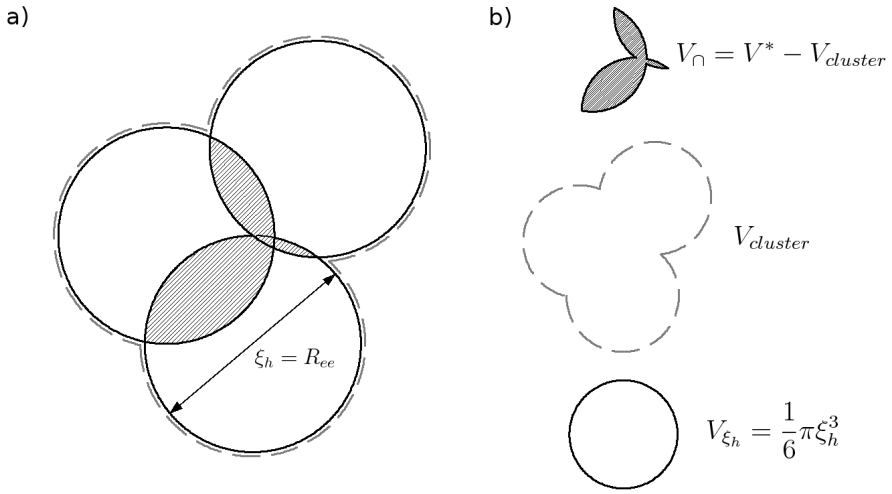

Figure 5.12: 2D example showing the intersection of three correlation lengths ξ_h (a), where the circles formed by continuous lines represent the correlation volumes V_{ξ_h} delimiting a polymer chain, the dashed area represents the intersecting volume $V_\cap$, and the dashed line around the cluster of correlations volumes is $V_{cluster}$ (see part b of figure).

c/c^* ratio and the intersecting volume fraction $V_\cap/V^*$ (which relates the pervading volume among chains above c^* with the critical volume V^*) are presented in Table 5.7. The pervaded volume existing between V_{ξ_h}, is given by

$$V_\cap = \frac{1}{6}N_c\pi R_{ee}^3 - V_{cluster}, \tag{5.30}$$

where N_c is the number of chains and $V_{cluster}$ is the volume of a cluster formed by overlapped spheres. The first term on the right hand side of the equation represents V^*, which is the total volume of spheres considering that chains are completely diluted. The ARVO package [167, 168] was used to calculate $V_{cluster}$. Fig. 5.12 illustrates the 2D the calculation of those quantities, including $V_\cap$ due to the overlapping of three spheres. The data in Table 5.7 for c/c^* preclude the possibility of the systems appearing on a diluted state. Nonetheless, the values of $V_\cap/V^*$ generally support the results of Fig. 5.11, where the dynamics are slown down as the overlapping between correlation lengths increases. Thus, it appears that the inconsistencies between c/c^* and the slopes of the sub-diffusive regimes, occur because the model fails to reproduce the correct system compressibility. The fact that the slopes of CG-10/50 and CG-10/100 systems and the respective $V_\cap/V^*$ are close to 1 suggests that the hydrodynamic interactions are fully screened. The differences appear only to the length of the sub-diffusive regimes. A progressive raise of M_w will merely result in a broadening of the sub-diffusive regime in the direction of higher values of τ_1, with the slope remaining unchanged. Reptation motion plays an important part in such concentrated systems, but clearly this is not handled by the simulations performed here. The absence of segmental repulsion potentials to avoid topological violations makes certain simulations somewhat unrealis-

tic. In this respect, important contributions have been made within the scope of segmental repulsion potentials for mesoscopic models [132, 169–172].

Table 5.7: Concentration fraction (c/c^*) and intersecting volume fraction ($V_\cap/V^*$) for systems with different molecular weight.

System	M_w	c/c^*	$V_\cap/V^*$
CG-10/5	1400	3.82	0.79
CG-10/10	2800	6.08	0.87
CG-10/20	5600	8.00	0.89
CG-10/50	14000	12.64	0.98
CG-10/100	28000	17.94	1.00

The above discussion pertain to systems having 10 monomers per mesoscopic particle. Identical trends were observed for systems with 12.5 and 20 monomers. After reaching a certain M_w and $V_\cap/V^* \approx 1$, the dynamics of the sub-diffusive regime follows the same evolution, with $\lambda = 12.5$ and $\lambda = 20$ reaching a slope of 0.56 and 0.64, respectively. As depicted in Fig. 5.13, when comparing the long time relaxations, it is surprising to observe that the coarse-graining level does not affect the scaling of τ_1 with M_w. At $M_w \approx 9000$, the slope changes, following closely a transition from Zimm to Rouse predictions.

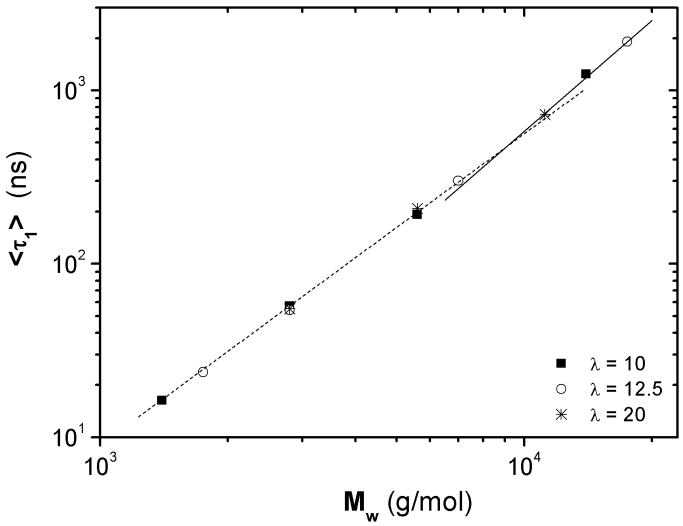

Figure 5.13: Comparison between the estimated relaxation times τ_1 given by different coarse-graining levels. The dashed and continuous lines are guides to the eye representing the Zimm and Rouse scaling, respectively.

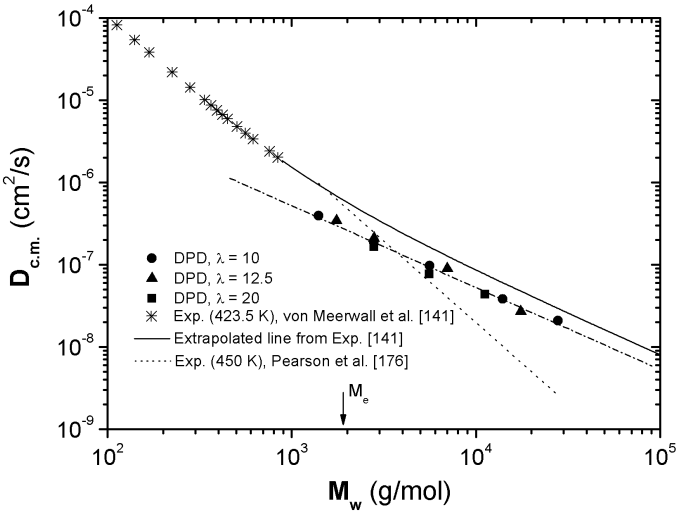

Figure 5.14: Comparison between calculated self-diffusion coefficients and experimental results found in the literature. The black arrow points to the entanglement molecular weight M_e measured by Richter et. al. [4]. The dash-and-dotted line is a guide to the eye of the DPD results and the dashed line manifests a slope of -1.

5.5.7 *Self-diffusion coefficient*

The self-diffusion coefficient $D_{c.m.}$ is a measure of the chain spreading through the accessible volume. Phenomenologically, the kinetics of diffusion is governed by Fick's law and the Smoluchowski equation [115]. Its magnitude strongly depends on the molecular weight and corresponding regimes, which range from a liquid-like behavior controlled by the availability of extra free-volume around chain ends [141, 148, 173], to a Rouse-type regime with $D \sim M^{-1}$ [174], and to an attenuated slowdown due to reptation combined with *constraint release* and *contour length fluctuation* effects [175]. Its calculation from simulations can be performed using Einstein's relation,

$$D_{c.m.} = \lim_{t\to\infty} \frac{1}{6t} \left\langle \left[\mathbf{R}_{c.m.}(t) - \mathbf{R}_{c.m.}(0)\right]^2 \right\rangle . \tag{5.31}$$

The dependece of $D_{c.m.}$ on M_w is plotted in Fig. **??**. The experimental measurements made by von Meerwall et. al. [141] and Pearson et. al. [176] are also included (in this case, the fit of the experimental data is shown). The former represents the sub-Rouse regime described by liquid-like alkane molecules, the second illustrates the trend followed by concentrated melts undergoing reptation. Throughout the range of M_w simulated, the performance is predominantly Rouse-like, with $D \sim M^{1(\pm 0.2)}$ extending to values above M_e. Similar trends have been reported in the literature [133]. As discussed above, the DPD model used cannot capture an eventual slowdown caused by topological constraints, thus the experimental data cannot be accurately reproduced. Only CG-10/5 and CG-12.5 lay below the M_e threshold. The continuous line extrapolates the trend of the experimental results of von Meerwall et. al. [141]

by making a fit that combines Rouse theory with chain-end free-volume effects, also proposed by them. Although unrealistic, the extrapolation justifies the qualitative values of the predictions made here, when neglecting the existence of entanglement constraints.

5.6 CONCLUSIONS

Using a procedure similar to that followed by Guerrault et al. [133], a mesoscopic force field was assembled based on information derived from all-atom atomistic simulations. For three levels of coarse-graining λ, the contributions of the potential energy were parameterized and used as the conservative force for DPD simulations. The *intra*-molecular components were accurately reproduced, but the non-bonded contributions failed correctly reproduce the atomistic pair correlation functions at the short range, revealing excessive particle overlapping. From excluded volume calculations it became clear that this overlapping increased with increasing λ. The same trend was found for the friction coefficient, revealing the predominance of dissipative forces. The mesoscopic systems followed ideal chain statistics ($\langle R_g^2 \rangle \sim M_w^{1.0}$ and $6\langle R_g^2 \rangle / \langle R_{ee}^2 \rangle \approx 1.0$), regardless of the value of λ. Conversely, γ has a remarkable implication on the structure when M_w reaches a critical value.

Atomistic MD simulations deal accurately with the fastest modes, but are computationally too expensive to cover the long time dependence. Conversely, DPD simulations easily attain the longest relaxations and the crossover from sub-diffusive to Fickian regimes. To correct the time scale of the mesoscopic system, a time mapping method [158] was combined with the idea of scaling the friction coefficient [137]. The results for either ϕ_λ or $\phi_{c.m.}$ consistently converged to a unique trend. Also, the time shifts decay exponentially with γ. The interplay between atomistic and mesoscopic simulations enabled to cover the entire dynamical description of the system. A ballistic regime (entirely described by the atomistic system) followed by a sub-diffusive regime (described by atomistic and mesoscopic systems) and a free-diffusive regime (entirely mesoscopic) could be identified. The sub-diffusive region where both models meet represents the slowdown of diffusion caused by the spectrum of chain mode relaxations. Here, the displacement of monomers scales as $\phi_{\lambda=1} \sim t^{0.5}$, as Rouse predictions. With increasing λ, the slope gradually increases towards the direction of a diluted system, with $\phi_{c.m.}$ remaining unchanged. Apparently, the application of scaling rules provided by the mesoscopic model yields results 8% higher than those from their atomistic counterparts.

Using the criteria previously proposed [2, 143, 162, 164], as far as relaxation modes are concerned, the coefficients β_k, $\langle \tau_k \rangle$ and W_k^{eff} were measured. The non-exponential character of the relaxations ($\beta_k < 1$) is weaker in mesoscopic systems, the differences being caused by the enhancement of chain mobility, as a consequence of the soft nature of the interactions. Consistently with the sub-diffusive predictions for ϕ_λ, $\langle \tau_k \rangle$ undergo similar deviations ($\approx 7\%$) and the slopes decrease with increasing λ due to the effect of chain stiffness. The enhancement of stiffness with increasing λ at lower length scales explains the

gradual deviation from Rouse theory and why the scaling law for the sub-diffusive regime loses resolution for mesoscopic systems. It was found that τ_1 is independent of λ. As the shortest relaxation times are not reproduced by the mesoscopic simulations, they were computed from the atomistic trajectories using the coherent dynamic structure factor of the maximum distance between adjacent λ-mer groups. With τ_1 being almost unchanged, and τ_s increasing with λ, the time lag of ϕ_λ dominated by the spectrum of mode relaxations narrows while the slope increases with increasing λ. These predictions are summarized in Table 5.8.

Table 5.8: Subdiffusive parameters estimated from CG-10/10, CG-12.5/8 and CG-20/5 systems. Coarse-graining level λ, segmental relaxation time τ_s (ns) calculated from the underlying atomistic system, longest relaxation time τ_1 (ns) resulting from DPD simulations using $\gamma = 350$ and the time scaling x of the sub-diffusive displacements.

λ	τ_s	τ_1	$\sim t^x$
10	1.16	52.86	0.63
12.5	2.01	52.35	0.65
20	7.72	52.78	0.70

Since the soft repulsion of the interactions enables chains to cross each other, it is unrealistic to assume that entanglements can be neglected. Still, it remains reasonable to unveil the limitations of the model in a phenomenological perspective. The sub-diffusive scaling traced from ϕ_λ showed that the slope changes from 0.66 to 0.5 as M_w increases. Also, when analyzing these results in terms of c/c^* and $V_\cap/V^*$, inconsistencies were found with the data shown by the dynamics and the solubility state of the systems. These were attributed to artificial compressibility. Surprisingly, the M_w value at which the hydrodynamic interactions are fully screened ($V_\cap/V^* = 1$) is independent of λ and the slope of the sub-diffusive regime does not decrease below 0.5. Concurrently, the values of the self-diffusion coefficient fall on the same slope, with a Rouse trend ($D_{c.m.}$) confirming that above τ_1 the translational motion of the chains are not influenced by the magnitude of λ.

6

NON-EQUILIBRIUM MESOSCOPIC SIMULATIONS OF POLYMERS UNDERGOING STEADY AND UNSTEADY SHEAR FLOWS

6.1 INTRODUCTION

Molecular simulations are playing a progressively more important role in understanding the link between properties and molecular structure of soft materials. Non-equilibrium molecular dynamics (NEMD) simulations have been applied to lubricants [177, 178] short polymer chains [179–184] and polymers with different architectures [185]. Despite the adequate accuracy to capture the molecular details, the time and length scales that can be assessed by these simulations are still limited by the currently available computer power. Hence, many authors turned their attention to mesoscopic models that are suitable, to some extent, to deal with the rheological description of higher molecular weight polymers at a much lower computational expense. Amongst these, probably the most popular is the dissipative particle dynamics model, DPD, developed by Hoogerbrugge and Koelman10. In the particular case of polymers, the mesoscopic system represents a coarse-grained description of the atomistic system, where the mesoscopic particles enclose an arbitrary number of monomers with dimensions exceeding the Kuhn length. Although rheological studies using mesoscopic non-equilibrium simulations are abundant [186–188], only a few were based on a systematic multiscale framework. A notable exception is the contribution of Padding et al. [2, 189] on coarse-graining. In these approaches, apart from the conservative forces governed by the Hamiltonian of the mesoscopic system, the role played by the friction and stochastic forces is substantial. In DPD, the choice of the dissipative friction is rather arbitrary. Groot and Warren [151] suggested a friction amplitude of 4.5 based on a balance between time step size, equilibration time and thermal stability during the simulation. Therefore, this value has been often considered independently on the system nature. In the case of low viscosity fluids, the dynamical evolution relies solely on the particles free diffusion, while polymers present a particular dynamic behavior that covers a sub-diffusive spectrum of relaxation times before free diffusion takes place, as discussed in many theoretical [115, 160, 161], computational [1, 2, 109, 162, 163, 190] and experimental [4, 143, 144] studies.

The question here is whether the value of 4.5 is suitable when one is interested in coping with the dynamic subtleties of polymeric systems. Probably, it will depend on the choice of the time step, duration of the simulation and chain length. Simulation of short chains requires time steps much lower than 0.01 to cover the sub-diffusive regimen, whereas very long chains require lengthier simulations to reach the longest relaxation time and the

free-diffusive regime. Some authors developed methods to estimate the DPD friction coefficient, from atomistic simulations [153, 154, 157, 191], but these have not yet been tested for polymer systems. In the previous chapter, the strength of the hydrodynamic interactions was adjusted by choosing the DPD friction coefficient and accommodating the system dynamics to the correct time-scale (e. g., the time-scale dictated by the atomistic system). A change on the DPD friction coefficient influences the mobility of the beads within the chains, since it directly relates to the degree of coupling between the heat bath and the system. It also implies that the physical temperature imposed to the system will change. Thus, the magnitude of DPD friction should simply shift the time-scale of the relaxation spectrum without altering its shape, similarly to a change in temperature [192]. In this way, it is possible to estimate the universal time scaling relation between the friction coefficients and the corresponding time shifts that is required to suitably accommodate the dynamical properties to a predefined reference.

A discussion on how the magnitude of coarse-graining affects the equilibrium properties of linear polymer chains was performed in Chapter 5 by means of DPD simulations using interaction parameters gathered empirically from all-atom molecular dynamics simulations. In this chapter the effort is pursued by showing that the same scaling protocol is applicable to predict rheological properties, through non-equilibrium simulations at different coarse-grained levels.

6.2 CALCULATED PROPERTIES

6.2.1 *Stress tensor*

The components of the microscopic stress tensor can be obtained through the Irving-Kirkwood relation [193],

$$\sigma_{\alpha\beta} = -\frac{1}{V}\left\langle \sum_{i}^{N} m_i v_{i\alpha} v_{i\beta} + \sum_{i}^{N}\sum_{j>i}^{N} r_{ij\alpha} f_{ij\beta} \right\rangle, \tag{6.1}$$

where α and β are the orthogonal directions of the Cartesian coordinates, and V is the volume of the simulation cell. The first sum inside brackets in Eq.(6.1) is the contribution of the kinetic energy tensor, where m_i is the mass of particle i, and $v_{i\alpha}$ and $v_{i\beta}$ are the corresponding α and β velocity components. The second sum accounts for the components of the virial tensor, where $r_{ij\alpha}$ is the α component of the vector describing the separation among i and j particles, and $f_{ij\beta}$ is the β component of the vector force imposed by particle i due to the presence of particle j.

6.2.2 *Material functions*

In a scenario where flow is steady $\dot{\varsigma}_{xy}(t) = \dot{\varsigma}_0$, the shear viscosity η is determined from the constitutive relation

$$\eta = \frac{\langle \sigma_{xy} \rangle}{\dot{\varsigma}_0}, \tag{6.2}$$

where $\langle \sigma_{xy} \rangle$ is the xy-component of the stress tensor averaged over all trajectories. In general, non-Newtonian liquids undergoing shear exhibit elastic effects associated to normal-stress phenomena. Therefore, it is useful to define the first and second normal stress coefficients,

$$\psi_1(\dot{\varsigma}) = \frac{-\left(\sigma_{xx} - \sigma_{yy}\right)}{\dot{\varsigma}_0^2}, \tag{6.3}$$

$$\psi_2(\dot{\varsigma}) = \frac{-\left(\sigma_{yy} - \sigma_{zz}\right)}{\dot{\varsigma}_0^2}, \tag{6.4}$$

where the numerators represent the first and second normal stress differences, N_1 and N_2, respectively.

Before steady-state is reached, material functions are expressed as $\eta^+(t, \dot{\varsigma})$, $\psi_1^+(t, \dot{\varsigma})$ and $\psi_2^+(t, \dot{\varsigma})$, and their definition closely resembles the relations given in Eqs.(6.2)-(6.4).

6.2.3 *Structural order*

The shear-thinning behavior of polymers is accompanied by shear-induced alignment of the chains in the flow direction. These anisotropic effects can be quantified using the order tensor, expressed by the following second order rank tensor [165],

$$\mathbf{S} = \frac{3}{2}\left\langle \frac{1}{N}\sum_{i=1}^{N}\left(\mathbf{e}_i\mathbf{e}_i - \frac{1}{3}\mathbf{I}\right)\right\rangle, \tag{6.5}$$

where $\mathbf{e}_i$ is the unit vector along the end-to-end distance of the molecule i and $\mathbf{I}$ is the unit tensor. The alignment angle of the chains is determined from the angle between the flow direction and the eigenvector corresponding to the largest eigenvalue of the order tensor.

6.3 SIMULATION DETAILS

As already mentioned, DPD simulations are performed in a reduced unit basis. Here, the reduced density ρ^* has the same value of the physical density ρ, and the magnitudes of reduced temperature T^* and mass m^* are set to unity. The time scaling should be adjusted according to the friction coefficient used in the model. The γ dependence on the time shifts $\bar{\delta}$ required to superimpose the mean-square displacements among mesoscopic and atomistic simulations can be fitted to an expression. The reduced units employed are summarized in Table 6.1.

Table 6.1: Scaling parameters for the coarse-grained systems (λ refers to the number of monomers per blob).

	Base unit	$\boldsymbol{\lambda = 10}$	$\boldsymbol{\lambda = 20}$
Length (nm)	$\hat{\sigma} = \sqrt[3]{m_{bead}\rho^*/\rho}$	0.775	0.976
Energy (kJ/mol)	$\hat{\epsilon} = k_B T/T^*$	3.738	
Mass (g/mol)	$\hat{\mu} = m/m^*$	280.54	561.09
Time[1] (ps)	$\hat{\delta} = \tau/\tau^*$	$9652.76\gamma^{-0.809}$	$10290\gamma^{-0.998}$

Table 6.2 presents the mesoscopic systems considered in this work. They were previously equilibrated to a set temperature of $k_B T = 1$ during $2 \cdot 10^6$ steps to achieve quiescent conditions. Then, the periodic cubic cells were allowed to deform due to the action of a constant external shear rate applied along two opposing boundary faces (Fig. 6.1). The algorithm induces a planar Couette flow on the bulk system, equivalent to the commonly employed Lees-Edwards boundary conditions [194]. When shear is applied, the bulk initially undergoes a period dominated by unsteady flow, during which the stress grows, before steady-state is reached. The simulations under non-equilibrium conditions were held through another $2 \cdot 10^6$ steps with time-step $0.001\bar{\delta}$ under continuous shear. The trajectories and thermodynamic data were sampled every 1000 steps. The shear-rate values were set to $\dot{\varsigma} = 0.001\bar{\delta}^{-1}$, $0.005\bar{\delta}^{-1}$, $0.01\bar{\delta}^{-1}$, $0.05\bar{\delta}^{-1}$, $0.1\bar{\delta}^{-1}$ and, $1.0\bar{\delta}^{-1}$. Notice that shear-rate is represented with a $\dot{\varsigma}$ symbol to avoid confusion with the DPD friction coefficient symbol (γ). For each $\dot{\varsigma}$, different magnitudes of γ (2, 5, 95, 200, 350, 500, 750) were used in order to identify the effect of these two parameters on the calculated rheological properties. A total of 168 simulations were performed using the LAMMPS simulation package [150] (*version 5-May-2012*) in a 8 core Xeon E5520 CPU. The positions and momenta of particles in time were updated according to the velocity Verlet integration scheme.

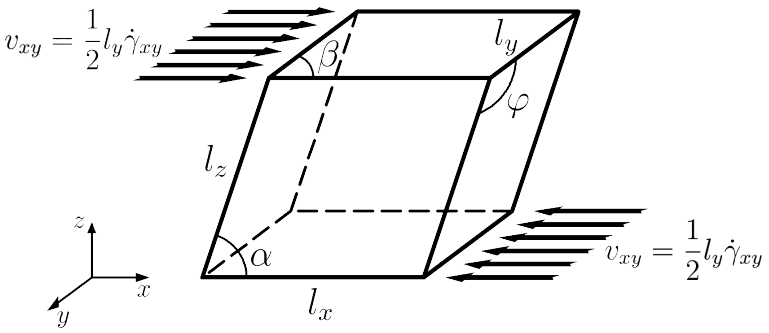

Figure 6.1: Shape of the periodic simulation cell under the influence of planar Couette flow ($\alpha \neq \beta = \varphi = 90°$, $l_x = l_y = l_z$).

Table 6.2: Simulated systems (nomenclature: CG-A/B, with A and B standing for coarse-graining level and number of particles per chain). Chain molecular weight M_w (g/mol), number of chains n_{chains}, and side length of the cubic simulation cell L^* (reduced units).

System	N	M_w	n_{chains}	L^*
CG-10/10	10	2800	175	13.04
CG-10/50	50	14000	34	13.17
CG-10/100	100	28000	34	13.17
CG-20/25	25	14000	70	13.17

6.4 TIME-SCALE MAPPING

Time-scale mapping was accomplished considering how a certain dynamic property under equilibrium is affected when the friction parameter is changed. Fig. 6.2-a displays the mean-squared displacements of the particles, $\phi_\lambda(t)$, and chains center of mass, $\phi_{c.m.}(t)$, in reduced units, for the CG-10/10 system (Table 6.2), using γ's ranging from 5 to 350.

If the data is shifted towards a predefined reference along the time axis, the curves form the mastercurve shown in Fig. 6.2-b. Combining the DPD results with the mean-squared displacements of the corresponding atomistic system (open symbols in Fig. 6.2-b), a subdiffusive regime can be identified. The bottom and top xx axes in Fig. 6.2-b follow two different references. The first is based on the time-scale of the atomistic system (i. e., the physical time), whereas the second concerns the time-scale of $\gamma = 5$. The shift factors, $\bar{\delta}$, were obtained from:

$$\bar{\delta} = \frac{t_{ref}}{t^*}, \tag{6.6}$$

where t_{ref} is the reference time and t^* is the reduced DPD time. As seen in Figure 6.3, $\bar{\delta}$ shares a power-law relationship with γ that can be expressed as

$$\bar{\delta}(\gamma) = \alpha\gamma^{-\beta}, \tag{6.7}$$

where α and β are fitting parameters. The fitting equations, when MD time-scale is the reference, are given in Table 6.1, for the coarse-graining levels relevant to this work. In the case when the time-scale of $\gamma = 5$ is the reference, the parameters are $\alpha = 3.888$ and $\beta = 0.809$. No adjustments are required on Eq.(6.7) if the chain lenght is increased, whereas different coarse-graining levels follow different scaling functions. Since the units of the shear-rate are

reciprocal time units, it can be stated that its scaling function is given by the inverse of the scaling function, $\bar{\delta}^{-1}(\gamma)$, in Eq. (6.7).

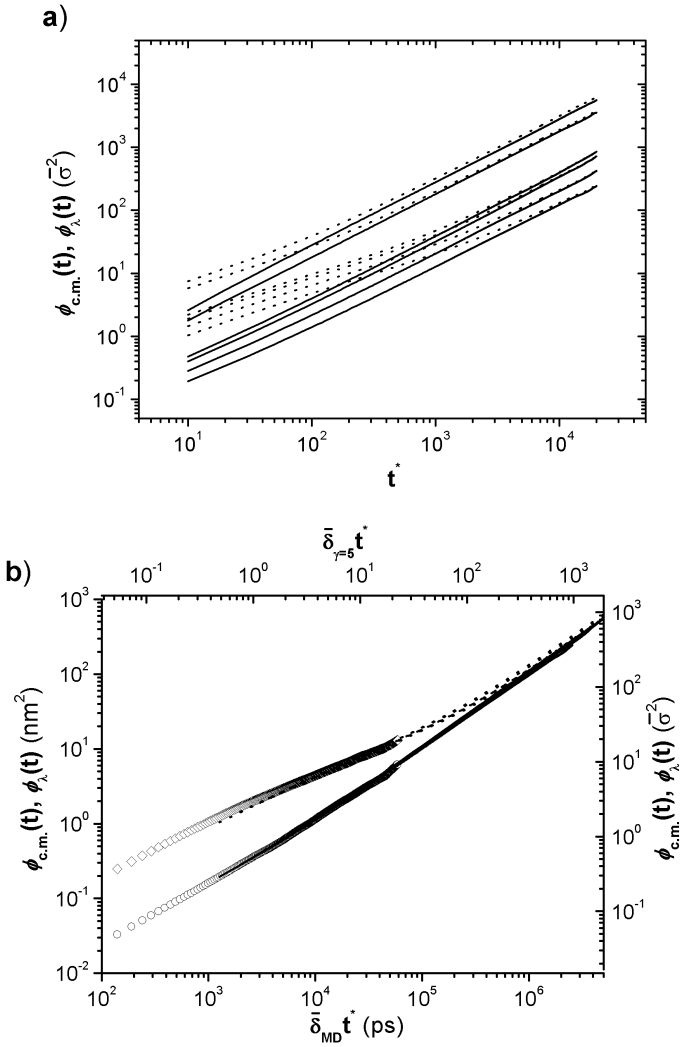

Figure 6.2: Mean-squared displacements of the chains center-of-mass $\phi_{c.m.}(t)$ (continuous lines) and coarse-grained particles $\phi_\lambda(t)$ (dashed lines), a) before time scaling; b) after time scaling. Each curve in a) corresponds to a particular friction coefficient value, ranging from $\gamma = 5$ (highest curve) to $\gamma = 350$ (lowest curve). The top and bottom xx axes in b) concern the $\bar{\delta}_{\gamma=5}$ and $\bar{\delta}_{MD}$ reference,respectively, while the right and left yy axes represent reduced and physical units, respectively. Symbols refer to MD results obtained in Chapter 4.

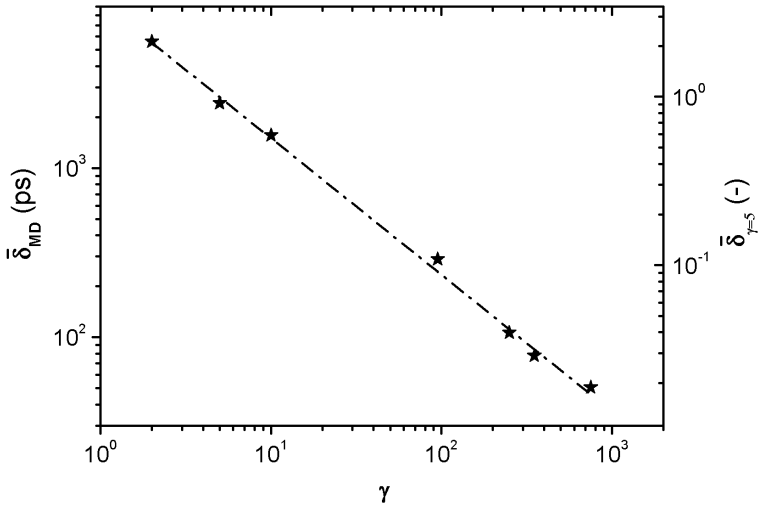

Figure 6.3: Time shifts as a function of $\dot{\gamma}$ for references; $\bar{\delta}_{MD}$ (left axis) and $\bar{\delta}_{\dot{\gamma}=5}$ (right axis).

6.5 RESULTS AND DISCUSSION

6.5.1 *Steady shear flow*

Once the simulations reached steady-state, the stress σ_{xy} was computed by means of Eq.(6.1). Fig. 6.4-a depicts the results the shear stress - shear rate curves for the CG-10/50 system, for various values of $\dot{\gamma}$. Despite the overall shear thinning behavior, the maginute of $\dot{\gamma}$ yields different rheological regimes which can be superimposed by matching the deformation time frame. Applying the scaling protocol presented in the previous section results in the master-curve of Fig. 6.4-b (taking $\dot{\gamma} = 5$ as reference).

In some of the cases tested, the DPD thermostat is not able to dissipate the increase of kinetic energy induced by the external field, forcing the system to reach an undesired thermal equilibrium. For example, Fig. 6.5 presents the influence of $\dot{\varsigma}$ on the average temperature, for the simulations reported in Fig. 6.4-a. When $\dot{\varsigma} = 1.0$, the simulations deviate drastically from the set temperature ($k_BT = 1.0$), while at lower shear-rates the thermal equilibrium is kept independently of the chosen $\dot{\gamma}$.

Fig. 6.6 shows the influence of chain length (systems CG-10/10, CG-10/50 and CG-10/100 in Table 6.2) on viscosity dependence on shear-rate, at identical coarse-graining level. The viscosites were computed using Eq.(6.2) and scaled values of shear-rate ($\bar{\delta}_{ref} \cdot \dot{\varsigma}_0$). To show the correspondence between different references, the bottom and left axes relate to reduced units for $\dot{\gamma}_{ref} = 5$, while the top and right axes correspond to physical units based on the scaling from atomistic simulations. In spite of the molecular weight of the chains being rather small, all the systems exhibited a Newtonian plateau. The transition to the shear-thinning regime is directly related to the point where the shear-rate equals the reciprocal of the chains longest relaxation time τ_0^{-1}. The vertical arrows in the figure indicate τ_0^{-1} of each system, as predicted from equilibrium

simulations (see Chapter 4). The good match between both further supports the consistency of the time-mapping used.

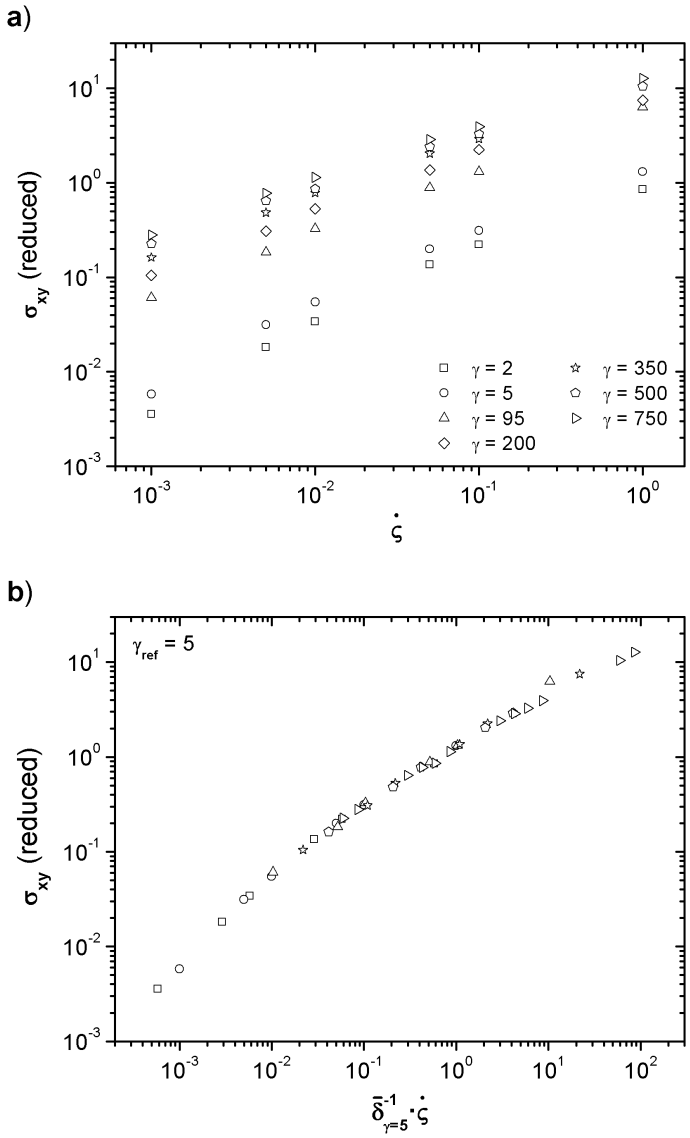

Figure 6.4: Shear-stress flow curves for CG-10/50; a) results before time-scaling and, b) mastercurve taking $\bar{\delta}_{\gamma=5}$ as reference.

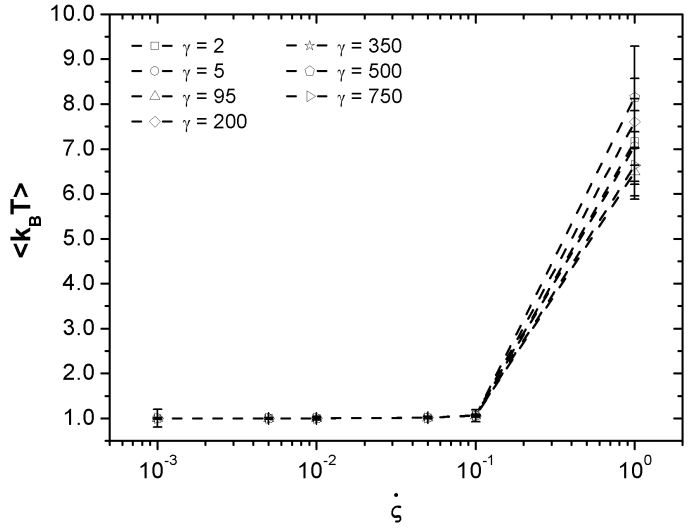

Figure 6.5: Influence of the reduced shear-rate on the thermal equilibrium of the simulations.

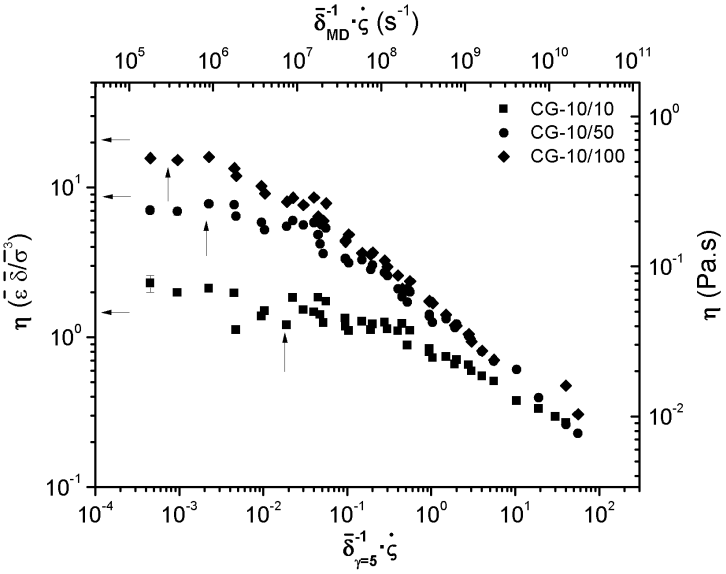

Figure 6.6: Shear-viscosity flow-curves of systems CG-10/10, CG-10/50 and CG-10/100. The shear-rates were scaled for $\gamma = 5$ (bottom and left axes) and MD physical time (top and right axes).

The onset of shear thinning decreases with increasing molecular length, which is consistent with measurements for entangled polymers [195]. The horizontal arrows in the figure indicate the zero-shear viscosity obtained from equilibrium simulations, following the relation proposed by Daivis and Evans [196],

$$\eta_0^{eq} = \frac{V}{10 k_B T} \lim_{t\to\infty} \int_0^t \left\langle \mathbf{P}^{0S}(t) : \mathbf{P}^{0S}(0) \right\rangle dt, \tag{6.8}$$

where k_B is the Boltzmann's constant, T is temperature and $\mathbf{P}^{0S}(t)$ denotes

the symmetric traceless part of the pressure tensor. The operator : implies the double contraction of two second rank tensors. The values of η_0^{eq} correlate very well with the plateau viscosities from non-equilibrium simulations. For the higher molecular weight polymer (CG-10/50 and CG-10/100 systems), the shear viscosity in the shear-thinning region follows a power-law ($\eta \propto \dot{\varsigma}^{-n}$) with the exponent independent of molecular weight.The value of -0.49, is in good agreement with the experimetal exponent of -0.5 found for linear low density polyethylene by Kalyon et al. [197]. In turn, system CG-10/10 shows an exponent of -0.31, which is typical for *n*-alkane fluids, as reported in previous simulations [177, 181] and experimental works [198].

Fig. 6.7 compares the flow curves of CG-10/50 and CG-20/25. These two systems present different coarse-graining levels, but are equivalent in terms of chain molecular weight (see Tablle 6.2). Thus, the good agreement between the curves demonstrate that the steady-shear viscosity may not be affected if the choice of the coarse-graining level extends up to $\lambda = 20$ (this represents 4.3 times the characteristic Kuhn length).

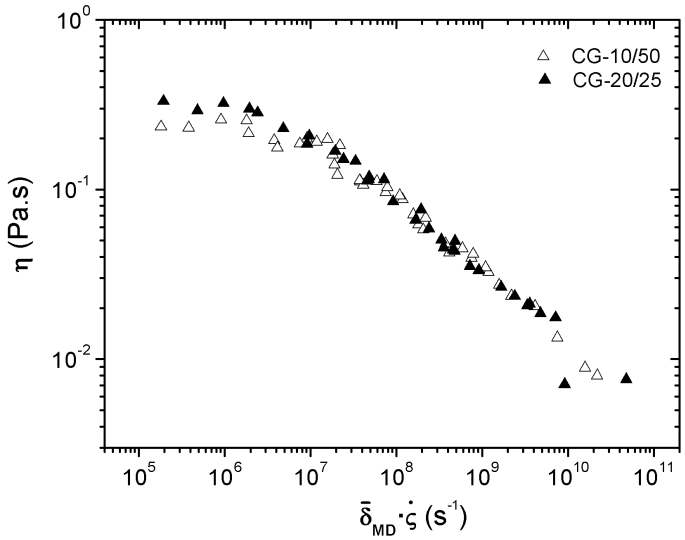

Figure 6.7: Shear-viscosity flowcurves of systems CG-10/50 and CG-20/25, after scaling of the shear-rate.

Fig. 6.8 plots the variation of ψ_1 and ψ_2 with shear-rate, obtained from Eq.(6.3) and Eq.(6.4). Fig. 6.8-a, exhibits a plateau at the lower shear-rate region, followed by a pronounced decay with increasing shear-rate. Such a non-linear behavior indicates that the restoring forces opposing to chain shear alignment leads to unbalanced normal stresses acting on the system [199]. At the same coarse-graining level ($\lambda = 10$), the systems with higher molecular weight converge onto the same non-linear regime. For CG-10/50 and CG-10/100, the slope in the range between 10^8 and 10^9 s^{-1} of CG-10/50 and CG-10/100, is -1.36. This result correlates well with previous studies using non-equilibrium molecular dynamics simulations [180, 181, 200] and mesoscopic simulations [189]. The values of CG-20/25 match well with CG-10/50 at shear-rates below $2 \cdot 10^8$ s^{-1}.

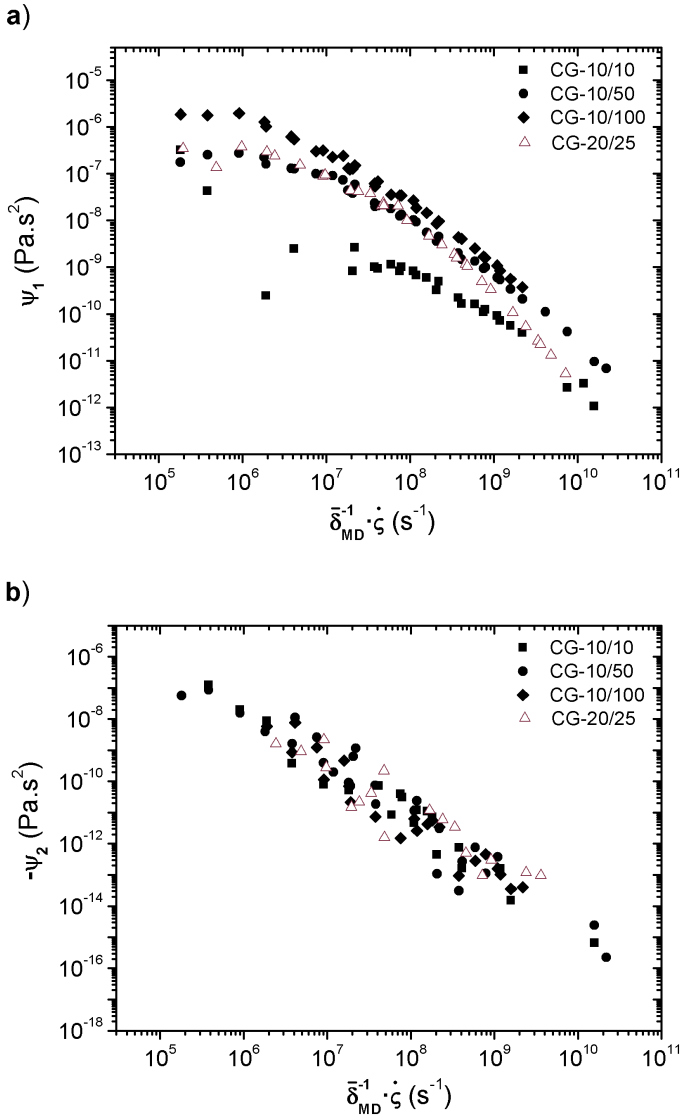

Figure 6.8: Normal stresses coefficient, ψ_1 and ψ_2, of sytems CG-10/10, CG-10/50, CG-10/100 and CG-20/25. Results were scaled to the physical time.

Even without evidence of a plateau, a decay of the second normal stress coefficient $-\psi_2$ is also present (see Fig. 6.8-b). The statistical noise of the results is significant because ψ_2 is based on the difference between two small values. Nevertheless, a liner correlation will yield slopes varying from -1.7 ($R^2 = 0.92$) to -1.72 ($R^2 = 0.95$) with decreasing chain length, which agrees well with previous NEMD simulation [180].

The ratio between N_1 and σ_{xy}, usually designated as stress ratio [201], provides a measure of fluid elasticity. While in Newtonian fluids this value is zero (since $N_1 = 0$), in non-Newtonian fluids it is a monotonically increasing function of shear-rate. Additionally, the shear-thinning regime of ψ_1 develops when the stress ration is approximately one. The results presented in Fig. 6.9 reproduces well the expected depencency for a non-Newtonian fluid. The shear-rates corresponding to $N_1/\sigma_{xy} = 1$ (intersect between the horizontal

dashed line and the curves) are within the same range of those in Fig. 6.8-a for the onset of shear-thinning. Fig. 6.9 also contains data on the variation of N_1 with σ_{xy}. At low shear-rates, the slopes of the curves are 1.76, 1.86 and 1.92, for CG-10/10, CG-10/50 and CG-10/100, respectively. These values seem slightly overestimated, since previous simulations of short *n*-alkanes [202] and experimental results of polymer melts [202] predicted a slope of 1.6.

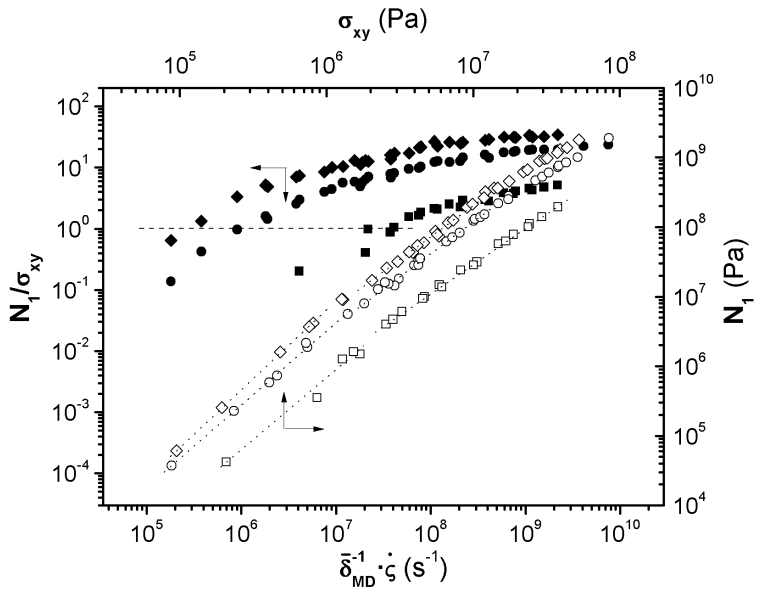

Figure 6.9: Stress ratio vs. shear-rate (filled symbols) and N_1 vs. σ_{xy} (open symbols) of systems CG-10/10 (squares), CG-10/50 (circles) and CG-10/100 (diamonds). The horizontal dashed line is a guide to the eye for $N_1/\sigma_{xy} = 1$ and dotted lines represent the slopes of $N_1(\sigma_{xy})$.

As the shear-rate increases up to values beyond the inverse of the longest relaxation time, the fluid does not have enough time to restore its internal equilibrium energy. Consequently, chains align on the flow direction, in order to relieve the extra stresses caused by the external field, giving raise to the shear-thinning behavior observed in Fig. 6.6. The shear alignment angle relative to the orientation order of the entire chains ensemble can be obtained from Eq.(6.5). For each system studied, Fig. 6.10 shows the dependence on the alignment angle on the Weissenberg number, $We = \dot{\varsigma}\tau_0$. As expected, the results fit within a single curve, i. e., the coarse-graining level has no influence. After a sharp decrease of the orientation angle with We, the chains approach a lower asymptotic limit close to 0.25°. A somewhat higher angle ($\sim 2^\circ - 5^\circ$) has been suggested [181, 189], the differences being probably caused by an limitation of the coarse-grained system to respond to the external field, given the softness of the coarse-grained potential energy combined with the lack of segmental repulsions in the model, making chain alignment more pronounced. Conversely, before the start-up of the orientation process the alignment angle reaches an upper value of 45°, which is consistent with other simulation studies [181, 189].

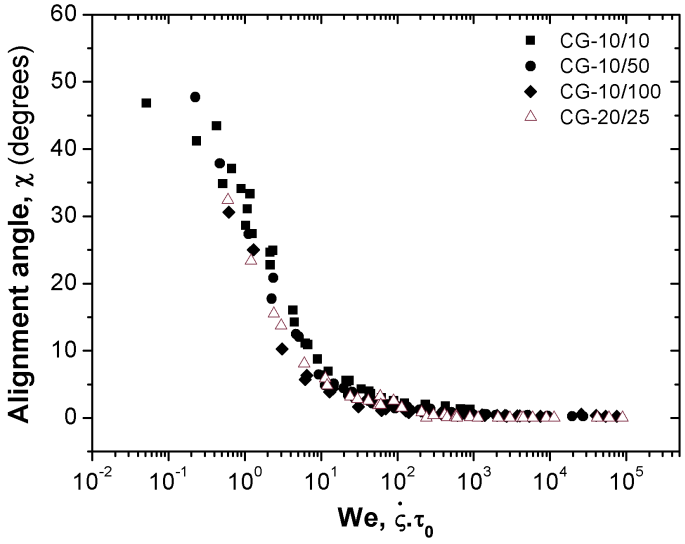

Figure 6.10: Dependence of the alignment angle on the Weissenberg number for systems CG-10/10, CG-10/50, CG-10/100 and CG-20/25.

6.5.2 *Stress growth upon startup of shear flow*

This section discusses whether scaling can be extended to unsteady shear flows, where the evolution of the materials response depends not only on the strain amplitude but also on time. The particular situation in which the fluid at equilibrium is suddenly perturbed by the inception of a constant shear strain rate will be dealt with. When the shear-rate is small, the stress increases monotonically with time before reaching a constant value; at sufficiently high shear-rates (typically larger than the reciprocal τ_0), the fluid departs from the linear viscoelastic regime and a stress overshoot takes place before steady-state is attained. This behavior is common in linear homopolymers and reflects the structural breakdown happening due to the chain alignment in response to the stretching induced by the fast flow. According to the Doi-Edwards model, the maximum shear stress occurs at a total shear strain, $\varsigma \equiv \int \dot{\varsigma} dt = \dot{\varsigma}_0 t$, of about 2, with no evidence of an overshoot related to the fist normal stress difference. Indeed, in comparison with experimental results, the Doi-Edwards model only holds when $\dot{\varsigma}\tau_0 < 1$. However, for high startup shear-rates, experimetal observations of untangled [203] and entangled solutions [6, 204–206] and melts [207–209] show that the maximum shear stress shifts to higher strains. Furthermore, contrarily to Doi-Edwards theory, experiments also show overshoots on the first normal stress coefficient, with maximums occuring at higher strains compared to the shear stress. The literature addresses extended models [210–212] aiming to eliminate the shortcomings of the the Doi-Edwards equation.

Fig. 6.11 shows the predictions of $\eta^+(t)$ and $\psi_1^+(t)$ as a function of total strain. The magnitudes were normalized with the corresponding steady-state values at $t \to \infty$. The previous scaling protocol was used to accomodate the rheological properties of systems with different DPD friction coefficients

to the corresponding physical time scale. The curves corresponding to similar start-up shear-rates exhibit comparable trends, from which three sets of data are distinguishable. All curves present overshoots, the peak value and breadth increasing with shear-rate, in accordance with the results reported by Moore et al. [181] and Padding et al.. [189]. The values of strain where the maxima take place are less evident. With respect to viscosity, they are at least one decade higher than that predicted by Doi-Edwards due to the high Weissenberg numbers ($We > 100$) taken into consideration. Boukany et al. [209] reported a scaling of $\varsigma_{max} \sim (\dot{\varsigma}\tau_0)^{1/3}$ irrespective on the degree of entanglements, where ς_{max} is the strain corresponding to the maximum of the shear stress overshoot. Pearson et al. [5] presented a stronger dependence, $\varsigma_{max} \sim (\dot{\varsigma}\tau_0)^{0.97}$ when $\dot{\varsigma}\tau_0 \to \infty$. Both reproduce well experimental findings [6, 209]. As depicted in Fig. 6.12, even though the values of ς_{max} at $We > 10^2$ computed have the same order of magnitude of those reported ealier, the trends are different.

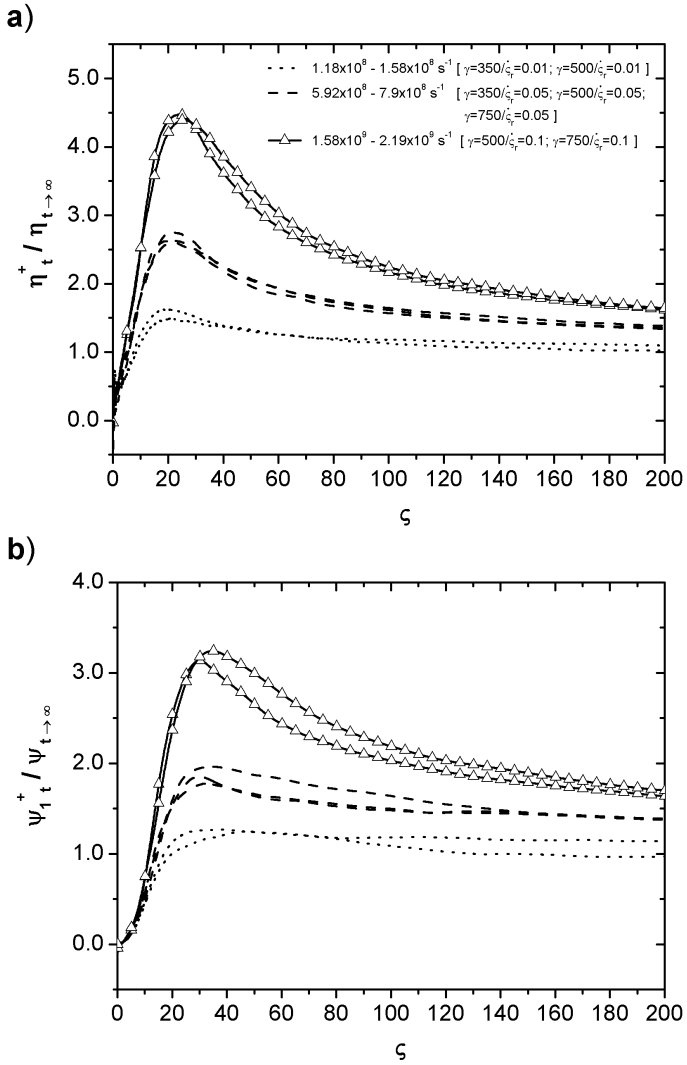

Figure 6.11: Normalized transient material functions at different start-up shear-rates for system CG-10/50; a) viscosity, and, b) first normal stress coefficient.

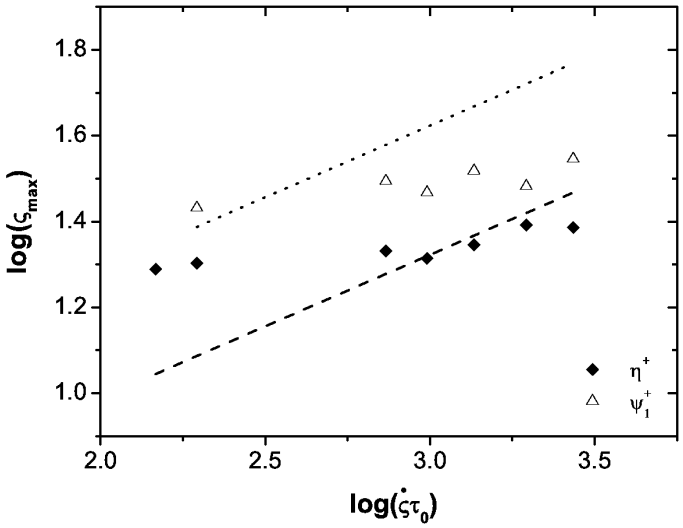

Figure 6.12: Log-log plot between the strains corresponding to the overshoots of η^+ and ψ_1^+, and the Weissenberg number. Dashed lines represents the theoretical predictions of Pearson et al. [5], which are in concordance with the experimetal work of Osaki et al. [6].

The influence of the chain length on the transient properties must follow a similar behavior to the results shown in Fig. 6.11. Fig. 6.13 shows transient viscosity upon strain for systems with different molecular weight. Although, the flow conditions applied to the systems are the same, the Weissenberg numbers are all different since the longest relaxation time is proportional to the molecular weight. The conclusions obtained from the figure are analogous to Fig. 6.11. The increase of molecular weight increases *We* and, thus, the magnitude of the overshoot and corresponding ς_{max}.

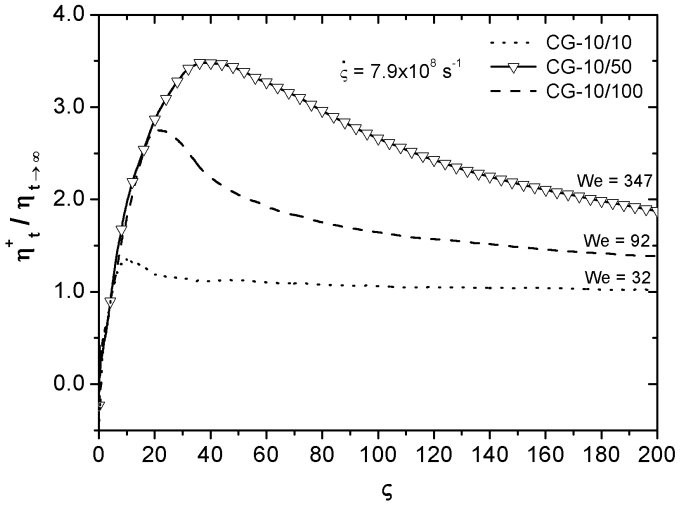

Figure 6.13: Normalized transient shear viscosity of systems with different molecular weight (CG-10/10, CG-10/50 and CG-10/100) but undergoing the same start-up shear-rate.

6.6 CONCLUSIONS

Computational rheology simulations were undertaken by means of the DPD model in order to evaluate the applicability of the time-scaling function reported in Chapter 5. The interaction parameters were empirically obtained *ab initio* from all-atom molecular dynamics simulations.

The time shifts estimated from equilibrium simulations seem to hold for the scaling of the rheological properties obtained from steady and unsteady shear simulations. Indeed, not only all the simulations running with distinct friction coefficients overlap upon scaling, but the time scale is consistent, since: i) in steady-shear, the longest relaxation time predicted from equilibrium simulations matches the onset of shear-thinning, ii) in unsteady-shear, the values of the strain corresponding to the maximum of the stress overshoot compare well with the available experimental data.

As in a coarse-grained model the entire description and processes involved within the fluid are simplified, in contrast with atomistic models, the accuracy of the rheological predictions attained here is somewhat surprising. Still, the slope of N_1 vs. σ_{xy}, the lower limit of the alignment angle and the behavior of ς_{max} with respect to We were somewhat overestimated. The softness of the coarse-graining interactions diminishes the strength of the bonded and non-bonded forces contributing to pressure. Thus, the system becomes less capable to recover the deformations induced by the external field. This fact is aggravated with increasing coarse-graining level, as shown by the elastic effects reported for the CG-20/25 system. Nonetheless, even in this case good correlations were found regarding shear-viscosity and alignment angle.

7

TOWARDS A MULTISCALE APPROACH TO PREDICT THE LARGE-SCALE MORPHOLOGY OF POLYMER/LAYERED-SILICATE NANOCOMPOSITES

7.1 INTRODUCTION

Computer simulations of polymer/layered silicates nanocomposites (PLS), have already been performed for over a decade. Since the earlier works of Vaia and Giannelis [213, 214] and Balazs [215] that address the thermodynamics of the formation of such materials by means of mean-field calculations, there was a tremendous effort to better understand their structure, kinetics and macroscopic properties. In this direction, the applicability of molecular dynamics simulations (MD) to explore the molecular exility, which is sometimes difficult to interpret from experiments, constitutes a remarkable support to material design. For instance, these simulations were used to predict the kinetics of the formation of nanocomposites [216, 217], as well as the relationship between equilibrium properties (e. g., basal spacing, interlayer structure, packing density, dynamics, and cleavage energy) and the chemical nature of organically modified clays [218–224] and intercalated nanocomposites containing different type of polymers [225–231].

It is well known that most of the macroscopic properties of PLS nanocomposites depend on the state of dispersion of the nanoclay platelets in the polymer matrix [35]. When incorporated into a polymer matrix, the clay particles can form agglomerated, intercalated or exfoliated structures, which will exist or co-exist based on the level of dispersion achieved. From a computational perspective, in order to model the state of dispersion, the system size should be large enough to contain a reproducible number of clay layers, which makes it unfeasible for detailed atomistic simulations. Thus, to deal with such a large-scale system at an affordable computational overhead, simulations at a coarser level need to be invoked.

Multiscale simulations based on coarse-graining techniques (CG) have received much attention in the simulations of complex materials having hierarchical features [232, 233]. Apart from the computational advantages, it also provides the benefit of accessing the properties specific to each scale. The most common approach involves message-passing through scales, in which simulations at the finer scale are used to define the parameters of the coarser scale model. Such a mapping scheme, based on coarse-graining techniques, still remains one of the biggest challenges of multiscale modeling. The accuracy and reliability of mesoscopic simulations depend on the quality of the mapping scheme as well as on the methodology adopted to estimate the interaction potentials governing the coarse scale. Some authors [234, 235] addressed this task thermodynamically, with mesoscopic interactions being qualitatively scaled

from solubility parameters or surface energy values obtained from atomistic simulation. Using dissipative particle dynamics simulations [136] (DPD), Fermeglia et al. [236, 237] obtained reproducible results for the density profiles of polymer molecules intercalated in between montmorillonite platelets. However, the level of detail provided by these simulations was still high (restricted to the gallery interlayer), and the shape of the interaction potentials used was erroneous. In the present chapter, an alternative approach is proposed, based on CG techniques [238] that involves the determination of the CG interaction potentials by means of the potential of meanforce, a procedure commonly used for the coarse-graining of polymers [239–242].

Therefore, in this chapter, a novel atomistic-to-mesoscopic multiscale procedure is presented, with the goal of covering the large-scale morphology of PLS nanocomposites. Its simplicity should allow its use even when considering the computational power of current desktop computers.

7.2 COMPUTATIONAL METHODOLOGY

7.2.1 *Atomistic framework*

7.2.1.1 *Models and force field*

The model provided by Heinz and coworkers [243] for the sodium montmorillonite Na^+MMT was adopted. The silicate structure consists of a crystal lattice including an aluminate octahedral sheet linked to two external silicate tetrahedral sheets. The interface between the sheets consists of a mesh of oxygen ions belonging to both, tetrahedrons and octahedrons. Isomorphous substitution within the layer between Al^{3+} to the lower charged metal ion Mg^{2+} generates negative charges on the surface, that are counterbalanced by the Na^+ alkali metal cations located at the clay surface. The chemical formula of the clay is $Na_{0.333}[Si_4O_8][Al_{1.667}Mg_{0.333}O_2(OH)_2]$, representing a cation exchange capacity (CEC) of 90 mmol/100g, resembling the commercial Cloisite® montmorillonite supplied by Southern Clay Products. According to the authors, the structure only deviates 0.5% relative to experimental X-ray measurements and the distributions $Al \longrightarrow Mg$ charge defects are in agreement with solid state NMR data. The dimensions of the periodic cell employed were 25.96 Å and 27.06 Å along the x and y directions, respectively, and for the z direction a large value (250 Å) was given to avoid interactions across the periodic boundaries.

The model structure of the alkylammonium cation was randomly generated with the graphical interface included in the MAPS platform. The quat consists of a dimethyl,dihydrogenated tallow (2M2HT), shown in Fig. 7.1, containing a positively charged head $N(CH_3)_2^+$, and two long hydrogenated tails C_nH_{2n+1} with $n = 18$, that are attached to the quaternary ammonium cation.

Finally, in order to obtain a fine description of the polymer to be included in the nanocomposite system, first it is necessary to assess a representative chain size that reproduces correctly the density of the bulk material. Thus, periodic simulation cells containing polypropylene (PP) and polypropylene

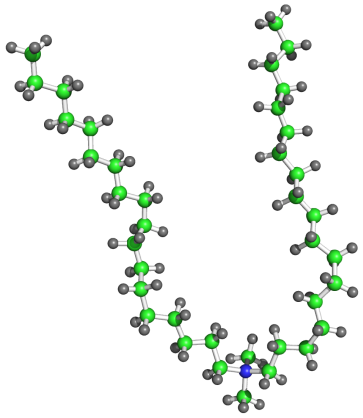

Figure 7.1: Dimethyl,dihydrogenated salt ($N(CH_3)_2^+ - [C_{18}H_{37}]_2$) structure; quaternary ammonium is coloured blue, carbon atoms are green, and hydrogen atoms are grey.

grafted with maleic anhydride (PP-g-MA) chains, with the same degree of polymerization (DP), were generated using the protocol originally proposed by Theodorou and Suter [142], as implemented in the Amorphous Builder module of MAPS (version 3.3). In order to keep coherency between the systems, all were created with approximately the same molecular weight and with a maleic anhydride content of 1%. The number of PP-g-MA chains was always 5, and each chain had only a single MA substituent located at a central monomer. Details of each system are provided in Table 7.1, and the simulation procedure followed to compute the equilibrium bulk density of the systems is summarized in the next section.

Table 7.1: Periodic simulation cells containing PP and PP-g-MA molecules (DP is the degree of polymerization of the chains, N_{PP} and $N_{PP-g-MA}$ are the number of PP and PP-g-MA molecules within the cell, respectively, and M_w is the entire molecular weight of the system in kg/mol).

DP	N_{PP}	$N_{PP-g-MA}$	M_w
10	109	5	48.86
20	52	5	48.74
40	24	5	49.53
80	9	5	47.82
100	6	5	46.97
120	4	5	46.12

The first step for a reliable multiscale method is to ensure the accuracy of the interaction energies between system species, which in great part are sensitive to the non-bonded components (i. e., electrostatics and van der Waals parameters) of the force field employed. The force field adopted in the simulations is an extended version of the polymer consistent force field (PCFF),

including optimized parameters for layered silicates, as introduced by Heinz et. al [244]. Unlike many other force fields, this one proved to be a good choice to obtain a quantitative reliable description of the surface thermodynamics of MMT. Atomic charges for the alkylammonium heads were obtained through a semi-empirical method described in [244]. Therefore, the corresponding partial charges are -0.1e for N and +0.275e for each methyl (-CH_3) and methanedyil (-CH_2-) groups attached to the surfactant head.

7.2.1.2 *Simulation details*

The creation of the atomistic nanocomposite model is a step-by-step process involving the prior equilibration/optimization of each constituent of the system.

The first step involves the simulation of a single MMT layer having Na^+ ions randomly positioned along the surface. Molecular dynamics simulations under NVT conditions were used in order to let the alkali ions reach their equilibrium positions over the surface. After a short run to equilibrate the initial structure temperature at 298 K, a sampling protocol, based on 10 annealing cycles, was undertaken to improve the accuracy of the equilibrium condition. Each cycle includes: i) increase the temperature to 1000K; ii) equilibration at high temperature to enhance the lateral mobility of the Na^+ ions and deliberately rearrange the energy landscape of the surface; iii) decrease the temperature back to 298 K. All stages lasted 20 ps, with the exception of the last equilibration step that was 10 ps longer due to the need to sample and average the energies. The topology of the system relative to the cycle producing the lowest energy was chosen before proceeding to the next step of the simulations.

The MMT surface was organically modified after replacing the alkali ions by the heads of the quat molecules, leaving the organic tails radiating away from the surface. Since the topology of the surface created strongly depends on the conformation of the quat tails, five different structures were created having the positions of the heads fixed. Subsequently, each sample was energy minimized in order to obtain a pre-conditioned structure before NVT dynamics. Simulations with the duration of 1.5 ns were performed at a constant temperature of 298 K, having reached their equilibrium after 200 ps. The remaining of the simulation was dedicated to sample trajectories and thermodynamic data. The uncertainty of the averaged energies between the simulations was small ($\approx$ 0.02%), so these were all taken in for the following simulation step.

Within each periodic cell, a new layer was generated after replicating the existing organoclay layer. The second layer was positioned on top of the original one, in the direction normal to the MMT surface, and separated by a distance large enough to prevent the quat tails of different layers from intersecting the same cross sectional plane. The systems were subjected to further molecular dynamics simulations under NVT conditions during 1.5 ns. Thermodynamic equilibrium was attained after a time similar to the time taken for the interlayer spacing to reach an equilibrium value. The energies and trajectories were harvested every 2 ps during the last 500 ps of each run (well

after the systems were completely equilibrated). Since the aim here is to study the nanocomposite at a realistic melt processing temperature, the organoclay assembly was gradually heated to 473 K during 200 ps, followed by equilibration for another 1.5 ns. Again, outputs were sampled every 2 ps during the last 500 ps.

The simulation cells containing the amorphous polymeric systems (Table 7.1) were first energy minimized and then equilibrated at 298 K through NVT dynamics. Thereafter, simulations lasting 4.0 ns under NPT conditions (1.0 bar and 298 K) were performed in order to relax the volume of the cells and access the corresponding equilibrium bulk densities, ρ_{bulk}. Fig. 7.2 presents the averaged densities resulting from the simulations. It appears that chains beyond a DP of 100 show the same equilibrium density, meaning that beyond this threshold chains can reproduce well most of the packing features of a longer chain. Although this may be not be the case for a confined system, considering a polymer chain with 100 monomers for an intercalated nanocomposite system is so far the best possible approximation.

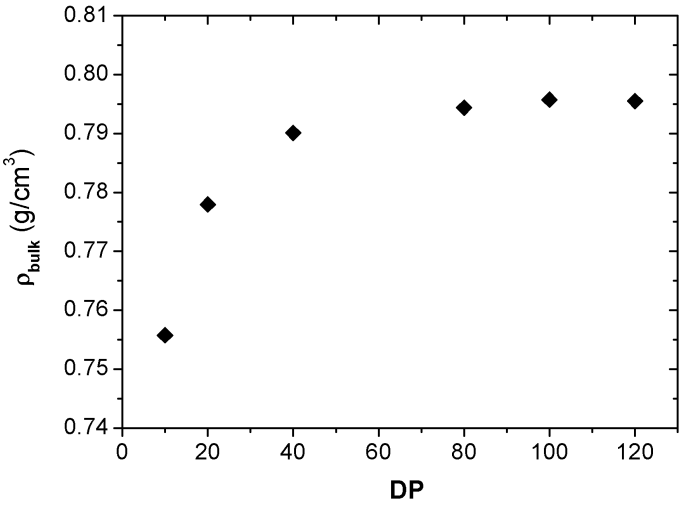

Figure 7.2: Equilibrium bulk density of systems containing polymer chains with different degrees of polymerization.

The nanocomposite model consists of a single PP-g-MA chain intercalated between two modified MMT layers. For this purpose, the double organoclay layer system showing the lowest energy was selected. Further, one of the layers was removed and one of the PP-g-MA chains from the bulk system was introduced at a short distance above the surfactant. NVT equilibration at 473 K was held during 2 ns, letting the polymer chain collapse over the hydrophobic layer formed by the quats. The previously eliminated organoclay layer was then reintroduced to the simulation cell a few picometers above the polymeric phase. The system was then equilibrated under NVT conditions during 1 ns, allowing the PP-g-MA molecule to be sandwiched in between the MMT layers. Next, a production run of 500 ps was carried and data gathering was performed at a frequency of 2 ps.

All atomistic simulations were conducted using the LAMMPS simulation package [150] (version released at *22-Feb-2013*). Regarding the molecular dynamics simulations, the NVT and NPT conditions were facilitated following the Nosé-Hoover phenomenology. Time integration used was the Verlet integrator, with a timestep of 1 fs. The non-bonded cutoff was set to 1.2 nm, and long-range Coulomb interactions were evaluated using the Ewald summation scheme [146], with an accuracy of 10^{-5}. For the energy minimization steps, the conjugate gradient algorithm was used, with stopping tolerances of 10^{-10} kcal/mol and 10^{-10} N for energy and force, respectively.

7.2.1.3 *Thermodynamic considerations and binding energy calculations*

The thermodynamics that drives the miscibility of the components, and thus the formation of intercalated and/or exfoliated nanocomposites, is understood in terms of the changes in the total enthalpy that are necessary to overcome the entropic penalty rendered by the confining polymer inside the gallery [213, 214]. A good enthalpy of mixing for the organoclay is achieved when the polymer-MMT interactions are more favorable than the surfactant-MMT interactions. Earlier experimental observations [106, 245, 246] have shown that non-polar polymers, such as PP, can originate well intercalated and exfoliated nanocomposites via melt intercalation processes, when modified with compatibilizers capable to associate interactions with the clay. The presence of MA grafted to the PP chain renders an excellent propensity to form hydrogen bonds with the polar surfaces of MMT (favorable enthalpic contribution). In addition, the role of the surfactant chains is to reduce the surface energy of the inorganic host, by enhancing the number of hydrophobic contacts at the surface. The miscibility of the nanoclay in the matrix is then improved by means of the dispersion forces between the apolar PP and the surfactant tails. Furthermore, the nature of the organic modifier has a tremendous effect over the interactions among the constituents. It is believed that the double aliphatic tails contained in 2M2HT empowers a stronger shield within the gallery [247], thereby favoring the interactions with the apolar PP.

Based on the calculations performed by Fermeglia et al. [228] and Tanaka et al. [248], details from the system energetics were measured in terms of the binding energy values, E_{bind}, between the species forming the nanocomposite ternary system, i. e., montmorillonite clay, surfactant and polymer. The conclusions obtained from the binding energies can be correlated with the free energy, if changes in entropy are indeed small enough to be neglected. In fact, after equilibrium being reached, the total entropy is almost unaffected, since the interlayer spacing of the PP-g-MA/organo-MMT system only undergoes small fluctuations. Thus, an analysis based on the binding energies is perfectly acceptable. For the binding energy calculation, the non-bonded energies (van der Waals and Coulombic energies) were split from the total potential energy. By definition, E_{bind} is the negative of the interaction energy ($E_{bind} = -E_{nb}$). Thus, in order to compute the binding energy between species, i. e., $E_{bind}^{PPgMA/MMT}$, $E_{bind}^{PPgMA/2M2HT}$, $E_{bind}^{2M2HT/MMT}$, simulations dealing with the binary systems are required. The starting point is to

consider the PP-g-MA/organo-MMT system resulting on the lowest total energy and delete one of the species, say 2M2HT molecules, and further run NVT dynamics of the remaining system to compute the binary interaction energy $E_{nb}^{PPgMA-MMT}$. Next, after deletion of the MMT molecules, the system is left with only the PP-g-MA chain, which is further subjected to NVT dynamics, its energy (E_{nb}^{PPgMA}) being calculated. Identical step was performed for the MMT molecules and calculated E_{nb}^{MMT}. $E_{bind}^{PPgMA/MMT}$ can be calculated from:

$$E_{bind}^{PPgMA/MMT} = E_{nb}^{PPgMA} + E_{nb}^{MMT} - E_{nb}^{PPgMA-MMT}. \tag{7.1}$$

The same procedure was repeated for the binding energy calculations of the remaining binary combinations.

7.2.2 *Mesoscopic framework*

7.2.2.1 *Coarse-graining model*

The mapping scheme of a coarse-graining model involves grouping a specific number of atoms into a CG particle. The coordinates of the underlying atoms are averaged to give place to a CG site that locates the center of mass of the CG particle. The interactions contributing to the CG potential energy consist of a sum of non-bonded and bonded potentials. In this work, solely non-bonded and bond stretch potentials were considered. These can be estimated from the Boltzmann inversion (BI) of the probability distribution function, $P(q)$, of the CG degrees of freedom, q, averaged from the basic atomistic system,

$$U^{CG}(q) = -k_B T \ln P(q). \tag{7.2}$$

When $P(q)$ represents the pair correlation function, $g(r)$, between non-bonded CG sites, the result is a potential of mean force that can be used as a intermolecular interaction potential. The derived potential of mean force cannot be considered an effective potential, unless the system is on the limit of zero density. Packing considerations in dense systems, such as polymer melts, or the nanocomposite system dealt with here, have a profound influence on the molecular conformational state. In situations where entropic effects play a bigger role, it is preferable to invoke more refined methods, in order to optimize the shape of the interaction potential.

The iterative Boltzmann inversion scheme, IBI, is a structure-based coarse-graining technique used to optimize the CG potentials in such a way that the distribution functions resulting from the mesoscopic simulation resemble those obtained from atomistic simulations. Highlights of the algorithm are briefly outlined here, a more detailed description being addressed elsewhere [238]. Similarly to most optimization algorithms, IBI is an iterative process, where the interaction potential is refined at the end of each iteration bymeans of a correction term. The potential of mean force resulting from the Boltzmann inversion constitutes a good initial guess for starting the process. Each

iteration consists of a CG simulation that uses the corrected potential from the previous iteration, to yield a new $g(r)$. The correction term is given by:

$$\Delta U(r) = -k_B T \ln\left(\frac{g(r)}{g_0(r)}\right), \tag{7.3}$$

where $g_0(r)$ is a target distribution function, corresponding to the radial distribution function between the center of mass of CG representations at the atomistic level. Convergence is approached when $g(r)/g_0(r) \approx 1$. The algorithm can also be used for the optimization of intramolecular potentials. However, a simple Boltzmann inversion of the normalized bonded distribution functions is acceptable, since these interactions are relatively strong and rather unperturbed by the non-bonded interactions.

Although IBI provides potentials that accurately reproduce the structure of the system, it is still not sufficient to reproduce a coherent thermodynamic state. This requisite is overcome when the pressure is corrected during the IBI process. This involves an additional term acting over the long-range of the updated non-bonded potential, with the form:

$$\Delta U^{pressure}(r) = A\left(1 - \frac{r}{r_c}\right), \tag{7.4}$$

where A is a constant (=-0.1$k_B T$), and r_c is the cutoff radius. The idea behind this additional term is to add an extra constant force that leads to a constant shift in pressure.

Even if the techniques to estimate the effective potentials are well established, the procedure to build the entire CG force field for a large-scale polymer / organo-MMT system remains laborious. First, in order to map the potential energy with good resolution, computationally demanding atomistic simulations enveloping different morphological states of the system are required. These encompass systems with a reproducible number of MMT layers adopting different levels of dispersion, and polymer molecules located at the bulk and confined spaces. Second, complicated sampling protocols may be required to estimate the potential of mean force. Thus, in this work, a simplified methodology is proposed where the interactions are estimated by parts, i. e., while interactions involving PP and PP-g-MA particles are gathered from a bulk system, those with respect to the modified clay are mapped from isolated systems.

The effective potentials involving PP and PP-g-MA particles were derived using the IBI method, as implemented in the VOTCA package [249] (version 1.2.3). Fig. 7.3 shows the mapping scheme proposed for the polymer system. As seen in Fig. 7.3-a, each CG particle contains the equivalent of ten consecutive monomers of the polymer chain. Two different particles are distinguished, those including exclusively ten PP monomers (dubbed as P), and those containing nine PP monomers and the monomer with the MA substitution (dubbed as A). The target radial distribution functions between P/A, P/A and A/A pairs were measured in terms of the CG sites encountered in the equilibrated bulk

polymeric system having $DP = 100$. The non-bonded potentials required to initiate the iterative process were estimated from the Boltzmann inverse of the target distributions. The stretch potentials relative to P-P and P-A bonds were obtained the same way as the non-bonded terms. The CG simulation cell containing the CG coordinates averaged from the atomistic topology was replicated on each dimension with the aim of increasing the magnitude of the system and improve the statistics (see Fig. 7.3-b). Iterations were handled under NVT conditions using a Langevin thermostat, a timestep of 0.001 ps, a simulation time of 500 ps, and a van der Waals cutoff of 2.5 nm. The simulations were performed using the GROMACS simulation engine [250] (version 4.5.4). Moreover, the potentials were updated sequentially in separate iterations. The update of the pressure correction was considered on the subsequent iterations of each potential optimization. The process was halted after all the potentials reached convergence.

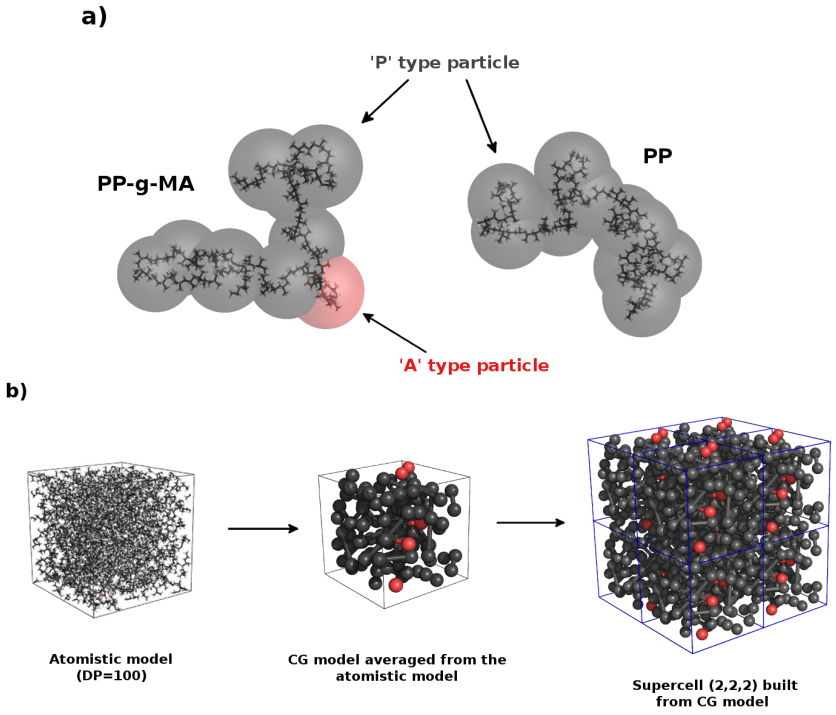

Figure 7.3: Coarse-graining mapping scheme for the bulk polymer system. In a), P type (grey) and A type (red) CG particles enfold 10 monomers from the underlying atomistic molecules. In b), the atomistic simulation cell is mapped onto a coarse-grained cell consistent with the CG site coordinates. Furthermore, the simulation cell is replicated to increase the number of molecules for the IBI process.

Fig. 7.4 shows the CG model ascribed to the organoclay. In this case, the coordinates of the MMT CG particles (dubbed as M) match the positions of the Al and Mg atoms located at the cross-section of the MMT molecule. Note that the presence of the quat molecules is neglected in the mapping scheme. This assumption holds when the quat molecules existence is artificially taken into

consideration on the non-bonded potential shape. The pairwise non-bonbed interactions involving polymer and MMT were estimated from MD simulations of an isolated system containing a single layer of MMT with the surfactant molecules at the surface and a PP-g-MA chain. After reaching equilibrium, the radial distribution functions between CG sites were sampled and averaged over the entire trajectory. Subsequently, the CG potentials were derived from a simple Boltzmann inversion. Similarly, the interactions between MMT particles were taken in from the double layer organoclay system at equilibrium basal spacing.

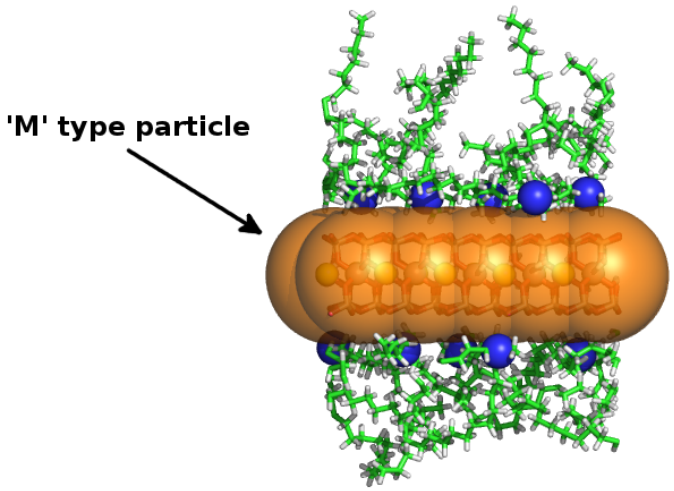

Figure 7.4: Mapping scheme of the silicate domains represented by the particles in orange.

7.2.2.2 *Parametrization of the CG potentials*

The CG potentials were fitted into mathematical expressions suitable to be introduced in a mesoscopic simulation code. Due to the high level of coarse-graining considered, the mesoscopic potentials usually require an extrapolation to soften the repulsive energy at short-range distances. Hence, the fitting expressions for the non-bonded and stretch interactions are:

$$U_{fit}^{nb}(r) = \sum_{k=(s,i,l)} \beta_k \exp\left(-\frac{3}{2a^2}\omega_k r^2\right) \tag{7.5}$$

and

$$U_{fit}^{b}(r) = b_0 e^{-(r/b_1)^2} + b_2 e^{-(r/b_1)^2} + b_4 r^{b_5}. \tag{7.6}$$

The parameters β_k and ω_k in Eq. (7.5) represent the strengths and ranges of short-, intermediate-, and long-range interactions. This function gives the possibility to add an attractive part to the potential, usually long-range. On the other hand, the short-range part is purely repulsive and the intermediate-range provides an extra degree of freedom to the fitting process. Moreover,

Eq. (7.6) offers the fitting equation for the stretch potential proposed by Guerrault et al. [133], defined by a first exponential contribution to fit the short-range bond repulsion, a second exponential to fit the shape of the potential barrier at the region of the bond equilibrium distance, and a polynomial term to fit the potentials long-range section.

Having performed the fittings, the negative of the potentials was differentiated to obtain the corresponding non-bonded and bonded forces ($F = -\nabla U(r)$). Furthermore, the resulting set of forces related to the interactions were introduced in the DPD equation as a replacement of the original soft-repulsive conservative force.

7.2.2.3 *Mesoscopic cell and simulation details*

The mesocopic cell containing the PLS nancomposite was built in accordance with the formulation used in a previous experimental [107]. The percentages of PP, PP-g-MA and clay fillers were 87.3% , 5% and 7.7%, respectively. The polymer molecules were assembled having 50 beads along the backbone and with a complete random conformation. Each PP molecule was entirely formed by P type particles, different from the PP-g-MA molecules that had one of their central particles with an A type particle representing the compatibilizer. The organo-MMT molecule was represented by rigid particles forming a disk-shaped cluster with a diameter of 16.8 nm, a height of 1.0 nm and a particle number density of $\rho^* = 5.0$. It is well known that the length of a nanoclay layer can extend up to several microns, which is substantially larger than the clay entities adopted here. This constitutes an approximation sustained by the need of finding a balance between system size and required computational time.

The components of the mesoscopic system and the corresponding simulations cell are illustrated in Fig. 7.5. The initial state of the system was created using Packmol [251] (version 13.066). The base units of length, $\hat{\sigma}$, were taken from the relation between the physical density of the bulk polymer and an arbitrarily chosen reduced particle density, through $\hat{\sigma} = \left(m_{bead}\rho^*/\rho^{bulk}\right)^{1/3}$ (m_{bead} is the mass of 10 consecutive PP monomers). By choosing $\rho^* = 3.0$ for the bulk polymer, in accordance with the rule of mixtures, the system results in a mesoscopic cell having a particle density of 3.153 and side length of 32.5 nm. The mesoscopic simulation was performed using the DPD model at $k_BT = 3.932$, friction coefficient of 4.5, a timestep of 0.001, $2 \cdot 10^7$ steps and the trajectories were sampled every 10000 steps. The potentials were dealt in reduced values and the non-bonded forces between polymer particles sharing a bond and particles belonging to the same MMT molecule were turned off.

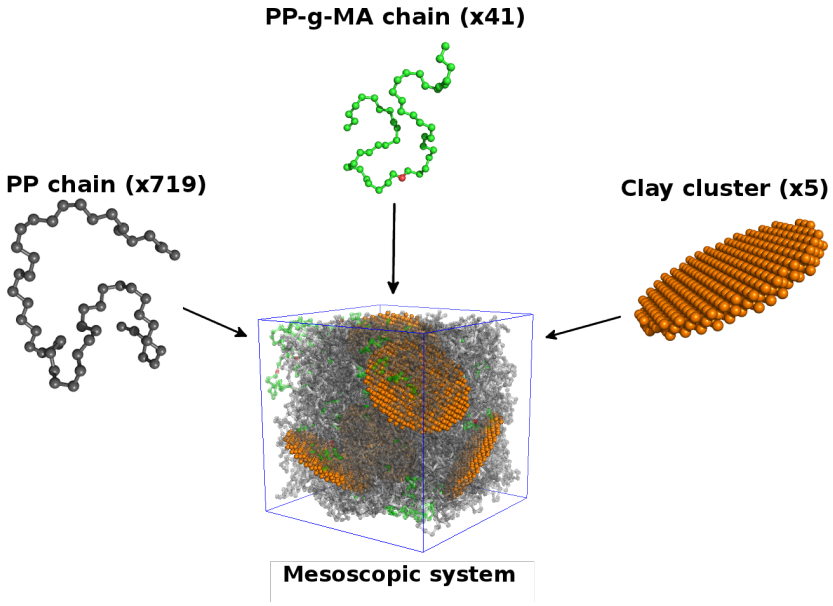

Figure 7.5: Mesoscopic system containing 719 molecules of PP, 41 molecules of PP-g-MA and 5 MMT platelets. T type P particles of PP-g-MA are represented in green to distinguish them from the PP molecules.

7.3 RESULTS AND DISCUSSION

7.3.1 *Atomistic simulations*

7.3.1.1 *Single montmorillonite layer*

Before adding the quat molecules to the pristine MMT surface, the alkali sodium ions are ionically attracted to the MMT surface close to the negatively charged holes localized at the center of the MMT layer. Additionally, the Na^+ cations remain within the surface cavities of the MMT (Fig. 7.6-a) and are prevented from possible jumps towards adjacent cavities. In contrast, after surface modification, the bulky methylene groups bonded to the quaternary ammonium heads shield part of the electrostatic attraction with the MMT surface. Consequently, a gap between surface and quat head is formed (Fig. 7.6-b), inhibiting the formation of hydrogen bonds between the methyl groups attached to N+ and the MMT surface. The propensity for the heads to move towards more electronically favorable positions is restrained by the presence of the quat tails, which are densely spread over the entire surface. The driving forces making sections of the apolar tails to lay flat over the polar MMT surface are merely physisorptive.

7.3.1.2 *Organoclay interlayer*

This section aims at providing an insight into the interlayer morphology as well as into the energetics at the interlayer spacing, and thus establish whether they confirm previous analyses [219, 220, 222, 223]. Although the nonpolar na-

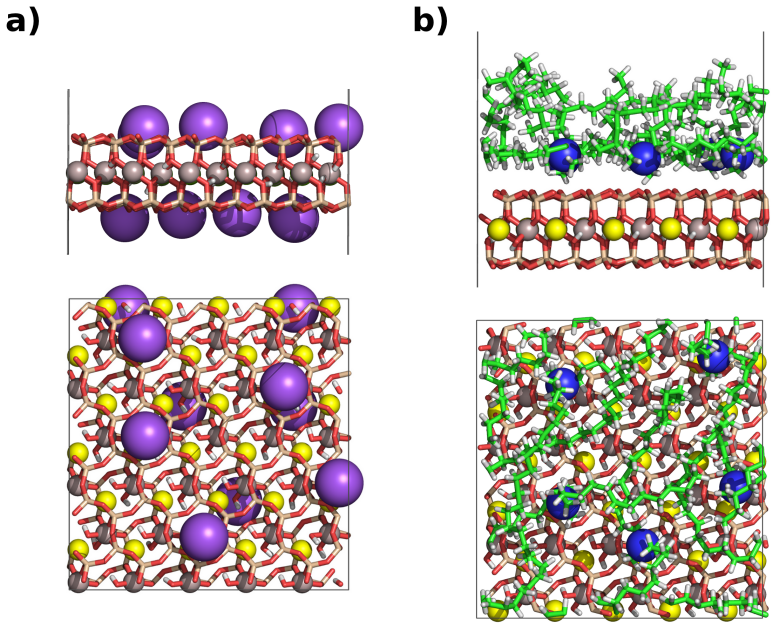

Figure 7.6: Snapshots from simulations of a) pristine MMT and b) organophilic MMT, showing top and side views of the simulation cell. Ionized atoms are represented by spheres [Na^+ (violet), Al^{3+} (grey), Mg^{2+} (yellow),N^+ (blue)]; beige and red sticks represent the Si and O atoms from MMT, respectively, and green sticks refer to C atoms from the quat molecules.

ture of the hydrophobic tails reduces the electrostatic interactions between silicate layers, the attractive effects are still present even when the temperature is increased. The basal spacings were measured in terms of the distance separating the middle cross sectional plane of the MMT layers and averaged over time. The simulation at 298 K resulted on a basal spacing of $2.74^{\pm 0.02}$ nm, in agreement with previous calculations [220] obtained using a similar CEC and surfactant, and X-ray measurements [107]. After increasing the temperature to 473 K, the interlayer gap increased to $3.05^{\pm 0.07}$ nm.

Fig. 7.7 displays snapshots of the interlayer region and corresponding density distributions of the quat molecules at the gallery. In order to better distinguish the quats adsorbed by top and bottom MMT surfaces, the carbon atoms were colored in green and orange, respectively. At 300 K (Fig. 7.7-a), a typical pseudoquadrilayer pattern formed by the alkyl tails is recognizable, analogous to the structure obtained by Zeng et al. [220]. While the nitrogens are electrostatically attracted to the MMT surfaces, the tails belonging to each side of the gallery seem to evolve in a stepwise fashion between ordered and disordered conformations producing well defined bilayers, a feature supported by NMR experiments [252]. Since the organic species tend to fill the available free volume, there is a probability of finding some segments occupying positions dominated by the presence of quats from opposing sides of the gallery. The situation becomes changes slightly at a higher temperature, as revealed in Fig. 7.7-b. The density distribution indicates a weaker layered patterning at the center of the gallery, sustained by the non-preferred arrangements de-

veloped at that location by some tail segments. Thus, while the latter favor a liquid-like structure, segments closer to the quat heads form monolayers rich in anti-conformers. This conclusion agrees well with earlier XRD measurements made by Osman et al. [253].

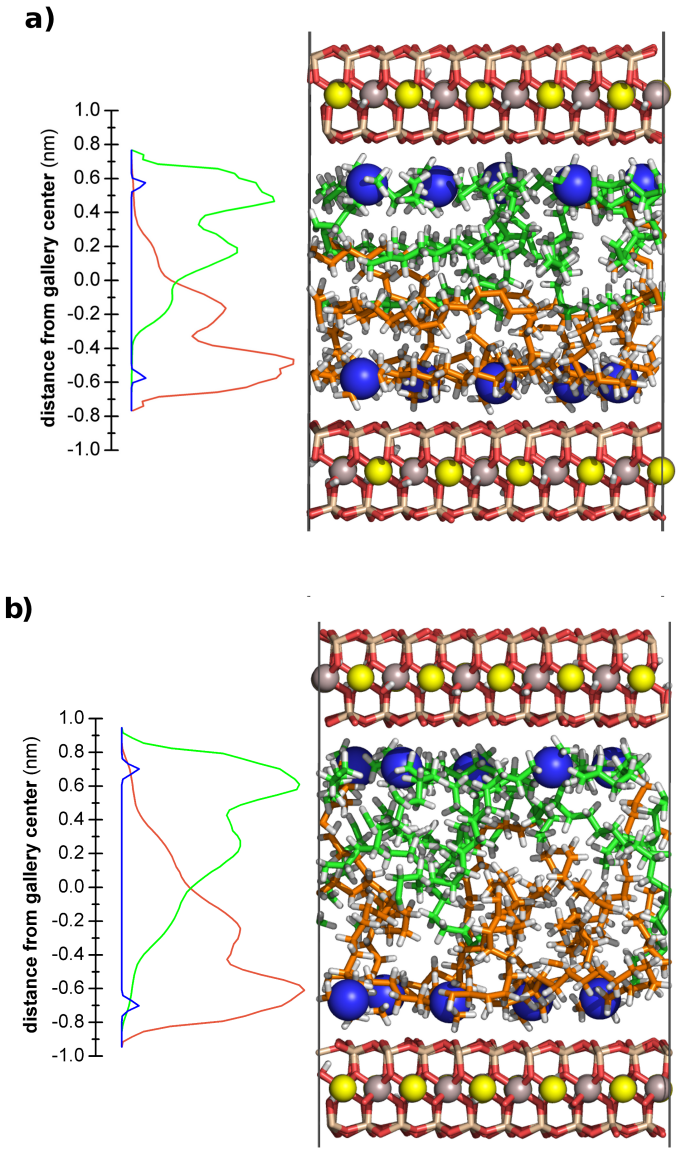

Figure 7.7: Interlayer structure of organically modified MMT with 2M2HT and corresponding density distributions.

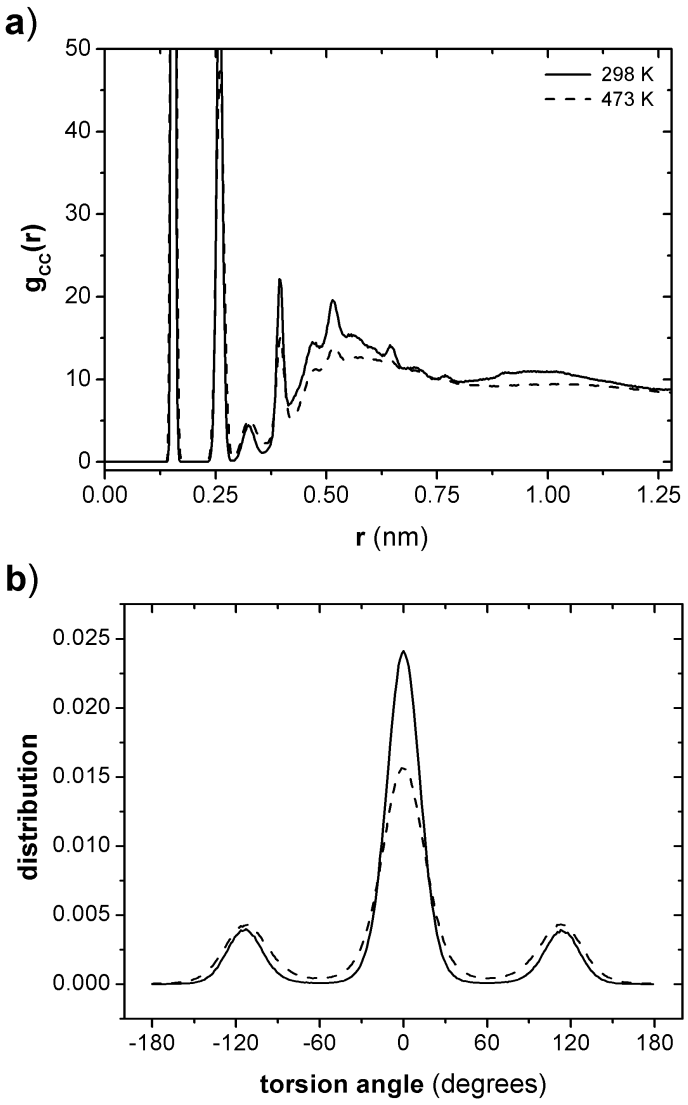

Figure 7.8: a) Radial distribution function between C atoms, and, d) distribution of the torsion angles along the quat tails, of systems simulated at 298 K (continuous line) and 473 K (dashed line).

The conformational state is thus analyzed in terms of the radial distribution function, g_{CC}, between C-C pairs exclusively belonging to the quat tails, and the corresponding torsional angle distribution. These properties are presented in Fig. 7.8. The two peaks at ∼0.15 and ∼0.25 nm in Fig. 7.8-a correspond to carbon atoms separated one and two bonds from the reference carbon, respectively. Peaks at ∼0.31 and ∼0.39 nm correspond to carbon atoms separated by three bonds in *gauche* and *trans* conformations, respectively. The small peak at ∼0.46 nm reveals a successive existence of *trans-gauche* conformers represented by the separation between a sequence of five carbon atoms along the tail. The same sequence also creates a sharp peak at ∼0.50 nm, revealing successive *trans-trans* conformers. The latter indicates that several torsional sequences along the tails are completely stretched. Comparing the two curves, the system at 298 K undoubtedly shows a higher population of *trans* conformations reflected by the peaks intensity at 0.39 and 0.50 nm. Still, the system at 298 K presents two extra peaks, one at ∼0.64 nm corresponding to 1-6 carbon sequence at successive *trans-trans* conformations, and a broad peak at the long-range ∼1.0 nm, which possibly represents the carbon atoms belonging to an adjacent surfactant layer. Fig. 7.8-b shows a torsional angle distribution along the alkyl tails backbone; with an increase of temperature, the degree of ordering reflected by the *trans* conformations is substantially diminished, yielding more randomly disordered conformations expressed by the broadening of the *gauche* conformation peaks. However, there is still a prominence of lower energy conformers, which is related to alkyl segments next to the quat heads resting flat and parallel to the MMT surfaces.

7.3.1.3 *Intercalated polymer chain*

The equilibrium topology of a system consisting of a single PP-g-MA molecule ($DP = 100$) confined between two organophilic MMT layers is presented in Fig. 7.9. To better elucidate the quat tails conformational state, the apolar fragments of the polymer are represented with some degree of transparency, while the polar MA is kept opaque. The corresponding equilibrium basal spacing obtained was $4.49^{\pm 0.85}$ nm, which is well within the typical range measured by experiments [254]. According to the density distribution, it is striking that the polymer is completely packed between the layers and that the quat tails scatter towards the center of the gallery, thus demonstrating their preference to interact with the polymer instead of the clay. This shows that the dispersion forces involving tails and polymer are stronger than those pertaining to tails and clay. However, during the entire simulation there was no evidence of MA→MMT hydrogen bond formation. The MA monomer frustratingly attempts to migrate towards the MMT surface, but its journey is precluded by a highly populated surfactant layer.

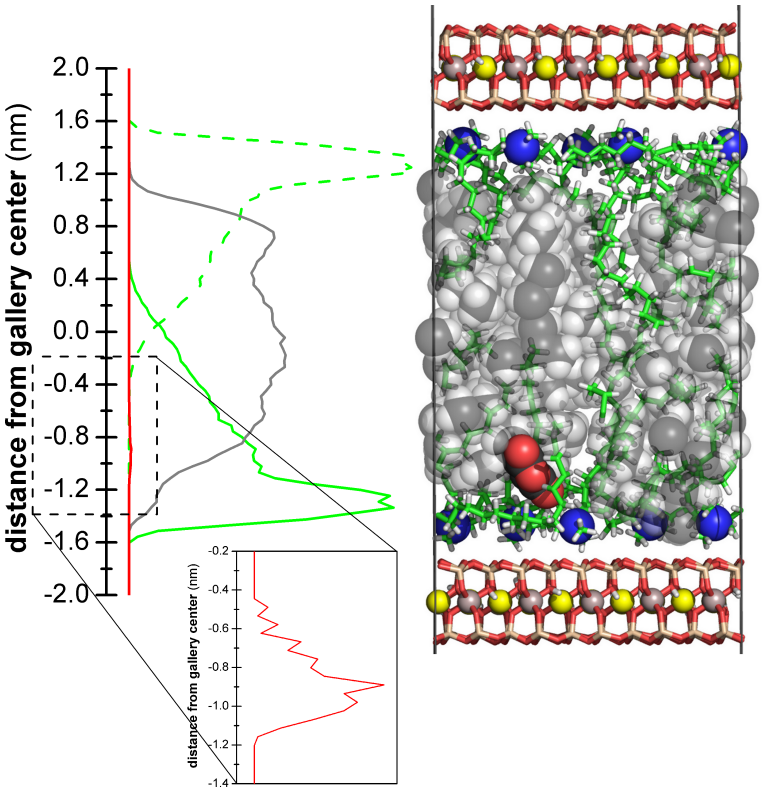

Figure 7.9: Intercalated PP-g-MA chain between organoclay layers and corresponding density profiles of the species; surfactants in green, PP in grey, oxygens from MA in red. Continuous and dashed lines correspond to surfactant adsorbed by the lower and upper layers, respectively.

Fig. 7.10 compares the intercalated PP-g-MA molecule and a single chain of PP-g-MA in the bulk in terms of structure. The radial distribution function curves in Fig. 7.10-a correspond to the distances of carbon atom pairs along the polymer backbone. The curves cotresponding to the bulk and intercalated systems perfectly fingerprint an amorphous morphology, where alternating *trans-gauche* events dominate the conformational state (represented by the peaks at ∼0.45 nm). The peak heights of the intercalated system are higher since the chain is found in a confined and densely packed medium. In addition, the temperature has no immmediate influence on the PP-g-MA structure, apart from reducing the amount of *trans* and *gauche* conformers, as depicted in Fig. 7.10-b. In turn, quat tails segments inside the nanocomposite interlayer conserve their ordered integrity, as demonstrated by the peak at ∼0.5 nm in Fig. 7.10-b and by the high degree of anti-conformers seen in Fig. 7.10-b. Such ordered segments are mostly located at the regions near to the MMT surfaces, as discussed before for Fig. 7.7.

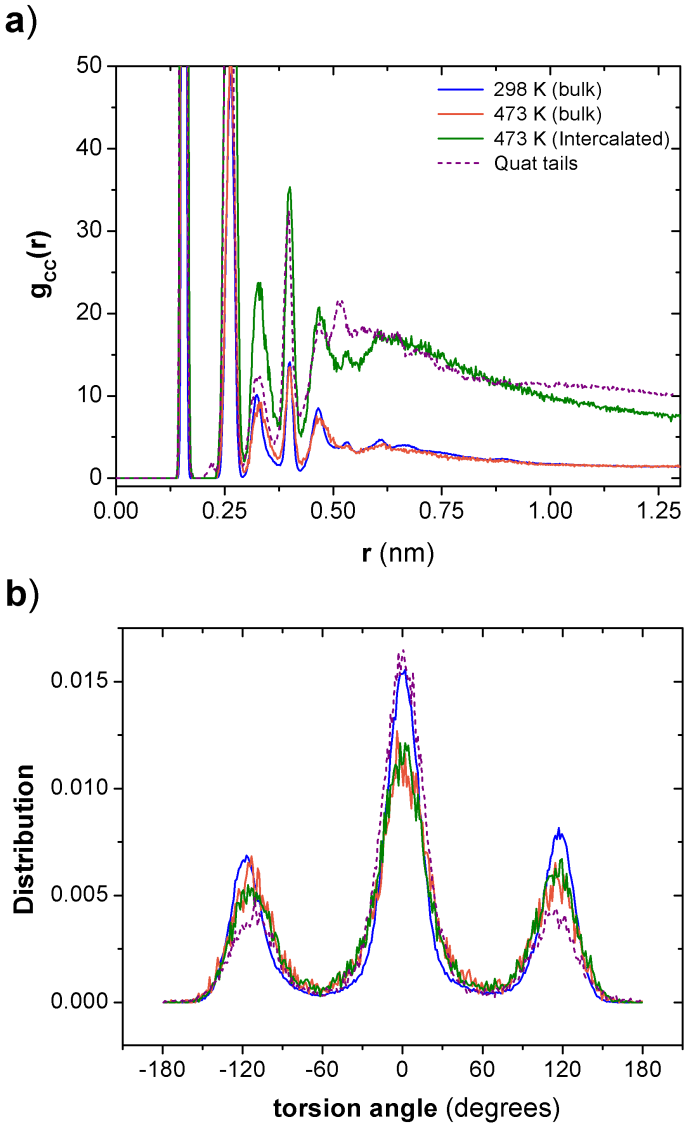

Figure 7.10: a) Radial distribution function between C atoms, and, d) distribution of the torsion angles along the quat tails, of systems simulated at 298 K (continuous line) and 473 K (dashed line).

7.3.1.4 *Energetics of the intermolecular interactions*

Table 7.2 reports the contributions to the binding energy predicted from the isolated binary systems. The favorable energetic contribution provided by $E_{bind}^{PPgMA/MMT}$ demonstrates how important is the presence of a compatibilizer to improve the interactions between PP and the inorganic clay. They are maintained by the strong electrostatic bind resulting from the polar MA monomer and the silicate surface. In addition, the contributions of $E_{bind}^{quat/MMT}$ are in conformity with the structure adopted by the surfactants over the clay (see Fig. 7.6-b). While the electrostatic contribution is mostly related to the head attractions to the layer, the positive van der Waals contribution explains the physisorption and flattening of the quat tails over the clay surface. In turn,

the interaction between PP-g-MA and the quat molecules is less pronounced, weakly dominated by dispersion forces (E_{bind}^{VdW}), but still assuring a favorable thermodynamic environment among the apolar organic species at the interlayer.

Table 7.2: Contributions to the binding energy of the PP-g-MA/quat/MMT system (in kJ/mol) - Van der Waals E_{bind}^{VdW}, Coulombic E_{bind}^{Coul}, and total non-bonded energies E_{bind}^{tot}.

	PP-g-MA/MMT	**quat/MMT**	**PP-g-MA/quat**
E_{bind}^{VdW}	-687.76	288.56	129.32
E_{bind}^{Coul}	46532.79	38474.91	-47.78
E_{bind}^{tot}	45845.05	38766.83	81.54

7.3.2 *Mesoscopic simulations*

7.3.2.1 *Coarse-graining potentials*

Fig. 7.11-a compares the target radial distribution functions with those resulting from the optimized potentials obtained from the IBI protocol. The average errors found after convergence were approximately 0.0056 for P/P, 0.19 for A/A, and 0.02 for P/A. Despite minor deviations, the two sets of curves are similar, meaning that the effective potentials resulting from the optimization are suitable and able to reproduce the structure of the system. The major differences in A/A are due to poor statistics, caused by an insufficient number of A sites in the system. The corresponding initial potentials gathered from the Boltzmann inversion and the effective potentials obtained from IBI are shown in Fig. 7.11-b. The potentials are not identical, but have analogous shapes and barrier heights. The differences exist mostly at the short range, where the potentials are shifted to longer distances in order to correctly reproduce the excluded volume effects of the interactions.

With the aim of obtaining potentials suitable for DPD simulations, the shapes of the non-bonded and bonded potentials were fitted to Eq. 7.5 and Eq. 7.6, respectively. The results are presented in Fig. 7.12. The potentials were deliberately softened via extrapolation, to prevent the existence of high repulsive energies at the short-range. The fitting also smoothes the curves, but without compromising their general features.

The same fitting approach was repeated for the potentials involving the A/M and M/M, based on the results from the Boltzmann inversion. The P/M interactions were set identical to the A/M interaction, with the difference that the attractive section of the potential was discarded, preserving the respulsive section of the potential. The fitting parameters for the non-bonded and bonded potentials are summarized in Table 7.3 and Table 7.4, respectively.

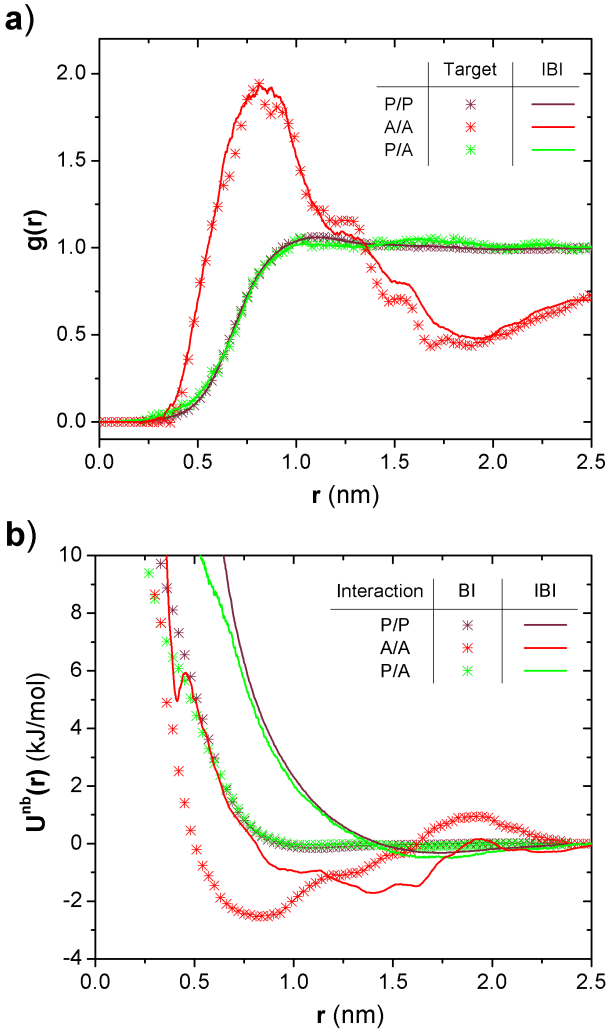

Figure 7.11: a) Radial distribution functions, and, b) effective potentials, obtained before (symbols) and after (lines) the iterative Boltzmann inversion optimization.

7.3.2.2 *DPD simulations of nanocomposites*

The equilibrium morphology of the PLS nanocomposite is to be evaluated by means of DPD simulations. So far, the rationale of the simulation is to verify if the set of non-bonded interactions coherently reproduces the expected systems equilibrium features. Fig. 7.13 provides snapshots of the simulation cell, showing the time evolution of the dispersion of the silicate particles (to facilitate the analysis, the PP molecules were hidden). Starting from a complete exfoliated system, the system evolves to a condition where the clay platelets come closer and start stacking on top of each other. In particular, the formation of a stack of two layers after $1 \cdot 10^6$ steps and the addition of a third layer after $2 \cdot 10^6$ steps are predicted. During this process, the polymer molecules become confined between the MMT layers, thus forming an intercalated structure. Meanwhile, type A particles containing the MA compatibilizer are adsorbed by the clay surfaces. A detailed view of the interlayer

(Fig. 7.14-a) shows PP-g-MA molecules confined between clay sheets and the A type particles being attracted over the surfaces. In addition, the minimum layer distance throughout the simulation (Fig. 7.14-b) reaches an equilibrium value of 4.33 nm, which agrees very well with the atomistic results and with the range of values determined experimentally [254]. Likewise, the averaged distance between the A type particles and the midsection of the layers was predicted to be $1.47^{\pm 0.02}$ nm, which less reproducible but still very close to the atomistic result ($\sim$ 1.34 nm).

7.4 CONCLUSIONS

A multiscale approach, capable of providing an insight into the range of length scales covered by the molecular structure and morphology of PLS nanocomposites, is presented.

Starting from the atomic level, MD simulations using a suitable force field yield accurate predictions of the morphology developed within the silicate stack. At room temperature (i. e., 298 K), a well-defined ordered pseudoquadrilayer, formed by the surfactant tails, is identified. As the temperature increases to 473 K, so does the basal stack distance, as the alkyl tails adopt a greater conformational disorder. Moreover, the analysis of the structure and energetics of a system containing an intercalated PP-g-MA chain between clay sheets confirmed that the existence of a maleic anhydride substitution definitively improves the electrostatic attraction of the polymer to the silicate surface, while dispersion forces are dominant in the interactions of the PP monomers; also, surfactant tails enhance the homogeneous miscibility of the two species at the interlayer.

The parameters necessary to model the system at mesoscopic level were estimated from atomistic simulations following two steps. First, the effective non-bonded potentials between polymer particles were derived from a system in the bulk, where the iterative Boltzmann inversion algorithm was invoked. Second, the interactions between polymer and clay particles were estimated according to the potential of mean force obtained from the non-bonded distribution functions. Furthermore, an initial structure of clay nanoparticles randomly dispersed in a PP+PP-g-MA matrix enclosed in a mesoscopic cell was simulated with the DPD model. During the simulation, the clay platelets began to stack on top of each other maintaining distances similar to the basal spacing obtained for the atomistic simulation. Meanwhile, particles containing the MA substitutions were attracted to the clay surfaces, thus demonstrating that these interactions were correctly reproduced.

It is well known that modeling the large-scale structure of PLS nanocomposites considering the real dimensions of nanoclay layers requires an enormous computational effort. To overcome this, some simplifying assumptions must be considered, while ensuring that the model built is able to provide a reproducible result. The methodology used could provide a step forward into this direction, even if further analyses of its validity are still required.

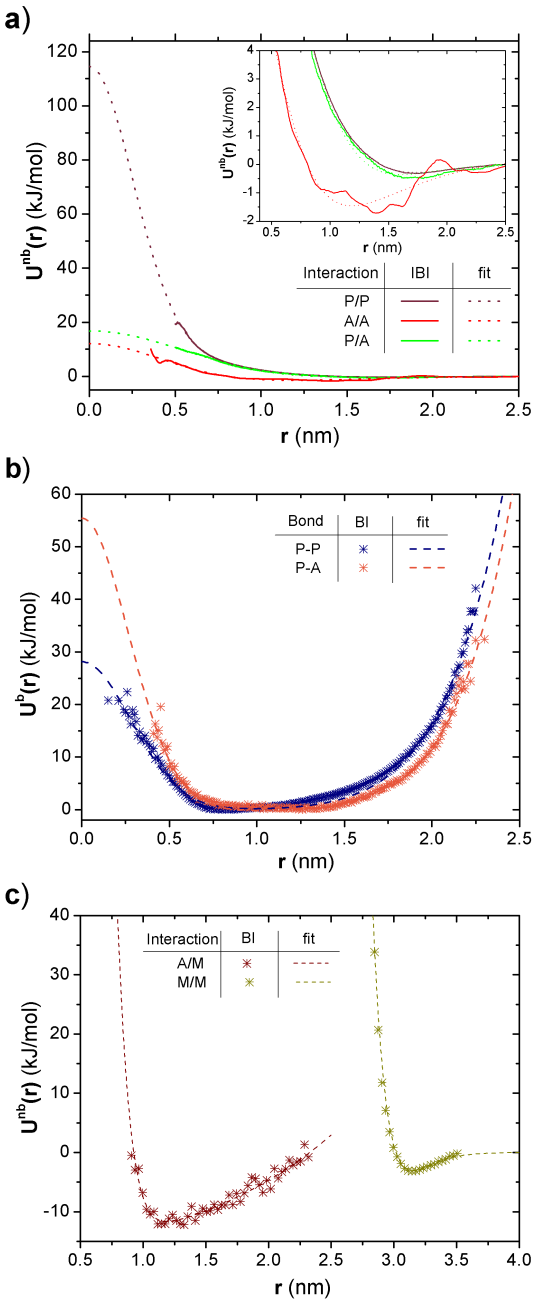

Figure 7.12: Interactions potentials; a) P/P, P/A and A/A non-bonded potentials after IBI (continuous lines) and fittings (dashed lines), b) P-P and P-A bonded potentials from BI (symbols) and fittings (dashed lines), c) A/M and M/M non-bonded potentials from BI (symbols) and fittings (dashed lines).

Table 7.3: Fitting parameters for non-bonded potentials, according to Eq. (7.5) (in kJ/mol).

Non-bonded	P/P	P/A	A/A	P/M	A/M	M/M
β_s	560.0684	185.3516	667.7882	2789.0572	2789.0572	$14.952 \cdot 10^9$
ω_s	2.8611	0.6670	1644.8515	472.4219	472.4219	0.9999
β_i	-547.632	-62.3367	-671.2123	0	-74482.047	$-14.946 \cdot 10^9$
ω_i	2.8302	0.66	1649.8696	0	-2.6169	0.9999
β_l	102.14	-106.2231	15.5383	0	74466.477	0
ω_l	22.1585	0.6253	16354.53	0	-2.6198	0
a	2.0484	0.8983	-94.1167	-10.6749	-10.6749	1.1102

Table 7.4: Fitting parameters for bonded potentials, according to Eq. (7.6) (in kJ/mol).

Bonded	P-P	P-A
b_0	14.059	55.6519
b_1	0.3962	0.3767
b_2	14.0756	-0.2225
b_3	0.3963	4.2186
b_4	0.12731	0.0529
b_5	7.01867	7.8252

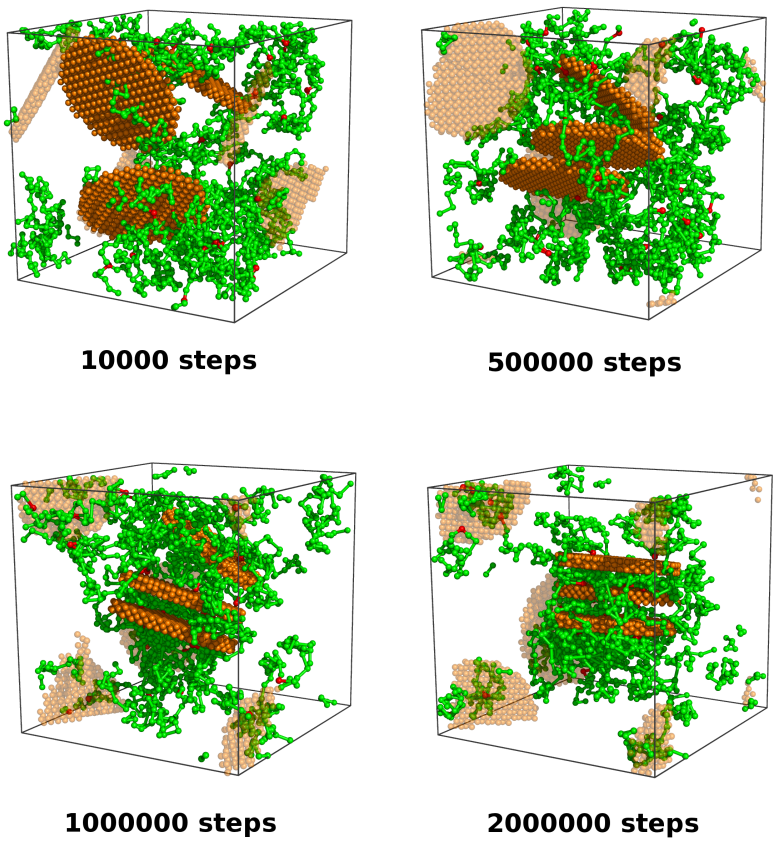

Figure 7.13: Dispersion evolution of the mesoscopic system during equilibrium simulation. PP molecules were hidden, PP-g-MA molecules are represented in green, A type particles are colored red.

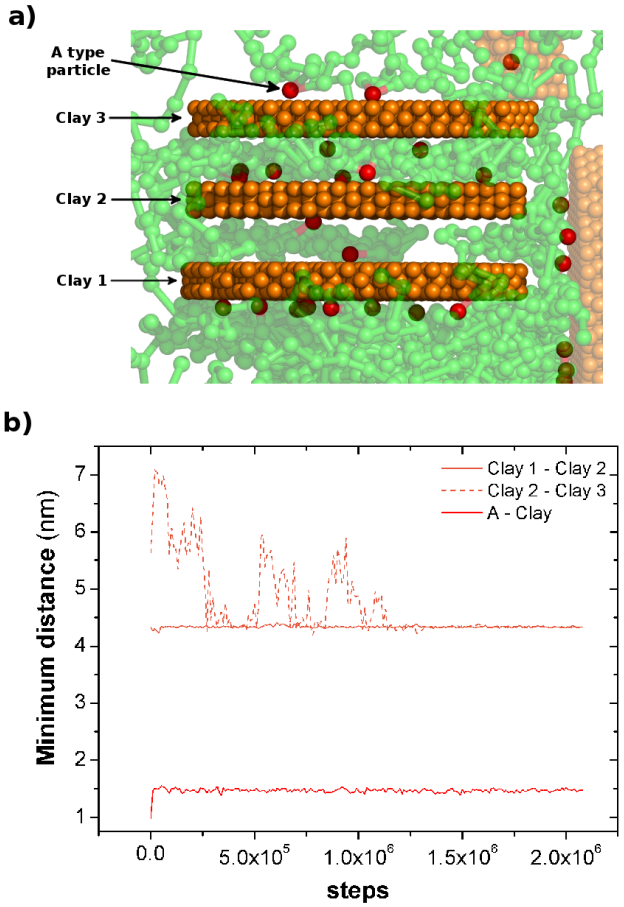

Figure 7.14: a) Detailed view of the silicate stack; b) Minimum distance between silicate layers and A type particles during the simulation.

Part IV

CLOSURE

8

CONCLUDING REMARKS

8.1 GENERAL OVERVIEW

This thesis tackles experimental and computational methodologies to study the behavior of polymeric systems upon processing. The first part is dedicated to the experimental assessment of a new on-line prototype rheometer and to determining whether it is able to detect changes in the rheological properties that are related to morphological changes in PLS nanocomposites during production. The second part presents computational studies involving coarse-graining methodologies to enhance the characteristic length and time scales accessible to predict relevant properties of polymers and, subsequently, of polymer nanocomposites.

The prototype on-line rotational rheometer has the capability of rapidly collecting material samples from within an extruder, at different axial locations, and performing the usual measurements of conventional bench top commercial rheometers. The mechanical and thermal assessment of the instrument included off-line measurements at room and high temperatures and on-line measurements. A good level of confidence on the apparatus was obtained. The instrument was then used to monitor the evolution of the linear viscoelastic behavior of PLS nanocomposites along the axis of a co-rotating twin-screw extruder. Formulations containing compatibilized PP or PA blended with different grades and weight percentages of organophilic montmorillonite were produced at different screw speeds. In all cases, the results from small amplitude oscillatory shear experiments revealed the presence of a non-terminal plateau in G' at the low frequency range, which has been associated with the formation of a network microstructure generated by solid particles resulting from the inter-diffusion of polymer chains between silicate stacks. An increase in nanoclay content broadens the plateau towards higher frequencies and increases the moduli values. The differences related to composition and screw speed were enhanced in formulations comprising PA, which was attributed to the good chemical affinity between the polar matrix and the clay surface combined with the higher shear environment. The conclusions relating the state of dispersion with the rheological properties were in general sustained by XRD data. Moduli values measured along the extruder axis show that most of the dispersion takes place upon melting. Downstream, the moduli could decrease, which was interpreted as evidence of thermal degradation. Subsequently, the on-line rheometer was tested in an industrial environment, where SAOS experiments were performed from sample collected between extruder and die. Again, the good correlation shown by the rheological results with XRD, TEM and SEM data, demonstrates the benefits of using the device for PLS nanocomposite studies.

In contrast with macroscopic simulations (e. g., FEM and FVM), molecular simulations can provide a very detailed insight on the relationships between the physical/chemical characteristics of a material and its properties. Unfortunately, the present practical applicability of these simulations to model industrial processes is virtually non-existent, due to the required computational resources. In this sense, in order to extend the length and time scales accessible by the simulations, efforts have been directed to the development of coarse-graining models. In the open literature, there is a considerable amount of work dealing with coarse-graining simulations of polymers, but little information is given on how the magnitude of coarse-graining affects the accuracy of the local and global behavior of polymer chains. In terms of the DPD model, particles enclose an arbitrary number of monomers with dimensions beyond the Kuhn length. Consequently, the resolution of local subtleties (e. g., fastest mode relaxations) is deteriorated and the scaling laws predicted by the theory are scarcely applicable. An analysis on how the magnitude of coarse-graining affects the equilibrium properties of linear polymer chains was performed. Different molecular weights were tested and the results were quantitatively compared with molecular dynamics simulations and experimental data. The parameters for mesoscopic simulations were empirically obtained from all-atom molecular dynamics simulations, and a time mapping protocol was used to accurately accommodate the systems dynamics to the correct time-scale. A study of the chains global dimensions revealed a good coherence with ideal chain statistics, in part due to the weak excluded volume effects that are present. The dynamic behavior was expressed as a combination of atomistic simulations (fastest mode relaxations) and mesoscopic simulations (slowest mode relaxations), distinguished by a sub-diffusive regime where the dynamics of both models overlap. It is shown that as the coarse-graining level increases, the dynamics deviate from the expected Rouse behavior, since the degrees of freedom describing the faster relaxation modes become absorbed by the mesoscopic particles. Additionally, while increasing the M_w,the dynamics are progressively slowed down until a scaling at the sub-diffusive region of $g_\lambda(t) \sim t^{0.5}$ is verified. The results are coherent with values of the pervaded volume fraction, but in disagreement with theoretical scaling laws. The latter is a consequence of the high coarse-graining levels used, which contributes to a different scaling of the dynamics, in addition to a limitation of the model to provide the correct system compressibility.

Non-equilibrium simulations were also carried out in order to predict rheological properties. One of the important conclusions obtained with these calculations was that the time-mapping function $\delta(\gamma)$ used for the scaling of the dynamical properties also holds for non-equilibrium properties. Since the DPD friction coefficient is itself a parameter contributing to the thermal equilibrium (by means of the fluctuation-dissipation theorem), its magnitude affects the mobility of the particles just as temperature does. In fact, the simulation results indicate that the magnitude of the DPD friction simply shifts the time-scale of the relaxation spectrum without altering its shape, i. e., in the same way as the concept of time-temperature superposition. Although the descrip-

tion given to the time-mapping function is merely empirical, it has proven to be consistent with equilibrium and non-equilibrium properties. Simulations under steady and unsteady shear flow conditions were performed to estimate rheological properties. The scalings obtained in the nonlinear regime were in good agreement with experimental results, even when the coarse-graining level was increased. However, some inaccuracies were detected, mostly related to the unsteady results, where the strain values when stress overshoots follow a trend different from that expected. This is related to a limitation of the model to correctly reproduce pressure. Other reasons accounting for these deviations include the lack of segmental repulsion potentials and the purely soft/repulsive nature of the non-bonded interactions.

In a subsequent step, coarse-graining simulations of PLS nanocomposites were attempted. The ultimate aim is to predict the state of dispersion of such materials when subjected to a certain level and type of hydrodynamic stresses, thus providing information that could support materials design and formulation. A multiscale methodology covering atomistic and mesoscopic scales was proposed. The system chosen included a formulation of PP+PP-g-MA with montmorillonite modified with a quaternary ammonium salt. An analysis of the equilibrium structure of the surfactants inside the clay gallery revealed a well ordered pseudo-quadrilayer morphology, which is in agreement previous experimental works. However, upon increasing the temperature, sections of the surfactant tails were irradiated towards the center of the gallery, adopting more disordered conformations and promoting clay swelling. A system containing an intercalated PP-g-MA chain evidenced the propensity of the MA compatibilizer to diffuse onto the clay surface, demonstrating the importance of the use of a compatibilizer to improve the affinity between the two species. A study regarding the binding energies provided a better understanding of the thermodynamics involved and on their relationship with the structure. The contributions of the coarse-grained free-energies for the mesoscopic system were obtained in a simplified way, by splitting the system in two parts: i) a bulk containing PP and PP-g-MA molecules with their interactions derived from the IBI algorithm through particles enclosing uniquely PP monomers and particles containingthe MA compatibilizer and, ii) a single organophilic MMT layer and a PP-g-MA molecule, where the potential of mean force was used to derive the interactions between particles related to polymer and clay. The potentials were further used in the simulation of a system having a reproducible size to model the state of dispersion of a nanocomposite. The result of the DPD simulation under equilibrium conditions showed astacking of MMT layers and the strong affinity of the MA particle to be adsorbed onto the silicate surfaces. Additionally, the predicted values of basal spacing were in agreement with MD results and in the same range of the values given by experiments. Although research in the field is ongoing, the methodology proposed is a promising starting point to further developments and improvements for the multiscale modelling of these materials.

8.2 FUTURE RESEARCH DIRECTIONS

Upon reaching the current development at the experimental, theoretical and computational levels, multiple appealing research topics have inevitably revealed their importance. A few of the most important research directions could be:

On-line rheometry

- Study of nanocomposites containing other kinds of nanoparticle species (e. g., carbon nanotubes, titanium dioxide, cellulose nanowhiskers).
- Detailed studies combining different on-line (e. g., rheometry, NIR) and conventional (e. g., XRD, NMR, TEM) techniques to unveil the dispersion mechanisms of nanocomposites.
- Extended studies towards the optimization of material formulations and processing conditions.

Computational modelling

- Employ/implement more refined algorithms to effectively derive a better description of the free-energy contributions between polymer and silicate layers, and the latter with themselves.
- During coarse-graining, some important subtleties of the system are relaxed and are not properly described at the mesoscopic scale. Hence, it is desirable to recover some of the features of the underlying structure by means of *reverse mapping* protocols.
- So far, the nanocomposite structure at the mesoscopic level was evaluated in term of equilibrium simulation. Non-equilibrium simulations are indispensable for accessing the mechanisms of dispersion involved, the state of dispersion, and their dependence on the magnitude of the external flow field.
- Experimental validation of the simulations are necessary. Specifically, comparison between the simulated distribution of nanoparticles in the matrix with results obtained from TEM and XRD analysis, and the coherence of the relationships between structure and rheological properties should be analyzed.
- Extend the multiscale procedure to other formulations and nanocomposite systems.

BIBLIOGRAPHY

[1] V. A. Harmandaris, V. G. Mavrantzas, D. N. Theodorou, M. Kröger, J. Ramírez, H. C. Öttinger, and D. Vlassopoulos. Crossover from the rouse to the entangled polymer melt regime: Signals from long, detailed atomistic molecular dynamics simulations, supported by rheological experiments. *Macromolecules*, 36(4):1376–1387, 2003.

[2] J. T. Padding and W. J. Briels. Time and length scales of polymer melts studied by coarse-grained molecular dynamics simulations. *The Journal of Chemical Physics*, 117(2):925–943, 2002.

[3] M. Zamponi, A. Wischnewski, M. Monkenbusch, L. Willner, D. Richter, P. Falus, B. Farago, and M. G. Guenza. Cooperative dynamics in homopolymer melts: A comparison of theoretical predictions with neutron spin echo experiments. *The Journal of Physical Chemistry B*, 112 (50):16220–16229, 2008.

[4] D. Richter, L. Willner, A. Zirkel, B. Farago, L. J. Fetters, and J. S. Huang. Onset of topological constraints in polymer melts: A mode analysis by neutron spin echo spectroscopy. *Phys. Rev. Lett.*, 71:4158–4161, Dec 1993.

[5] D. Pearson, E. Herbolzheimer, N. Grizzuti, and G. Marrucci. Transient behavior of entangled polymers at high shear rates. *Journal of Polymer Science Part B: Polymer Physics*, 29(13):1589–1597, 1991.

[6] K. Osaki, T. Inoue, and T. Uematsu. Stress overshoot of polymer solutions at high rates of shear: semidilute polystyrene solutions with and without chain entanglement. *Journal of Polymer Science Part B: Polymer Physics*, 38(24):3271–3276, 2000.

[7] José A. Covas, Olga S. Carneiro, João M. Maia, Susana A. Filipe, and Ana V. Machado. Evolution of chemistry, morphology and rheology of various polymer systems along a twin-screw extruder. *The Canadian Journal of Chemical Engineering*, 80(6):1065–1074, 2002.

[8] A. V. Machado, J. M. Maia, S. V. Canevarolo, and J. A. Covas. Evolution of peroxide-induced thermomechanical degradation of polypropylene along the extruder. *Journal of Applied Polymer Science*, 91(4):2711–2720, 2004.

[9] W. Lertwimolnun and B. Vergnes. Influence of compatibilizer and processing conditions on the dispersion of nanoclay in a polypropylene matrix. *Polymer*, 46(10):3462 – 3471, 2005.

[10] J.A. Covas, J.M. Maia, A.V. Machado, and P. Costa. On-line rotational rheometry for extrusion and compounding operations. *Journal of Non-Newtonian Fluid Mechanics*, 148(1-3):88 – 96, 2008.

[11] A.A. Collyer. *Techniques in Rheological Measurement.* Chapman & Hall, 1993. ISBN 9780412534904.

[12] Halit S. Gokturk and Dilhan M. Kalyon. Adjustable gap rheometer, 1 1994.

[13] Nihan Dogan, Michael J McCarthy, and Robert L Powell. Measurement of polymer melt rheology using ultrasonics-based in-line rheometry. *Measurement Science and Technology*, 16(8):1684, 2005.

[14] Johan Wiklund and Mats Stading. Application of in-line ultrasound doppler-based UVP-PD rheometry method to concentrated model and industrial suspensions. *Flow Measurement and Instrumentation*, 19(3-4): 171 – 179, 2008.

[15] R.S. Smith and J.A. Glasscock. Measurements of the rheological properties of standard reference material 2490 using an in-line micro-fourier rheometer. *Korea-Australia Rheology Journal*, 16(4):169–173, 2004.

[16] D.G. Baird, T.W. Chan, C. McGrady, and S.M. Mazahir. Evaluation of the use of a semi-hyperbolic die for measuring elongational viscosity of polymer melts. *Applied Rheology*, 20:34900, 2010.

[17] HAAKE ProFlow. Thermo Electron Corporation. http://www.thermo.com/eThermo/CMA/PDFs/Product/productPDF_18544.pdf.

[18] Göttfert process rheometers. Göettfert. http://www.goettfert.com.

[19] Viscosensor. Dynisco. http://www.dynisco.com/online-rheometer-;viscosensor-.

[20] V. Zschuppe, T. Geilen, J.M. Maia, J.A. Covas, and H.-M. Petri. Rheology application note lr-57, 2006.

[21] J.A Covas, J M. Nóbrega, and J M. Maia. Rheological measurements along an extruder with an on-line capillary rheometer. *Polymer Testing*, 19(2):165 – 176, 2000.

[22] O.S. Carneiro, A. Poulesquen, J.A. Covas, and B. Vergnes. Visualisation and analysis of the flow along the kneading block of a twin-screw extruder. *International Polymer Processing*, 4:301 – 308, 2002.

[23] K. Kohlgrüber and M. Bierdel. *Co-rotating Twin-screw Extruders: Fundamentals, Technology, and Applications.* Hanser Gardner Publications, 2008.

[24] O.S. Carneiro, J.A. Covas, J.A. Ferreira, and M.F. Cerqueira. On-line monitoring of the residence time distribution along a kneading block of a twin-screw extruder. *Polymer Testing*, 23(8):925 – 937, 2004.

[25] H.M. Laun and H. MÃŒnstedt. Elongational behaviour of a low density polyethylene melt. *Rheologica Acta*, 17(4):415–425, 1978.

[26] J. Meissner. Basic parameters, melt rheology, processing and end-use properties of three similar low density polyethylene samples. *Pure and Applied Chemistry*, 42(4):551–612, 1975.

[27] S. Al-Malaika. *Reactive Modifiers for Polymers*. Springer, 1997. ISBN 9780751402650.

[28] M. Xanthos. *Reactive Extrusion: Principles and Practice*. Polymer Processing Institute Series. Hanser Publishers, 1992. ISBN 9781569901137.

[29] A.V Machado, J.A Covas, and M van Duin. Effect of polyolefin structrure on maleic anhydride grafting. *Polymer*, 42(8):3649 – 3655, 2001.

[30] Michael J. Solomon, Abdulwahab S. Almusallam, Kurt F. Seefeldt, Anongnat Somwangthanaroj, and Priya Varadan. Rheology of polypropylene/clay hybrid materials. *Macromolecules*, 34(6):1864–1872, 2001.

[31] Ph. Cassagnau. Melt rheology of organoclay and fumed silica nanocomposites. *Polymer*, 49(9):2183 – 2196, 2008.

[32] Suprakas Sinha Ray and Mosto Bousmina. Biodegradable polymers and their layered silicate nanocomposites: In greening the 21st century materials world. *Progress in Materials Science*, 50(8):962 – 1079, 2005.

[33] Suprakas Sinha Ray and Masami Okamoto. Polymer/layered silicate nanocomposites: a review from preparation to processing. *Progress in Polymer Science*, 28(11):1539 – 1641, 2003.

[34] Emmanuel P. Giannelis. Polymer-layered silicate nanocomposites: Synthesis, properties and applications. *Applied Organometallic Chemistry*, 12(10-11):675–680, 1998.

[35] Michael Alexandre and Philippe Dubois. Polymer-layered silicate nanocomposites: preparation, properties and uses of a new class of materials. *Materials Science and Engineering: R: Reports*, 28(1-2):1 – 63, 2000.

[36] Hartmut Fischer. Polymer nanocomposites: from fundamental research to specific applications. *Materials Science and Engineering: C*, 23(6-8): 763 – 772, 2003.

[37] Suprakas Sinha Ray and Masami Okamoto. Polymer/layered silicate nanocomposites: a review from preparation to processing. *Progress in Polymer Science*, 28(11):1539 – 1641, 2003.

[38] O. Breuer and Uttandaraman Sundararaj. Big returns from small fibers: A review of polymer/carbon nanotube composites. *Polymer Composites*, 25(6):630–645, 2004.

[39] Farzana Hussain, Mehdi Hojjati, Masami Okamoto, and Russell E. Gorga. Review article: Polymer-matrix nanocomposites, processing, manufacturing, and application: An overview. *Journal of Composite Materials*, 40(17):1511–1575, 2006.

[40] Jonathan N. Coleman, Umar Khan, Werner J. Blau, and Yurii K. Gun´ko. Small but strong: A review of the mechanical properties of carbon nanotube-polymer composites. *Carbon*, 44(9):1624 – 1652, 2006.

[41] Kin tak Lau, Chong Gu, and David Hui. A critical review on nanotube and nanotube/nanoclay related polymer composite materials. *Composites Part B: Engineering*, 37(6):425 – 436, 2006.

[42] A W K Ma, K M Yearsley, F Chinesta, and M R Mackley. A review of the microstructure and rheology of carbon nanotube suspensions. *Proceedings of the Institution of Mechanical Engineers, Part N: Journal of Nanoengineering and Nanosystems*, 222(3):71–94, 2008.

[43] D.R. Paul and L.M. Robeson. Polymer nanotechnology: Nanocomposites. *Polymer*, 49(15):3187 – 3204, 2008.

[44] Lucilene Betega de Paiva, Ana Rita Morales, and Francisco R. Valenzuela Díaz. Organoclays: Properties, preparation and applications. *Applied Clay Science*, 42(1-2):8 – 24, 2008.

[45] S. Pavlidou and C.D. Papaspyrides. A review on polymer-layered silicate nanocomposites. *Progress in Polymer Science*, 33(12):1119 – 1198, 2008.

[46] Zdenko Spitalsky, Dimitrios Tasis, Konstantinos Papagelis, and Costas Galiotis. Carbon nanotube-polymer composites: Chemistry, processing, mechanical and electrical properties. *Progress in Polymer Science*, 35(3): 357 – 401, 2010.

[47] J. Jancar, J.F. Douglas, F.W. Starr, S.K. Kumar, P. Cassagnau, A.J. Lesser, S.S. Sternstein, and M.J. Buehler. Current issues in research on structure-property relationships in polymer nanocomposites. *Polymer*, 51(15):3321 – 3343, 2010.

[48] T. MacNally and P.P. Otschke. *Polymer Carbon Nanotube Composites: Preparation, Properties and Applications*. Woodhead Publishing Series in Composites Science and Engineering Series. Woodhead Publishing Limited, 2011.

[49] Yu Dong and Debes Bhattacharyya. Effects of clay type, clay/compatibiliser content and matrix viscosity on the mechanical properties of polypropylene/organoclay nanocomposites. *Composites Part A: Applied Science and Manufacturing*, 39(7):1177 – 1191, 2008.

[50] Youngjae Yoo and D.R. Paul. Effect of organoclay structure on morphology and properties of nanocomposites based on an amorphous polyamide. *Polymer*, 49(17):3795 – 3804, 2008.

[51] W. Lertwimolnun and B. Vergnes. Effect of processing conditions on the formation of polypropylene/organoclay nanocomposites in a twin screw extruder. *Polymer Engineering & Science*, 46(3):314–323, 2006.

[52] Gaurav R. Kasaliwal, Sven Pegel, Andreas Göldel, Petra Pötschke, and Gert Heinrich. Analysis of agglomerate dispersion mechanisms of multiwalled carbon nanotubes during melt mixing in polycarbonate. *Polymer*, 51(12):2708 – 2720, 2010.

[53] R. Haggenmueller, H.H. Gommans, A.G. Rinzler, J.E. Fischer, and K.I. Winey. Aligned single-wall carbon nanotubes in composites by melt processing methods. *Chemical Physics Letters*, 330(3-4):219 – 225, 2000.

[54] H.R. Dennis, D.L. Hunter, D. Chang, S. Kim, J.L. White, J.W. Cho, and D.R. Paul. Effect of melt processing conditions on the extent of exfoliation in organoclay-based nanocomposites. *Polymer*, 42(23):9513 – 9522, 2001.

[55] W. Rodgers, F. Lortie, R. Ottaviani, P. Fasulo, M. Dolgovskij, and C. Macosko. Effect of mixer type on exfoliation of polypropylene nanocomposites. *SPE ANTEC Techninal Papers*, pages 2255 – 2259, 2003.

[56] Hua Wang, Changchun Zeng, Mark Elkovitch, L. James Lee, and Kurt W. Koelling. Processing and properties of polymeric nano-composites. *Polymer Engineering & Science*, 41(11):2036–2046, 2001.

[57] W. Lertwimolnun and B. Vergnes. Influence of screw profile and extrusion conditions on the microstructure of polypropylene/organoclay nanocomposites. *Polymer Engineering & Science*, 47(12):2100–2109, 2007.

[58] J. A. Covas, M. F. Almeida, A. V. Machado, N. M. Larocca, and L. A. Pessan. Nanoclays dispersion in a PA6/PP blend by twin screw compounding. *Macromolecular Symposia*, 301(1):55–62, 2011.

[59] Y. Y. Huang, S. V. Ahir, and E. M. Terentjev. Dispersion rheology of carbon nanotubes in a polymer matrix. *Phys. Rev. B*, 73:125422, Mar 2006.

[60] J. Vermant, S. Ceccia, M. K. Dolgovskij, P. L. Maffettone, and C. W. Macosko. Quantifying dispersion of layered nanocomposites via melt rheology. *Journal of Rheology*, 51(3):429–450, 2007.

[61] Su-Dong Park, Dong-Hee Han, Dayong Teng, and Younghwan Kwon. Rheological properties and dispersion of multi-walled carbon nanotube (MWCNT) in polystyrene matrix. *Current Applied Physics*, 8(3-4):482 – 485, 2008.

[62] B. Vergnes. The use of apparent yield stress to characterize exfoliation in polymer nanocomposites. *International Polymer Processing*, 26:229 – 232, 2011.

[63] Sven Pegel, Petra Pötschke, Gudrun Petzold, Ingo Alig, Sergej M. Dudkin, and Dirk Lellinger. Dispersion, agglomeration, and network formation of multiwalled carbon nanotubes in polycarbonate melts. *Polymer*, 49(4):974 – 984, 2008.

[64] S. Jamali. Effect of Thermomechanical History on the Final Properties of CNT Composites. Master's thesis, EURHEO Erasmus Mundus Master Thesis, University of Minho, Guimarães, Portugal, 2010.

[65] Seung Hwan Lee, EunNaRi Cho, and Jae Ryoun Youn. Rheological behavior of polypropylene/layered silicate nanocomposites prepared by melt compounding in shear and elongational flows. *Journal of Applied Polymer Science*, 103(6):3506–3515, 2007.

[66] I. Manas-Zloczower. *Mixing and Compounding of Polymers: Theory and Practice*, chapter Chapter 4: Dispersive Mixing of Solid Additives. Hanser Publishers, Munich, 2009.

[67] N. Domingues, M. Camesasca, M. Kaufman, I. Manas-Zloczower, A. Gaspar-Cunha, and J.A. Covas. Modeling of agglomerate dispersion in single screw extruders. *International Polymer Processing*, 25:251 – 257, 2011.

[68] S. Mould, J. Barbas, A.V. Machado, J.M. Nóbrega, and J.A. Covas. Measuring the rheological properties of polymer melts with on-line rotational rheometry. *Polymer Testing*, 30(6):602 – 610, 2011.

[69] L. A. Utracki. *Clay-containing polymeric nanocomposites, 2 Vols.* Smithers Rapra Publishing, Shawbury, Shrewsbury, UK, 2004.

[70] Akane Okada and Arimitsu Usuki. Twenty years of polymer-clay nanocomposites. *Macromolecular Materials and Engineering*, 291(12): 1449–1476, 2006.

[71] Z-Z Yu, Dasari A., and Y-W Mai. *Processing and properties of nanocomposites*, chapter 7: Polymer-clay nanocomposites: a review of mechanical and physical properties. World Sci Pub, 2006.

[72] Biqiong Chen, Julian R. G. Evans, H. Christopher Greenwell, Pascal Boulet, Peter V. Coveney, Allen A. Bowden, and Andrew Whiting. A critical appraisal of polymer-clay nanocomposites. *Chem. Soc. Rev.*, 37: 568–594, 2008.

[73] A. Esfandiari, H Nazokdast, R. A. Rashidi, and M-E Yazdansgenas. Review of polymer-organoclay nanocomposites. *Journal of Applied Sciences*, 8(3):545–561, 2008.

[74] Jinguo Zhang, E. Manias, and Charles A. Wilkie. Polymerically modified layered silicates: An effective route to nanocomposites. *Journal of Nanoscience and Nanotechnology*, 8(4):1597–1615, 2008.

[75] Biqiong Chen and Julian R. G. Evans. Impact strength of polymer-clay nanocomposites. *Soft Matter*, 5:3572–3584, 2009.

[76] G. Choudalakis and A.D. Gotsis. Permeability of polymer/clay nanocomposites: A review. *European Polymer Journal*, 45(4):967 – 984, 2009.

[77] Vikas Mittal. Polymer layered silicate nanocomposites: A review. *Materials*, 2(3):992–1057, 2009.

[78] Hurang Hu, Landon Onyebueke, and Ayo Abatan. Characterizing and modeling mechanical properties of nanocomposites - review and evaluation. *Journal of Minerals & Material Characterization & Engineering*, 9(4):275–319, 2010.

[79] In-Yup Jeon and Jong-Beom Baek. Nanocomposites derived from polymers and inorganic nanoparticles. *Materials*, 3(6):3654–3674, 2010.

[80] P. Kiliaris and C.D. Papaspyrides. Polymer/layered silicate (clay) nanocomposites: An overview of flame retardancy. *Progress in Polymer Science*, 35(7):902 – 958, 2010.

[81] Shanghua Li, Meng Meng Lin, Muhammet S. Toprak, Do Kyung Kim, and Mamoun Muhammed. Nanocomposites of polymer and inorganic nanoparticles for optical and magnetic applications. *Nano Reviews*, 1: 5214, 2010.

[82] Makoto Kato, Usuki Arimitsu, Naoki Hasegawa, Hirotaka Okamoto, and Masaya Kawasumi. Development and applications of polyolefin- and rubber-clay nanocomposites. *Polymer Journal*, 43:583–593, 2011.

[83] Suprakas Sinha Ray, Kazunobu Yamada, Masami Okamoto, and Kazue Ueda. Polylactide-layered silicate nanocomposite: A novel biodegradable material. *Nano Letters*, 2(10):1093–1096, 2002.

[84] Mosto Bousmina. Study of intercalation and exfoliation processes in polymer nanocomposites. *Macromolecules*, 39(12):4259–4263, 2006.

[85] Cher H. Davis, Lon J. Mathias, Jeffrey W. Gilman, David A. Schiraldi, J. Randy Shields, Paul Trulove, Tom E. Sutto, and Hugh C. Delong. Effects of melt-processing conditions on the quality of poly(ethylene terephthalate) montmorillonite clay nanocomposites. *Journal of Polymer Science Part B: Polymer Physics*, 40(23):2661–2666, 2002.

[86] Paula D. Fasulo, William R. Rodgers, Robert A. Ottaviani, and Douglas L. Hunter. Extrusion processing of tpo nanocomposites. *Polymer Engineering & Science*, 44(6):1036–1045, 2004.

[87] Linjie Zhu and M. Xanthos. Effects of process conditions and mixing protocols on structure of extruded polypropylene nanocomposites. *Journal of Applied Polymer Science*, 93(4):1891–1899, 2004.

[88] M. Modesti, A. Lorenzetti, D. Bon, and S. Besco. Effect of processing conditions on morphology and mechanical properties of compatibilized polypropylene nanocomposites. *Polymer*, 46(23):10237 – 10245, 2005.

[89] Piia Peltola, Elina Välipakka, Jyrki Vuorinen, Seppo Syrjälä, and Kalle Hanhi. Effect of rotational speed of twin screw extruder on the microstructure and rheological and mechanical properties of nanoclay-reinforced polypropylene nanocomposites. *Polymer Engineering & Science*, 46(8):995–1000, 2006.

[90] Luigi Scattela, Paola Scarfato, and Domenico Acierno. Processing, rheology and structure of melt compounded pbtclay nanocomposites having different chemical composition. *e-Polymers*, 6(1):295–309, 2013.

[91] Rhutesh K. Shah and D.R. Paul. Organoclay degradation in melt processed polyethylene nanocomposites. *Polymer*, 47(11):4075 – 4084, 2006.

[92] Mark A. Treece, Wei Zhang, Ronald D. Moffitt, and James P. Oberhauser. Twin-screw extrusion of polypropylene-clay nanocomposites: Influence of masterbatch processing, screw rotation mode, and sequence. *Polymer Engineering & Science*, 47(6):898–911, 2007.

[93] T. Domenech, E. Peuvrel-Disdier, and B. Vergnes. Influence of twin-screw processing conditions on structure and properties of polypropylene-organoclay nanocomposites. *International Polymer Processing*, XXVII:517–526, 2012.

[94] A. L. F. de M. Giraldi, M. T. M. Bizarria, A. A. Silva, J. I. Velasco, Marcos A. d'Ávila, and L. H. I. Mei. Effects of extrusion conditions on the properties of recycled poly(ethylene terephthalate)/nanoclay nanocomposites prepared by a twin-screw extruder. *Journal of Applied Polymer Science*, 108(4):2252–2259, 2008.

[95] Anthony J. Bur, Yu-Hsin Lee, Steven C. Roth, and Paul R. Start. Measuring the extent of exfoliation in polymer/clay nanocomposites using real-time process monitoring methods. *Polymer*, 46(24):10908 – 10918, 2005.

[96] Marcelo K. Bertolino and SebastiÃ£o V. Canevarolo. Preparation of extruded melt-mixed polypropylene/montmorillonite nanocomposites with inline monitoring. *Polymer Engineering & Science*, 50(3):440–445, 2010.

[97] Paul H. Maupin, Jeffrey W. Gilman, Richard H. Harris, Severine Bellayer, Anthony J. Bur, Steven C. Roth, Marius Murariu, Alexander B. Morgan, and Joseph D. Harris. Optical probes for monitoring intercalation and exfoliation in melt-processed polymer nanocomposites. *Macromolecular Rapid Communications*, 25(7):788–792, 2004.

[98] Anthony J. Bur, Steven C. Roth, Paul R. Start, Yu-Hsin Lee, and Paul H. Maupin. Monitoring clay exfoliation during polymer/clay compounding using fluorescence spectroscopy. *Transactions of the Institute of Measurement and Control*, 29(5):403–416, 2007.

[99] Andreas Witschnigg, Stephan Laske, Milan Kracalik, Michael Feuchter, Gerald Pinter, Günther Maier, Wolfgang Märzinger, Michael Haberkorn, Günter Rüdiger Langecker, and Clemens Holzer. In-line characterization of polypropylene nanocomposites using FT-NIR. *Journal of Applied Polymer Science*, 117(5):3047–3053, 2010.

[100] Joana M. Barbas, Ana V. Machado, and José A. Covas. In-line near-infrared spectroscopy: A tool to monitor the preparation of polymer-clay nanocomposites in extruders. *Journal of Applied Polymer Science*, 127(6):4899–4909, 2013.

[101] Yu-Hsin Lee, Anthony J. Bur, Steven C. Roth, Paul R. Start, and Richard H. Harris. Monitoring the relaxation behavior of nylon/clay nanocomposites in the melt with an online dielectric sensor. *Polymers for Advanced Technologies*, 16(2-3):249–256, 2005.

[102] Milan Kracalik, Stephan Laske, Andreas Witschnigg, and Clemens Holzer. Elongational and shear flow in polymer-clay nanocomposites measured by on-line extensional and off-line shear rheometry. *Rheologica Acta*, 50(11-12):937–944, 2011.

[103] Ramanan Krishnamoorti and Emmanuel P. Giannelis. Rheology of end-tethered polymer layered silicate nanocomposites. *Macromolecules*, 30 (14):4097–4102, 1997.

[104] Alexandre Vermogen, Karine Masenelli-Varlot, Roland Séguéla, Jannick Duchet-Rumeau, Sylvain Boucard, and Patrick Prele. Evaluation of the structure and dispersion in polymer-layered silicate nanocomposites. *Macromolecules*, 38(23):9661–9669, 2005.

[105] Ali Durmus, Ahmet Kasgoz, and Christopher W. Macosko. Linear low density polyethylene (lldpe)/clay nanocomposites. part i: Structural characterization and quantifying clay dispersion by meltÂ rheology. *Polymer*, 48(15):4492 – 4502, 2007.

[106] Liang Xu, Hiroyoshi Nakajima, Evangelos Manias, and Ramanan Krishnamoorti. Tailored nanocomposites of polypropylene with layered silicates. *Macromolecules*, 42(11):3795–3803, 2009.

[107] S. T. Mould, J. M. Barbas, A. V. Machado, J. M. Nóbrega, and J. A. Covas. Monitoring the production of polymer nanocomposites by melt compounding with on-line rheometry. *International Polymer Processing*, XXVII(5):527–534, 2012.

[108] J.M. Barbas, A.V. Machado, and J.A. Covas. Evolution of dispersion along the extruder during the manufacture of polymer-organoclay nanocomposites. *Chemical Engineering Science*, 98(0):77 – 87, 2013.

[109] Kurt Kremer and Gary S. Grest. Dynamics of entangled linear polymer melts: A molecular-dynamics simulation. *The Journal of Chemical Physics*, 92(8):5057–5086, 1990.

[110] F. Ercolessi and J. B. Adams. Interatomic potentials from first-principles calculations: The force-matching method. *EPL (Europhysics Letters)*, 26 (8):583, 1994.

[111] Alexander P. Lyubartsev and Aatto Laaksonen. Calculation of effective interaction potentials from radial distribution functions: A reverse monte carlo approach. *Phys. Rev. E*, 52:3730–3737, Oct 1995.

[112] Dirk Reith, Mathias Pütz, and Florian Müller-Plathe. Deriving effective mesoscale potentials from atomistic simulations. *Journal of Computational Chemistry*, 24(13):1624–1636, 2003.

[113] Sergei Izvekov and Gregory A. Voth. Multiscale coarse graining of liquid-state systems. *The Journal of Chemical Physics*, 123(13):134105, 2005.

[114] Siewert J. Marrink, H. Jelger Risselada, Serge Yefimov, D. Peter Tieleman, and Alex H. de Vries. The MARTINI force field: Coarse grained model for biomolecular simulations. *The Journal of Physical Chemistry B*, 111(27):7812–7824, 2007.

[115] M. Doi and S.F. Edwards. *The Theory of Polymer Dynamics*. International Series of Monographs on Physics. Clarendon Press, 1988.

[116] P.J. Flory. *Principles of Polymer Chemistry: Paul J. Flory*. The George Fisher Baker Non-Resident Lectureship in Chemistry At Cornell University. Cornell University, 1953.

[117] Steve O. Nielsen, Carlos F. Lopez, Goundla Srinivas, and Michael L. Klein. A coarse grain model for n-alkanes parameterized from surface tension data. *The Journal of Chemical Physics*, 119(14):7043–7049, 2003.

[118] Roland Faller and Florian MÃŒller-Plathe. Modeling of poly(isoprene) melts on different scales. *Polymer*, 43(2):621 – 628, 2002.

[119] Praveen K. Depa and Janna K. Maranas. Dynamic evolution in coarse-grained molecular dynamics simulations of polyethylene melts. *The Journal of Chemical Physics*, 126(5):054903, 2007.

[120] Hwankyu Lee, Alex H. de Vries, Siewert-Jan Marrink, and Richard W. Pastor. A coarse-grained model for polyethylene oxide and polyethylene glycol: Conformation and hydrodynamics. *The Journal of Physical Chemistry B*, 113(40):13186–13194, 2009. PMID: 19754083.

[121] Theodora Spyriouni, Christos Tzoumanekas, Doros Theodorou, Florian Müller-Plathe, and Giuseppe Milano. Coarse-grained and reverse-mapped united-atom simulations of long-chain atactic polystyrene melts: Structure, thermodynamic properties, chain conformation, and entanglements. *Macromolecules*, 40(10):3876–3885, 2007.

[122] Vagelis A. Harmandaris and Kurt Kremer. Dynamics of polystyrene melts through hierarchical multiscale simulations. *Macromolecules*, 42 (3):791–802, 2009.

[123] Dominik Fritz, Konstantin Koschke, Vagelis A. Harmandaris, Nico F. A. van der Vegt, and Kurt Kremer. Multiscale modeling of soft matter: scaling of dynamics. *Phys. Chem. Chem. Phys.*, 13:10412–10420, 2011.

[124] W. Tschöp, K. Kremer, J. Batoulis, T. Bürger, and O. Hahn. Simulation of polymer melts. i. coarse-graining procedure for polycarbonates. *Acta Polymerica*, 49(2-3):61–74, 1998.

[125] S. León, N. van der Vegt, L. Delle Site, and K. Kremer. Bisphenol a polycarbonate: Entanglement analysis from coarse-grained md simulations. *Macromolecules*, 38(19):8078–8092, 2005.

[126] Kazunori Kamio, Krzysztof Moorthi, and Doros N. Theodorou. Coarse grained end bridging monte carlo simulations of poly(ethylene terephthalate) melt. *Macromolecules*, 40(3):710–722, 2007.

[127] Giulia Rossi, Ian G. Elliott, Tapio Ala-Nissila, and Roland Faller. Molecular dynamics study of a MARTINI coarse-grained polystyrene brush in good solvent: Structure and dynamics. *Macromolecules*, 45(1):563–571, 2012. doi: 10.1021/ma201980k.

[128] Hwankyu Lee and Ronald G. Larson. Coarse-grained molecular dynamics studies of the concentration and size dependence of fifth- and seventh-generation pamam dendrimers on pore formation in dmpc bilayer. *The Journal of Physical Chemistry B*, 112(26):7778–7784, 2008. PMID: 18543869.

[129] Robert Zwanzig. Memory effects in irreversible thermodynamics. *Phys. Rev.*, 124:983–992, Nov 1961.

[130] Hazime Mori. Transport, collective motion, and brownian motion. *Progress of Theoretical Physics*, 33(3):423–455, 1965.

[131] Tomoyuki Kinjo and Shi-aki Hyodo. Equation of motion for coarse-grained simulation based on microscopic description. *Phys. Rev. E*, 75: 051109, May 2007.

[132] J. T. Padding and W. J. Briels. Uncrossability constraints in mesoscopic polymer melt simulations: Non-rouse behavior of C_{120} H_{242}. *The Journal of Chemical Physics*, 115(6):2846–2859, 2001.

[133] X. Guerrault, B. Rousseau, and J. Farago. Dissipative particle dynamics simulations of polymer melts. i. building potential of mean force for polyethylene and cis-polybutadiene. *The Journal of Chemical Physics*, 121(13):6538–6546, 2004.

[134] F. Lahmar, C. Tzoumanekas, D. N. Theodorou, and B. Rousseau. Onset of entanglements revisited. dynamical analysis. *Macromolecules*, 42(19): 7485–7494, 2009.

[135] R. Perez-Aparicio, J. Colmenero, F. Alvarez, J. T. Padding, and W. J. Briels. Chain dynamics of poly(ethylene-alt-propylene) melts by means of coarse-grained simulations based on atomistic molecular dynamics. *The Journal of Chemical Physics*, 132(2):024904, 2010.

[136] P. J. Hoogerbrugge and J. M. V. A. Koelman. Simulating microscopic hydrodynamic phenomena with dissipative particle dynamics. *EPL (Europhysics Letters)*, 19(3):155, 1992.

[137] P. Kindt and W. J. Briels. Scaling of mesoscale simulations of polymer melts with the bare friction coefficient. *The Journal of Chemical Physics*, 123(22):224903, 2005.

[138] Flavien Lahmar and Bernard Rousseau. Influence of the adjustable parameters of the dpd on the global and local dynamics of a polymer melt. *Polymer*, 48(12):3584 – 3592, 2007.

[139] H. Sun. Compass: An ab initio force-field optimized for condensed-phase applications and overview with details on alkane and benzene compounds. *The Journal of Physical Chemistry B*, 102(38):7338–7364, 1998.

[140] Olagoke Olabisi and Robert Simha. Pressure-Volume-Temperature studies of amorphous and crystallizable polymers. i. experimental. *Macromolecules*, 8(2):206–210, 1975.

[141] E. von Meerwall, S. Beckman, J. Jang, and W. L. Mattice. Diffusion of liquid n-alkanes: Free-volume and density effects. *The Journal of Chemical Physics*, 108(10):4299–4304, 1998.

[142] Doros N. Theodorou and Ulrich W. Suter. Detailed molecular structure of a vinyl polymer glass. *Macromolecules*, 18(7):1467–1478, 1985.

[143] W. Paul, G. D. Smith, D. Y. Yoon, B. Farago, S. Rathgeber, A. Zirkel, L. Willner, and D. Richter. Chain Motion in an Unentangled Polyethylene Melt: A Critical Test of the Rouse Model by Molecular Dynamics Simulations and Neutron Spin Echo Spectroscopy. *Physical Review Letters*, 80(11):2346–2349, March 1998.

[144] P. Schleger, B. Farago, C. Lartigue, A. Kollmar, and D. Richter. Clear evidence of reptation in polyethylene from neutron spin-echo spectroscopy. *Phys. Rev. Lett.*, 81:124–127, Jul 1998.

[145] H. J. C. Berendsen, J. P. M. Postma, W. F. van Gunsteren, A. DiNola, and J. R. Haak. Molecular dynamics with coupling to an external bath. *The Journal of Chemical Physics*, 81(8):3684–3690, 1984.

[146] Tom Darden, Darrin York, and Lee Pedersen. Particle mesh Ewald: An N· log(N) method for Ewald sums in large systems. *The Journal of Chemical Physics*, 98(12):10089–10092, 1993.

[147] James Martens. Deep learning via Hessian-free optimization. In Johannes Fürnkranz and Thorsten Joachims, editors, *Proceedings of the 27th International Conference on Machine Learning (ICML-10)*, pages 735–742, Haifa, Israel, June 2010. Omnipress.

[148] V. A. Harmandaris, M. Doxastakis, V. G. Mavrantzas, and D. N. Theodorou. Detailed molecular dynamics simulation of the self-diffusion of n-alkane and cis-1,4 polyisoprene oligomer melts. *The Journal of Chemical Physics*, 116(1):436–446, 2002.

[149] Paul Zoller. The Pressure-Volume-Temperature properties of three well-characterized low-density polyethylenes. *Journal of Applied Polymer Science*, 23(4):1051–1056, 1979.

[150] Steve Plimpton. Fast parallel algorithms for short-range molecular dynamics. *Journal of Computational Physics*, 117(1):1 – 19, 1995.

[151] Robert D. Groot and Patrick B. Warren. Dissipative particle dynamics: Bridging the gap between atomistic and mesoscopic simulation. *The Journal of Chemical Physics*, 107(11):4423–4435, 1997.

[152] P. Espanol and P. Warren. Statistical mechanics of dissipative particle dynamics. *EPL (Europhysics Letters)*, 30(4):191, 1995.

[153] Anders Eriksson, Martin Nilsson Jacobi, Johan Nyström, and Kolbjørn Tunstrøm. Using force covariance to derive effective stochastic interactions in dissipative particle dynamics. *Phys. Rev. E*, 77:016707, Jan 2008.

[154] Anders Eriksson, Martin Nilsson Jacobi, Johan Nyström, and Kolbjørn Tunstrøm. A method for estimating the interactions in dissipative particle dynamics from particle trajectories. *Journal of Physics: Condensed Matter*, 21(9):095401, 2009.

[155] Anders Eriksson, Martin Nilsson Jacobi, Johan Nyström, and Kolbjørn Tunstrøm. Bottom-up derivation of an effective thermostat for united atoms simulations of water. *The Journal of Chemical Physics*, 130(16): 164509, 2009.

[156] Alexander P. Lyubartsev, Mikko Karttunen, Ilpo Vattulainen, and Aatto Laaksonen. On coarse-graining by the inverse monte carlo method: Dissipative particle dynamics simulations made to a precise tool in soft matter modeling. *Soft Materials*, 1(1):121–137, 2002.

[157] Huan Lei, Bruce Caswell, and George Em Karniadakis. Direct construction of mesoscopic models from microscopic simulations. *Phys. Rev. E*, 81:026704, Feb 2010.

[158] V. A. Harmandaris, N. P. Adhikari, N. F. A. van der Vegt, and K. Kremer. Hierarchical modeling of polystyrene: From atomistic to coarse-grained simulations. *Macromolecules*, 39(19):6708–6719, 2006.

[159] Joseph E. Mayer. Contribution to statistical mechanics. *The Journal of Chemical Physics*, 10(10):629–643, 1942.

[160] Jr. Prince E. Rouse. A theory of the linear viscoelastic properties of dilute solutions of coiling polymers. *The Journal of Chemical Physics*, 21(7):1272–1280, 1953.

[161] Bruno H. Zimm. Dynamics of polymer molecules in dilute solution: Viscoelasticity, flow birefringence and dielectric loss. *The Journal of Chemical Physics*, 24(2):269–278, 1956.

[162] J. Scott Shaffer. Effects of chain topology on polymer dynamics: Configurational relaxation in polymer melts. *The Journal of Chemical Physics*, 103(2):761–772, 1995.

[163] W. Paul, Grant D. Smith, and Do Y. Yoon. Static and dynamic properties of a n-C_{100} H_{202} melt from molecular dynamics simulations. *Macromolecules*, 30(25):7772–7780, 1997.

[164] M. Brodeck, F. Alvarez, A. Arbe, F. Juranyi, T. Unruh, O. Holderer, J. Colmenero, and D. Richter. Study of the dynamics of poly(ethylene oxide) by combining molecular dynamic simulations and neutron scattering experiments. *The Journal of Chemical Physics*, 130(9):094908, 2009.

[165] P.G. de Gennes. *Scaling Concepts in Polymer Physics*. Cornell University Press, 1979.

[166] M. Rubinstein and R.H. Colby. *Polymer Physics*. Oxford University Press, USA, 2003. ISBN 9780198520597.

[167] Ján Buša, Jozef DÅŸurina, Edik Hayryan, Shura Hayryan, Chin-Kun Hu, JÃ¡n Plavka, Imrich Pokorný, Jaroslav Skřivánek, and Ming-Chya Wu. ARVO: A fortran package for computing the solvent accessible surface area and the excluded volume of overlapping spheres via analytic equations. *Computer Physics Communications*, 165(1):59 – 96, 2005.

[168] JÃ¡n BuÅ¡a Jr., Shura Hayryan, Ming-Chya Wu, JÃ¡n BuÅ¡a, and Chin-Kun Hu. Arvo-cl: The OpenCL version of the arvo package - an efficient tool for computing the accessible surface area and the excluded volume of proteins via analytical equations. *Computer Physics Communications*, 183(11):2494 – 2497, 2012.

[169] Satish Kumar and Ronald G. Larson. Brownian dynamics simulations of flexible polymers with spring–spring repulsions. *The Journal of Chemical Physics*, 114(15):6937–6941, 2001.

[170] Florent Goujon, Patrice Malfreyt, and Dominic J. Tildesley. Mesoscopic simulation of entanglements using dissipative particle dynamics: Application to polymer brushes. *The Journal of Chemical Physics*, 129(3): 034902, 2008.

[171] Mikio Yamanoi, Oliver Pozo, and Joao M. Maia. Linear and non-linear dynamics of entangled linear polymer melts by modified tunable coarse-grained level dissipative particle dynamics. *The Journal of Chemical Physics*, 135(4):044904, 2011.

[172] Timothy W. Sirk, Yelena R. Slizoberg, John K. Brennan, Martin Lisal, and Jan W. Andzelm. An enhanced entangled polymer model for dissipative particle dynamics. *The Journal of Chemical Physics*, 136(13): 134903, 2012.

[173] F. Bueche. *Physical properties of polymers*. Interscience Publishers, 1962.

[174] G. Fleischer. The chain length dependence of self-diffusion in melts of polyethylene and polystyrene. *Colloid & Polymer Science*, 265:89–95, 1987.

[175] Timothy P. Lodge. Reconciliation of the molecular weight dependence of diffusion and viscosity in entangled polymers. *Phys. Rev. Lett.*, 83: 3218–3221, Oct 1999.

[176] D. S. Pearson, G. Ver Strate, E. Von Meerwall, and F. C. Schilling. Viscosity and self-diffusion coefficient of linear polyethylene. *Macromolecules*, 20(5):1133–1141, 1987.

[177] S. T. Cui, S. A. Gupta, P. T. Cummings, and H. D. Cochran. Molecular dynamics simulations of the rheology of normal decane, hexadecane, and tetracosane. *The Journal of Chemical Physics*, 105(3):1214–1220, 1996.

[178] Loukas I. Kioupis and Edward J. Maginn. Rheology, dynamics, and structure of hydrocarbon blends: a molecular dynamics study of n-hexane/n-hexadecane mixtures. *Chemical Engineering Journal*, 74(1-2): 129 – 146, 1999.

[179] Martin Kröger and Siegfried Hess. Rheological evidence for a dynamical crossover in polymer melts via nonequilibrium molecular dynamics. *Phys. Rev. Lett.*, 85:1128–1131, Jul 2000.

[180] T. Aoyagi and M. Doi. Molecular dynamics simulation of entangled polymers in shear flow. *Computational and Theoretical Polymer Science*, 10(3-4):317 – 321, 2000.

[181] J.D Moore, S.T Cui, H.D Cochran, and P.T Cummings. A molecular dynamics study of a short-chain polyethylene melt.: I. Steady-state shear. *Journal of Non-Newtonian Fluid Mechanics*, 93(1):83 – 99, 2000.

[182] J.D. Moore, S.T. Cui, H.D. Cochran, and P.T. Cummings. A molecular dynamics study of a short-chain polyethylene melt.: II. Transient response upon onset of shear. *Journal of Non-Newtonian Fluid Mechanics*, 93(1): 101 – 116, 2000.

[183] P.J. Daivis, M.L. Matin, and B.D. Todd. Nonlinear shear and elongational rheology of model polymer melts at low strain rates. *Journal of Non-Newtonian Fluid Mechanics*, 147(1-2):35 – 44, 2007.

[184] J.M. Kim, D.J. Keffer, M. Kröger, and B.J. Edwards. Rheological and entanglement characteristics of linear-chain polyethylene liquids in planar couette and planar elongational flows. *Journal of Non-Newtonian Fluid Mechanics*, 152(1-3):168 – 183, 2008.

[185] A. Jabbarzadeh, J. D. Atkinson, and R. I. Tanner. Effect of molecular shape on rheological properties in molecular dynamics simulation of star, h, comb, and linear polymer melts. *Macromolecules*, 36(13):5020–5031, 2003.

[186] N. A. Spenley. Scaling laws for polymers in dissipative particle dynamics. *EPL (Europhysics Letters)*, 49(4):534, 2000.

[187] C. M. Wijmans and B. Smit. Simulating tethered polymer layers in shear flow with the dissipative particle dynamics technique. *Macromolecules*, 35(18):7138–7148, 2002.

[188] Shuo Chen, Nhan Phan-Thien, Xi-Jun Fan, and Boo Cheong Khoo. Dissipative particle dynamics simulation of polymer drops in a periodic shear flow. *Journal of Non-Newtonian Fluid Mechanics*, 118(1):65 – 81, 2004.

[189] J. T. Padding and W. J. Briels. Coarse-grained molecular dynamics simulations of polymer melts in transient and steady shear flow. *The Journal of Chemical Physics*, 118(22):10276–10286, 2003.

[190] Maurizio Mondello, Gary S. Grest, Edmund B. Webb III, , , and P. Peczak. Dynamics of n-alkanes: Comparison to rouse model. *The Journal of Chemical Physics*, 109(2):798–805, 1998.

[191] Eric E. Keaveny, Igor V. Pivkin, Martin Maxey, and George Em Karniadakis. A comparative study between dissipative particle dynamics and molecular dynamics for simple- and complex-geometry flows. *The Journal of Chemical Physics*, 123(10):104107, 2005.

[192] JohnD. Ferry and RobertF. Landel. Molecular friction coefficients in polymers and their temperature dependence. *Kolloid-Zeitschrift*, 148 (1-2):1–6, 1956.

[193] J. H. Irving and John G. Kirkwood. The statistical mechanical theory of transport processes. IV. The equations of hydrodynamics. *The Journal of Chemical Physics*, 18(6):817–829, 1950.

[194] A W Lees and S F Edwards. The computer study of transport processes under extreme conditions. *Journal of Physics C: Solid State Physics*, 5 (15):1921, 1972.

[195] L. H. Tung. Melt viscosity of polyethylene at zero shear. *Journal of Polymer Science*, 46(148):409–422, 1960.

[196] Peter J. Daivis and Denis J. Evans. Comparison of constant pressure and constant volume nonequilibrium simulations of sheared model decane. *The Journal of Chemical Physics*, 100(1):541–547, 1994.

[197] Dilhan M. Kalyon, Dong-Woo Yu, and Francis H. Moy. Rheology and processing of linear low density polyethylene resins as affected by alpha-olefin comonomers. *Polymer Engineering & Science*, 28(23):1542–1550, 1988.

[198] Scott Bair, Clare McCabe, and Peter T. Cummings. Comparison of nonequilibrium molecular dynamics with experimental measurements in the nonlinear shear-thinning regime. *Phys. Rev. Lett.*, 88:058302, Jan 2002.

[199] H.A. Barnes, J.F. Hutton, and K. Walters. *An introduction to rheology*. Annals of Discrete Mathematics. Elsevier Science & Technology Books, 1989.

[200] P.J. Daivis, M.L. Matin, and B.D. Todd. Nonlinear shear and elongational rheology of model polymer melts by non-equilibrium molecular dynamics. *Journal of Non-Newtonian Fluid Mechanics*, 111(1):1 – 18, 2003.

[201] R.B. Bird and O. Hassager. *Dynamics of Polymeric Liquids: Fluid mechanics*. Dynamics of Polymeric Liquids. Wiley, 1987.

[202] M. Seriai, J. Guillet, and C. Carrot. A simple model to predict extrudate swell of polystyrene and linear polyethylenes. *Rheologica Acta*, 32(6): 532–538, 1993.

[203] P. G. Santangelo and C. M. Roland. Interrupted shear flow of unentangled polystyrene melts. *Journal of Rheology*, 45(2):583–594, 2001.

[204] E. V. Menezes and W. W. Graessley. Nonlinear rheological behavior of polymer systems for several shear-flow histories. *Journal of Polymer Science: Polymer Physics Edition*, 20(10):1817–1833, 1982.

[205] K. Osaki, T. Inoue, and T. Isomura. Stress overshoot of polymer solutions at high rates of shear. *Journal of Polymer Science Part B: Polymer Physics*, 38(14):1917–1925, 2000.

[206] Javier Sanchez-Reyes and Lynden A. Archer. Relaxation dynamics of entangled polymer liquids in steady shear flow. *Journal of Rheology*, 47 (2):469–482, 2003.

[207] Thomas Schweizer, Jan van Meerveld, and Hans Christian Öttinger. Nonlinear shear rheology of polystyrene melt with narrow molecular weight distribution—experiment and theory. *Journal of Rheology*, 48(6): 1345–1363, 2004.

[208] Dietmar Auhl, Jorge Ramirez, Alexei E. Likhtman, Pierre Chambon, and Christine Fernyhough. Linear and nonlinear shear flow behavior of monodisperse polyisoprene melts with a large range of molecular weights. *Journal of Rheology*, 52(3):801–835, 2008.

[209] Pouyan E. Boukany, Shi-Qing Wang, and Xiaorong Wang. Universal scaling behavior in startup shear of entangled linear polymer melts. *Journal of Rheology*, 53(3):617–629, 2009.

[210] D. W. Mead, R. G. Larson, and M. Doi. A molecular theory for fast flows of entangled polymers. *Macromolecules*, 31(22):7895–7914, 1998.

[211] G. Marrucci and G. Ianniruberto. Open problems in tube models for concentrated polymers. *Journal of Non-Newtonian Fluid Mechanics*, 82 (2-3):275 – 286, 1999.

[212] S. T. Milner, T. C. B. McLeish, and A. E. Likhtman. Microscopic theory of convective constraint release. *Journal of Rheology*, 45(2):539–563, 2001.

[213] Richard A. Vaia and Emmanuel P. Giannelis. Polymer melt intercalation in organically-modified layered silicates: Model predictions and experiment. *Macromolecules*, 30(25):8000–8009, 1997.

[214] Richard A. Vaia and Emmanuel P. Giannelis. Lattice model of polymer melt intercalation in organically-modified layered silicates. *Macromolecules*, 30(25):7990–7999, 1997.

[215] Anna C. Balazs, Chandralekha Singh, Ekaterina Zhulina, and Yulia Lyatskaya. Modeling the phase behavior of polymer/clay nanocomposites. *Accounts of Chemical Research*, 32(8):651–657, 1999.

[216] Jae Youn Lee, Arlette R. C. Baljon, Roger F. Loring, and Athanassios Z. Panagiotopoulos. Simulation of polymer melt intercalation in layered nanocomposites. *The Journal of Chemical Physics*, 109(23):10321–10330, 1998.

[217] Kelly L. Anderson, Anuchai Sinsawat, Richard A. Vaia, and B. L. Farmer. Control of silicate nanocomposite morphology in binary fluids: Coarse-grained molecular dynamics simulations. *Journal of Polymer Science Part B: Polymer Physics*, 43(8):1014–1024, 2005.

[218] E. Hackett, E. Manias, and E. P. Giannelis. Molecular dynamics simulations of organically modified layered silicates. *The Journal of Chemical Physics*, 108(17):7410–7415, 1998.

[219] Q. H. Zeng, A. B. Yu, G. Q. Lu, and R. K. Standish. Molecular dynamics simulation of organic-inorganic nanocomposites: Layering behavior and interlayer structure of organoclays. *Chemistry of Materials*, 15(25): 4732–4738, 2003.

[220] Q. H. Zeng, A. B. Yu, G. Q. Lu, and R. K. Standish. Molecular dynamics simulation of the structural and dynamic properties of dioctadecyldimethyl ammoniums in organoclays. *The Journal of Physical Chemistry B*, 108(28):10025–10033, 2004.

[221] D.R. Paul, Q.H. Zeng, A.B. Yu, and G.Q. Lu. The interlayer swelling and molecular packing in organoclays. *J Colloid Interface Sci*, 292(2):462–8, 2005.

[222] Hendrik Heinz, R. A. Vaia, and B. L. Farmer. Interaction energy and surface reconstruction between sheets of layered silicates. *The Journal of Chemical Physics*, 124(22):224713, 2006.

[223] Hendrik Heinz, R. A. Vaia, R. Krishnamoorti, and B. L. Farmer. Self-assembly of alkylammonium chains on montmorillonite: Effect of chain length, head group structure, and cation exchange capacity. *Chemistry of Materials*, 19(1):59–68, 2007.

[224] Yao-Tsung Fu and Hendrik Heinz. Cleavage energy of alkylammonium-modified montmorillonite and relation to exfoliation in nanocomposites: Influence of cation density, head group structure, and chain length. *Chemistry of Materials*, 22(4):1595–1605, 2010.

[225] E. Hackett, E. Manias, and E. P. Giannelis. Computer simulation studies of peo/layer silicate nanocomposites. *Chemistry of Materials*, 12(8): 2161–2167, 2000.

[226] E. Manias, V. Kuppa, D.-K. Yang, and D.B. Zax. Relaxation of polymers in 2 nm slit-pores: confinement induced segmental dynamics and suppression of the glass transition. *Colloids and Surfaces A: Physicochemical and Engineering Aspects*, 187-188(0):509 – 521, 2001.

[227] V. Kuppa, S. Menakanit, R. Krishnamoorti, and E. Manias. Simulation insights on the structure of nanoscopically confined poly(ethylene oxide). *Journal of Polymer Science Part B: Polymer Physics*, 41(24):3285–3298, 2003.

[228] Maurizio Fermeglia, Marco Ferrone, and Sabrina Pricl. Computer simulation of nylon-6/organoclay nanocomposites: prediction of the binding energy. *Fluid Phase Equilibria*, 212(1-2):315 – 329, 2003.

[229] Fabrice Gardebien, Anouk Gaudel-Siri, Jean-Luc Brédas, and Roberto Lazzaroni. Molecular dynamics simulations of intercalated poly(ϵ-caprolactone)-montmorillonite clay nanocomposites. *The Journal of Physical Chemistry B*, 108(30):10678–10686, 2004.

[230] Maurizio Fermeglia, Marco Ferrone, and Sabrina Pricl. Estimation of the binding energy in random poly(butylene terephtalate-co-thiodiethylene terephtalate) copolyesters/clay nanocomposites via molecular simulation. *Molecular Simulation*, 30(5):289–300, 2004.

[231] Paolo Cosoli, Giulio Scocchi, Sabrina Pricl, and Maurizio Fermeglia. Many-scale molecular simulation for ABS-MMT nanocomposites: Upgrading of industrial scraps. *Microporous and Mesoporous Materials*, 107(1-2):169 – 179, 2008.

[232] Q.H. Zeng, A.B. Yu, and G.Q. Lu. Multiscale modeling and simulation of polymer nanocomposites. *Progress in Polymer Science*, 33(2):191 – 269, 2008.

[233] Azadeh Ghanbari, Tinashe V. M. Ndoro, Frédéric Leroy, Mohammad Rahimi, Michael C. Böhm, and Florian Müller-Plathe. Interphase structure in silica-polystyrene nanocomposites: A coarse-grained molecular dynamics study. *Macromolecules*, 45(1):572–584, 2012.

[234] Giulio Scocchi, Paola Posocco, Maurizio Fermeglia, and Sabrina Pricl. Polymer-clay nanocomposites: A multiscale molecular modeling approach. *The Journal of Physical Chemistry B*, 111(9):2143–2151, 2007.

[235] Marek Maly, Paola Posocco, Sabrina Pricl, and Maurizio Fermeglia. Self-assembly of nanoparticle mixtures in diblock copolymers: Multiscale molecular modeling. *Industrial & Engineering Chemistry Research*, 47 (15):5023–5038, 2008.

[236] Giulio Scocchi, Paola Posocco, Andrea Danani, Sabrina Pricl, and Maurizio Fermeglia. To the nanoscale, and beyond!: Multiscale molecular modeling of polymer-clay nanocomposites. *Fluid Phase Equilibria*, 261 (1-2):366 – 374, 2007.

[237] Radovan Toth, Dirk-Jan Voorn, Jan-Willem Handgraaf, Johannes G. E. M. Fraaije, Maurizio Fermeglia, Sabrina Pricl, and Paola Posocco. Multiscale computer simulation studies of water-based montmorillonite/poly(ethylene oxide) nanocomposites. *Macromolecules*, 42(21): 8260–8270, 2009.

[238] Dirk Reith, Mathias Pütz, and Florian Müller-Plathe. Deriving effective mesoscale potentials from atomistic simulations. *Journal of Computational Chemistry*, 24(13):1624–1636, 2003.

[239] Roland Faller. Automatic coarse graining of polymers. *Polymer*, 45(11): 3869 – 3876, 2004.

[240] Xuejin Li, Xiaojing Ma, Lei Huang, and Haojun Liang. Developing coarse-grained force fields for cis-poly(1,4-butadiene) from the atomistic simulation. *Polymer*, 46(17):6507 – 6512, 2005.

[241] Hossein Eslami, Hossein Ali Karimi-Varzaneh, and Florian Müller-Plathe. Coarse-grained computer simulation of nanoconfined polyamide-6,6. *Macromolecules*, 44(8):3117–3128, 2011.

[242] Beste Bayramoglu and Roland Faller. Coarse-grained modeling of polystyrene in various environments by iterative boltzmann inversion. *Macromolecules*, 45(22):9205–9219, 2012.

[243] Hendrik Heinz, Hilmar Koerner, Kelly L. Anderson, Richard A. Vaia, and B. L. Farmer. Force field for mica-type silicates and dynamics of octadecylammonium chains grafted to montmorillonite. *Chemistry of Materials*, 17(23):5658–5669, 2005.

[244] Hendrik Heinz and Ulrich W. Suter. Atomic charges for classical simulations of polar systems. *The Journal of Physical Chemistry B*, 108(47): 18341–18352, 2004.

[245] Masaya Kawasumi, Naoki Hasegawa, Makoto Kato, Arimitsu Usuki, and Akane Okada. Preparation and mechanical properties of polypropylene-clay hybrids. *Macromolecules*, 30(20):6333–6338, 1997.

[246] Pham Hoai Nam, Pralay Maiti, Masami Okamoto, Tadao Kotaka, Naoki Hasegawa, and Arimitsu Usuki. A hierarchical structure and properties of intercalated polypropylene/clay nanocomposites. *Polymer*, 42 (23):9633 – 9640, 2001.

[247] S. Hotta and D.R. Paul. Nanocomposites formed from linear low density polyethylene and organoclays. *Polymer*, 45(22):7639 – 7654, 2004.

[248] Tanaka G. and Goettler L.A. Predicting the binding energy for nylon 6,6/clay nanocomposites by molecular modeling. *Polymer*, 43(2):541–553, 2002.

[249] Victor Rühle, Christoph Junghans, Alexander Lukyanov, Kurt Kremer, and Denis Andrienko. Versatile object-oriented toolkit for coarse-graining applications. *Journal of Chemical Theory and Computation*, 5(12):3211–3223, 2009.

[250] Berk Hess, Carsten Kutzner, David van der Spoel, and Erik Lindahl. GROMACS 4: Algorithms for highly efficient, load-balanced, and scalable molecular simulation. *Journal of Chemical Theory and Computation*, 4(3):435–447, 2008.

[251] L. Martínez, R. Andrade, E. G. Birgin, and J. M. Martínez. PACKMOL: A package for building initial configurations for molecular dynamics simulations. *Journal of Computational Chemistry*, 30(13):2157–2164, 2009.

[252] Li-Qiong Wang, Jun Liu, Gregory J. Exarhos, Kyle Y. Flanigan, and R. Bordia. Conformation heterogeneity and mobility of surfactant molecules in intercalated clay minerals studied by solid-state NMR. *The Journal of Physical Chemistry B*, 104(13):2810–2816, 2000.

[253] Maged A. Osman, Michael Ploetze, and Peter Skrabal. Structure and properties of alkylammonium monolayers self-assembled on montmorillonite platelets. *The Journal of Physical Chemistry B*, 108(8):2580–2588, 2004.

[254] Girish Galgali, C. Ramesh, and Ashish Lele. A rheological study on the kinetics of hybrid formation in polypropylene nanocomposites. *Macromolecules*, 34(4):852–858, 2001.

COLOPHON

This document was typeset with LaTeX and BibTeXusing the typographical look-and-feel `classicthesis` developed by André Miede, available via:

`http://code.google.com/p/classicthesis/`

The style was inspired by Robert Bringhurst's seminal book on typography "*The Elements of Typographic Style*".